1992

Contrasting styles of alteration and metamorphism in shear zones at Wawa, Ontario.

Deborah Lynn. MacDonald
University of Windsor

NOTICE

The quality of this microform is heavily dependent upon the quality of the original thesis submitted for microfilming. Every effort has been made to ensure the highest quality of reproduction possible.

If pages are missing, contact the university which granted the degree.

Some pages may have indistinct print especially if the original pages were typed with a poor typewriter ribbon or if the university sent us an inferior photocopy.

Reproduction in full or in part of this microform is governed by the Canadian Copyright Act, R.S.C. 1970, c. C-30, and subsequent amendments.

AVIS

La qualité de cette microforme dépend grandement de la qualité de la thèse soumise au microfilmage. Nous avons tout fait pour assurer une qualité supérieure de reproduction.

S'il manque des pages, veuillez communiquer avec l'université qui a conféré le grade.

La qualité d'impression de certaines pages peut laisser à désirer, surtout si les pages originales ont été dactylographiées à l'aide d'un ruban usé ou si l'université nous a fait parvenir une photocopie de qualité inférieure.

La reproduction, même partielle, de cette microforme est soumise à la Loi canadienne sur le droit d'auteur, SRC 1970, c. C-30, et ses amendements subséquents.

CONTRASTING STYLES OF ALTERATION AND METAMORPHISM IN SHEAR ZONES AT WAWA, ONTARIO

BY

DEBORAH LYNN MACDONALD

A Thesis
Submitted to the Faculty of Graduate Studies and Research
through the Department of Geology
in partial fulfilment
of the requirements for the degree of
Master of Science
at the University of Windsor

Windsor, Ontario, Canada
1992

ISBN 0-315-72781-0

ABSTRACT

Petrographic and chemical analysis of sheared rocks from seven narrow deformation zones in Archean-age rocks near Wawa, Ontario reveal different styles of alteration and deformation. Deformation of felsic intrusive, volcanic and volcaniclastic protoliths can be monitored by median grain-sizes of feldspars. The strained rocks are classified into protomylonite, mylonite and ultramylonite using feldspar grain-size measurements and clast/matrix ratios. The reduction of grain size and modal abundance of feldspar is accompanied by formation of hydrous phases such as muscovite and epidote. Typically, the loss of feldspar is accompanied by losses in SiO_2 and the alkali and alkali-earth elements, presumably to the hydrous fluids associated with the mylonitization. Relative increases in less mobile components, particularly the high field strength elements, result from a net loss of soluble components from the sheared rocks. The chemical patterns show evidence of significant volume loss in many of the shear zones.

Hydrothermal alteration and gold mineralization result in complex chemical patterns in some of the shear zones. Typically mineralizing fluids add SiO_2, alkalis, copper, gold and arsenic. Early alterations are overprinted by the chemical changes accompanying formation of mylonites and post-deformation alterations are generally constrained to the most deformed rocks. Evidence of multiple deformation and alteration events in the study area leads to a proposed model of the temporal relationship among the deformation and mineralization events. The northeast-striking shear zones show evidence of an early mineralization that is disturbed and altered during mylonitization. In some cases the shear zones act as conduits for a later mineralizing event. A set of northwest-striking shear zones offset the northeast-striking set. The northwest set show a less complex history with a single mineralizing event following deformation.

ACKNOWLEDGEMENTS

I wish to take this opportunity to thank the people who most contributed to the completion of this thesis. First and foremost, I would like to thank Dr. William Blackburn, my thesis advisor, who contributed many, many hours of his time. Dr. Blackburn guided me carefully through each stage of this study, and I am very fortunate to have had such a patient, supportive and understanding advisor. I would also like to thank Dr. Iain Samson for his insight and help with the initial field work, software assistance, and for always finding the time to answer a question or two.

To the staff at the Geology Department, I extend thanks for all the help they have provided over the course of the past two years. Special thanks to Anton Knitl for assistance in thin section preparation.

I am grateful to Mr. Roy Rupert of Citadel Gold Mines for providing maps for field work, and other information.

Finally, I would like to acknowledge the support of my family. They have been a constant source of encouragement and love, for which I will be forever grateful.

TABLE OF CONTENTS

LIST OF FIGURES

PAGE

LIST OF TABLES

CHAPTER 1

INTRODUCTION

Geology of the Wawa Area

Location

The study area is located to the southeast of Wawa, Ontario within the National Topographic System sheet number 41 N/15. Geologically, the region is within the southwestern portion of the Michipicoten greenstone belt of Ontario, part of the Wawa Subprovince of the Superior Province of the Canadian Shield (Figure 1). The supracrustal rocks of the Michipicoten greenstone belt extend east from the northeast corner of Lake Superior for 141 km and have a maximum width of 38 km (Sage, 1991). The study area is situated almost entirely within McMurray Township, with the exception of the southernmost sections which lie within Razabo and Naveau Townships.

Geology of the Superior Province

The Canadian Shield comprises seven structural provinces: the Southern, Slave, Nain, Churchill, Bear, Grenville and the Superior Provinces. The Superior Province lies in the southeastern part of the Shield and is bounded on all sides by younger supracrustal and crystalline rocks (Goodwin, 1972). A remnant of an early Precambrian craton, the Superior Province includes units of Mid-Archean (2900-3400 Ma) to Late-Archean (2500-2900 Ma) age. It is subdivided into a number of fault-bounded subprovinces, which are classified as either volcano-plutonic, plutonic, metasedimentary, or high-grade gneiss types (Card and Ciesielski, 1986), based on structural, lithologic, metamorphic, age, and geophysical characteristics. Volcano-plutonic subprovinces include the Wabigoon, Sachigo, La Grande River, Uchi, Abitibi and the Wawa. These greenstone belts form elongate regions, separated by younger granitic complexes of metavolcanic and minor metasedimentary rocks. They are

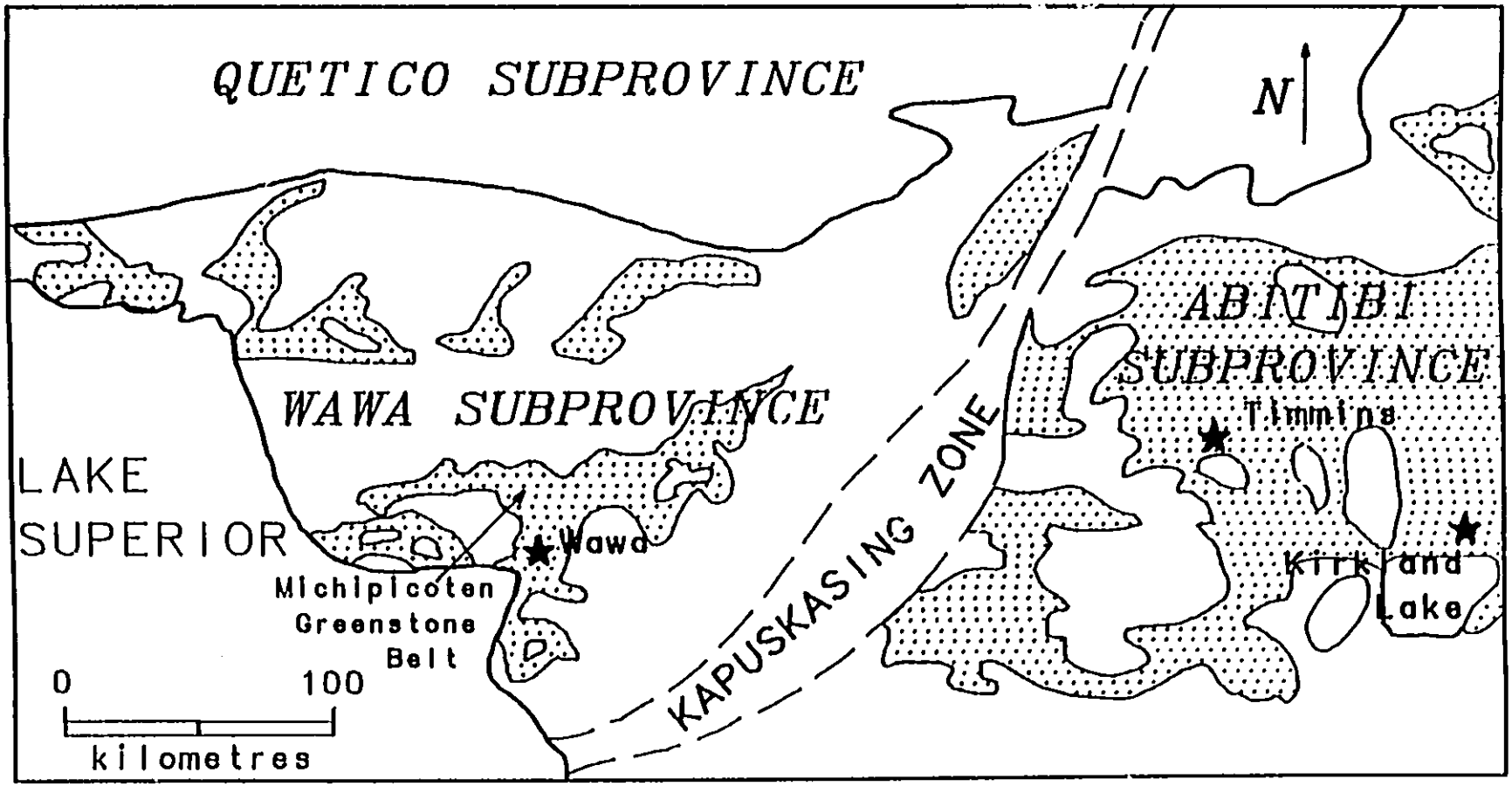

Fig.1. Regional map showing location of the Wawa Subprovince. Greenstone belts are dotted. The study area is within the Michipicoten greenstone belt, to the south and east of the town of Wawa. Modified after Heather, 1991.

characterized by shear-zone bounded homoclinal and complexly folded segments of supracrustal rocks (Colvine, 1989).

The Archean metavolcanics, metasediments, and early mafic intrusions of the greenstone belts underwent Early Precambrian, greenschist facies regional metamorphism. Locally, the rocks have undergone contact metamorphism in the vicinity of felsic intrusions. Feldspars and mafic minerals in the intrusive rocks are extensively altered by a thermal event related to late faulting and accompanying mafic intrusive activity prior to deposition of Middle Precambrian supracrustal rocks of the Southern Province (Lumbers, 1978).

Geology of the Michipicoten Greenstone Belt

The geology of the Michipicoten greenstone belt includes at least three sequences of volcanic rocks, which in some localities are separated by Algoma-type banded iron formation. The physical characteristics of the volcanic, volcaniclastic, and sedimentary rock units reflect subaerial, shallow subaqueous, and locally deeper water depositional environments (Sylvester et al., 1989). The Michipicoten supracrustal sequences generally form cycles ranging in composition from tholeiitic basalt to calc-alkalic felsic volcanics (Thurston, 1986). The 2900 Ma cycle is the oldest in the study area and represents basaltic to perid-otitic komatiite volcanism followed by calc-alkalic felsic volcanism (Sage, 1991). Meta-sedimentary rocks in the Michipicoten greenstone belt include conglomerate, siltstone, wacke, and argillite derived from the penecontemporaneous volcanics (Ojakangas, 1983).

Intermediate to mafic intrusions, ranging in composition from peridotite to quartz diorite intrude the supracrustal sequences. Granitoid stocks ranging from tonalite and trondhjemite to granite also intrude the volcanic and sedimentary sequences (Sage, 1991).

The supracrustal rocks and most of the intrusive rocks within the greenstone belt have been interpreted to represent an originally monoclinal stratigraphic sequence (Sage, 1991). Structural deformation involved early thrusting, followed by folding and the develop-

ment of strike-slip faults. A later deformation event resulted in the establishment of a prominent set of northwest, left-lateral transverse faults, which are commonly occupied by diabase dikes. Local reactivation of the strike-slip faults has resulted in minor offsets of some of the diabase dikes (Sage, 1991).

The core of the Michipicoten greenstone belt consists of greenschist facies rocks. The metamorphic grade increases to amphibolite facies toward the margins because of the effects of contact metamorphism by younger external granitic rocks (Turek et al., 1990).

Geology of the Study Area

The geology and gold mineralization of McMurray Township has been studied in detail by Rupert (1975, 1979) and Sage (1979, 1981). The Wawa supracrustal sequence consists of at least three cycles of volcanism. The region to the east and southeast of the town of Wawa contains the youngest igneous rocks of the Archean Michipicoten greenstone belt (Figure 2). Here felsic to intermediate tuffs, feldspar crystal tuffs, lapilli tuffs and subordinate felsic flows are intruded by dioritic to granodioritic rocks of the Jubilee stock (Sage, 1979). The Jubilee stock is an epizonal intrusion that contains abundant xenoliths and blocks of the supracrustal host rocks (Sage, 1979). Diabase dikes, generally trending NW, are common throughout the area. Biotite-rich and olivine-rich lamprophyre dikes of generally less than one-meter width are common and generally strike NE (Sage, 1979). All of these rocks were subject to regional metamorphism at conditions of the greenschist facies. No regional penetrative fabric exists, but highly localized shear zones occur.

The shear zones are often characterized by muscovite-, chlorite-, biotite-, and carbonate-rich schists (I.M. Samson, pers. comm., 1991). In the field it is difficult to determine whether mafic schists represent hydrothermal alteration zones or if they represent original lithologic variations along which the strain was concentrated. Both relationships appear to exist in different localities, whereas other areas are more ambiguous.

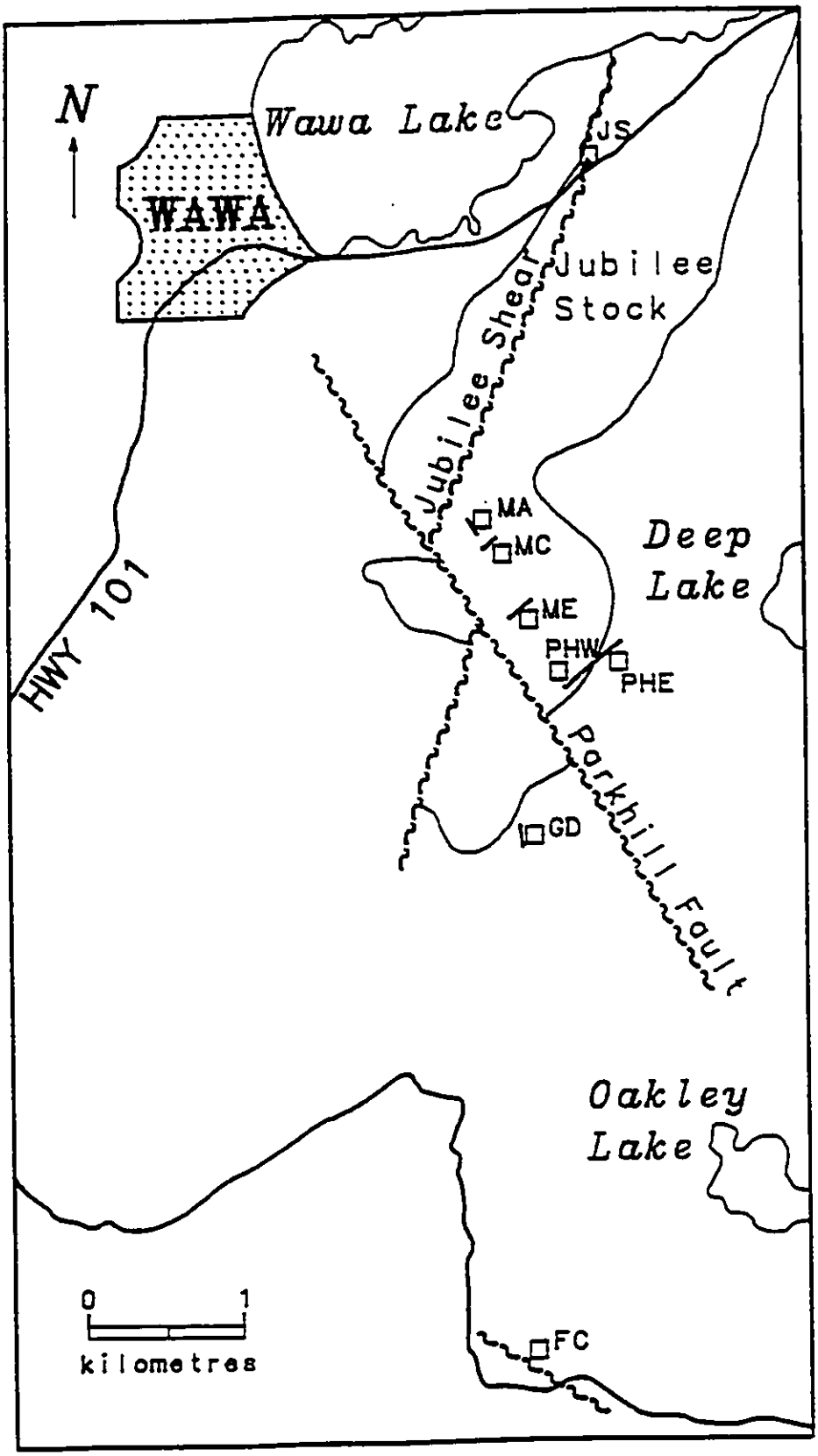

Fig.2. Map of the study area showing the location of major faults (sheared pattern), minor shear zones, and sampling locations (open squares).

History of Gold Mining in the Wawa Area

The Wawa area has a long history of minor gold production from shear-zone hosted auriferous quartz veins. Significant mineralization occurs in other parts of the Michipicoten and Mishibishu greenstone belts, in similar geological settings and in rocks of similar characteristics. For these reasons, the area is considered to have good potential for gold exploration.

Gold was first discovered in 1896 on the south shore of Wawa Lake (Rupert, 1979). Over the next ten years, prospectors located most of the presently known gold deposits. Several producing mines were in operation during the 1920's and 1930's, including the Grace, Darwin, Minto, Jubilee, Parkhill, Deep Lake, VanSickle, Stanley, and Cooper Mines. A brief resurgence of gold exploration and mining activities in the late 1960's lead to the opening of the Surluga Mine in 1967. Operations at the Surluga mine continued periodically in the years 1968-1969, and in 1989 (Rupert, 1979).

Gold exploration activity in the study area in the 1980's included overburden stripping, trenching, diamond drilling and geological mapping by Citadel Gold Mines Limited. Dewatering and underground re-evaluation of the Surluga and the Jubilee Mines was initiated in 1987. Surface drilling resulted in the discovery of a new ore zone in the Surluga mine. Geophysical surveys were also conducted by Citadel Gold Mines.

In 1989 and 1990 Van Ollie Explorations Limited conducted mapping, sampling and surface drilling of gold prospects and past-producing mines in McMurray Township. Exploration activities were conducted primarily in veins near the Minto and Parkhill Mine sites (Tortosa et al., 1990).

General Geology of the Gold Deposits

Gold occurs in classic Archean quartz vein-shear zone deposits (Sage, 1991). The gold mineralization is mainly associated with early east-west shears and faults and splays

from these major shear zones (Rupert, 1979). Gold mineralization occurs in quartz veins that are localized in numerous shear zones (Figure 2) that cut both the Jubilee stock and the volcanic sequence (Rupert, 1975). The Surluga and Jubilee mines exploit quartz veins and silicified zones within the Jubilee Shear, a complex reverse fault zone that strikes NNE, dips 40-50°E and parallels the western margin of the Jubilee Stock. Numerous other shear zones and quartz-filled fissure vein systems are located in the hanging wall of the Jubilee shear, many of which are mineralized and have been mined for gold at some time in the past. Ore shoots occur as elongated quartz veins or zones of siliceous laminated stringers of quartz in the schist. Ore zones in these shears are restricted to areas where the shear zone walls are predominantly intermediate to felsic intrusive rocks. Where the shear zones intersect volcanic pyroclastic rocks with a higher phyllosilicate content, the ore zones are not present (Rupert, 1979).

Objectives

The gold-producing district near Wawa, Ontario is characterized by multiple shear zones, some of which are altered by late mineralizing fluids. The purpose of this project is to characterize the nature of the protolith, the mylonites and mylonite zones at Wawa, in terms of their chemistry and mineralogy, and the chemical changes that have occurred within the shear zones. An attempt is made to distinguish hydrothermal alteration that accompanied and/or followed deformation. The primary goal is to interpret the relationship of gold mineralization to formation of the shear zones and the hydrothermal alteration.

The main question to be answered is: Can the geochemical effects accompanying mylonitization be distinguished from those of secondary hydrothermal alteration? If so, what are the chemical changes that are the result of mylonitization and what are the chemical effects of the hydrothermal alteration events? How is gold mineralization related to shearing and hydrothermal alteration? The approach taken in this study is to characterize

the chemical effects of mylonitization and thereby isolate the effects of alteration.

Methods

The methods used to achieve the objectives outlined included detailed petrological studies of the protoliths, the mylonitic rocks, and interpretation of the petrographic and mineralogical changes that occur across the shear zones. Alteration assemblages were determined and used to characterize the types of alteration. Microstructural observations assisted in the characterization of the stages of mylonite development and hydrothermal alteration. Chemical studies were used to identify elemental gains and losses in the deformed rocks, which were in turn used to assess chemical fluxes, fluid compositions, volume losses, and the operative fluid/rock ratios.

Petrographic and geochemical analyses have been performed on eight suites of mylonites from the Wawa area. Only those shear zones that have continuous outcrop across the shear zone boundary from protolith to mylonitic rock, with no apparent original heterogeneities in rock type were sampled. This was necessary so that the alteration within each shear zone could be characterized in terms of its chemical, petrographical and mineralogical effects on a single protolith rock unit. Each individual suite includes at least one example of undeformed protolith and a series of deformed rocks taken at intervals across the shear zone. Changes in chemical, mineralogical and structural characteristics are interpreted using the protoliths as a basis of comparison since they are assumed to represent the undeformed and unaltered equivalents of the shear zone rocks.

CHAPTER 2

STRAIN IN SHEAR ZONES

Mechanisms and Kinematics

Since their first recognition and description from the Moine Thrust zone in the Scottish Highlands (Lapworth, 1885), geologists have recognized that mylonites indicate zones of concentrated deformation. Originally thought to be products of clastic milling and brittle fracturing, mylonites are now recognized as products of dominantly ductile flow and intracrystalline deformation, resulting in grain size reduction by recrystallization.

Griggs and Blacic (1965) first demonstrated that the presence of fluids, even in small amounts, can promote grain-size reduction and recrystallization. More recent investigations have shown that complex interactions between cataclasis, crystal-plastic mechanisms, fluids and metamorphic reactions take place in shear zones (eg., Dixon and Williams, 1983; White and White, 1983). Kerrich et al. (1977) stated that at low grade (greenschist facies), deformation may be dominated by mass transfer and volume changes, and therefore crystal-plastic processes may be of less importance. Chemical studies by O'Hara and Blackburn (1987, 1989) and O'Hara (1988, 1990) have demonstrated the importance of mass transfer and volume changes in mylonitic gneisses.

Shear zones exhibit non-coaxial strain (Berthé et al., 1979), which has suggested to some authors (e.g.; Simpson, 1986) that they may be modelled as products of heterogenrous simple shear. Strain analyses of mylonites exhibit finite strain in the field of apparent flattening (Coward, 1976; Choukroune and Gapais, 1983) on a Flinn diagram (Flinn, 1962). Cobbold (1977) modelled these strains on the basis of shear bands with a component of shortening normal to the shear zone boundaries. Bulk heterogeneous shortening has been proposed as a model for deformation in rocks which deformed along conjugate shear zones (Bell, 1981). In this model, space problems associated with bulk strain are accommodated

by the addition of a component of dilation.

Ramsay and Wood (1973) illustrated the geometric effect of dilation during deformation; rocks which have volume loss plot in the field of apparent flattening, an effect which is produced by shortening along the Z-direction of the strain ellipsoid without concomitant elongation in the X-direction. Volume loss, therefore can be incorrectly attributed to true flattening. Ramsay and Huber (1987) show that volume loss and variable shear strains are compatible, and these components can be identified if suitable strain markers are present. The amount of volume change, and the amount of shear strain across a shear zone can be calculated using the displacement of initially planar markers (Ramsay, 1980).

Indicators such as asymmetric folds (Bell and Hammond, 1984), *S*- and *C*-planes (Lister and Snoke, 1984), foliation fish (Hanmer, 1986), asymmetric augen (Simpson and Schmid, 1983; Passchier and Simpson, 1983), or displaced marker horizons may be used to determine sense-of-shear locally within the shear zone. If the orientations, both inside and outside the shear zone, of two differently oriented lines (traces of bedding planes, dikes, etc.) are known, it is possible to compute the values of shear strain and volumetric dilation at different points at specific directions from the shear zone walls (Ramsay and Huber, 1987). If the shear direction cannot be determined from the sense-of-shear criteria, three differently oriented planar structures are required to determine the shear direction, amount of shear, and the dilation across the zone. A further method of separating volumetric and shear components arises when the elipticity and orientation of the strain ellipse outside the shear zone, the elipticity of the strain ellipse at a point inside the shear zone, and the deflections of a single marker horizon are all known (Ramsay, 1980).

Petrographic and Mineralogic Effects

Crystal-plasticity of matrix minerals in mylonites accommodate large strains and result in extensive dynamic recrystallization, grain-size reduction and preferred crystallo-

graphic orientation (Lister and Snoke, 1984; Ralser et al., 1991). A wide variety of microstructures are common, ranging from undulose extinction, kinking and polygonization of quartz in the early stages, to subgrain formation, twinning, dynamic recrystallization and mortar textures in the more advanced stages (Bell and Etheridge, 1973).

O'Hara (1988) observed that muscovite content increased with deformation in the shear zones with an accompanying feldspar grain size reduction. These observations, together with petrographic evidence for a reaction relationship between alkali feldspar and muscovite lead to the conclusion that the following reaction played an important role in the development of the mylonites:

$$\underset{\text{alkali feldspar}}{1.5\ NaAlSi_3O_8} + H^+ = \underset{\text{muscovite}}{0.5\ KAl_3Si_3O_{10}(OH)_2} + K^+ + 3SiO_2. \quad (1)$$

In addition, a more complex reaction postulated by Bryant (1966) and reiterated by O'Hara (1988) may explain the breakdown of plagioclase feldspars, as well as the increase of zoisite toward the shear zones:

$$\underset{\text{oligoclase}}{Na_4CaAl_6Si_{14}O_{40}} + \underset{\text{alkali feldspar}}{1.5KAlSi_3O_8} + 0.5K^+ + 0.5H_2O + 3.5H^+$$

$$= \underset{\text{zoisite}}{0.5Ca_2Al_3Si_3O_{12}(OH)} + \underset{\text{muscovite}}{2KAl_3Si_3O_{10}(OH)_2} + 11SiO_2 + 4Na^+ \quad (2)$$

O'Hara and Blackburn (1989) found that mylonites derived from gneisses of granodioritic composition contain high proportions of epidote and chlorite, and that mylonites derived from gneisses of granitic composition contain more muscovite. Petrographic observations correlate closely with those of O'Hara (1988) concerning the increase in phyllosilicate content, and corresponding decrease on feldspar content with decreasing grain size. O'Hara and Blackburn (1989) propose that these observations may be accounted for by one or both the above reactions (1) and (2). They added a third possible reaction that may occur by itself, or in conjunction with reaction (1) and/or reaction (2):

$$2NaAlSi_3O_8 + KAlSi_3O_8 + 2H^+ = KAl_3Si_3O_{10}(OH)_2 + 6SiO_2 + 2Na^+ \quad (3)$$

albite alkali feldspar muscovite

All of the proposed reactions are hydrolysis reactions that involve a release of alkalis and silica to an aqueous fluid phase. The inferred loss of alkalis is further supported by the depletion of Rb and Sr in the mylonites (O'Hara and Blackburn, 1989). The reactions would also have a strain-softening effect on the rocks as the mechanical breakdown of feldspar and the formation of muscovite occurs.

Classification of Mylonitic Rocks

Hanmer (1987) developed a field classification scheme for quartzo-feldspathic mylonitic rocks that avoids the complex nomenclature for fault-related rocks suggested by other authors (Zeck, 1974; Tullis et al., 1982; Wise et al., 1984). Using the textural classification defined by Sibson (1977), Hanmer defined three rock types associated with ductile fault zones; protomylonite, mylonite, and ultramylonite. By Hanmer's (1987) definition, protomylonite transforms to mylonite when the volumetric matrix/porphyroclast ratio exceeds 50%, and mylonite transforms to ultramylonite when this ratio exceeds 90%. O'Hara (1988) extended this classification scheme to the thin section scale using feldspar grain size in phi (ϕ) units (where $\phi = -\log_2$diameter) as an indicator of intensity of mylonitization. On the basis of the median feldspar grain-size, deformed protoliths are classified as either protomylonites, mylonites or ultramylonites. The range of grain size for each of these rock types will, of course, differ for each shear zone, depending on the original grain sizes in the protolith. A continuous reduction in grain sizes from protolith-protomylonite-mylonite-ultramylonite could, however, be documented for any given shear zone if the protolithology is the same across that zone.

Chemical Effects

Mylonites and cataclasites show both petrographic and chemical evidence of distinct mineralogical changes. The changes that occur during the formation of shear zones depend on a number of variables; including original lithology, metamorphic grade, degree of brittle versus ductile behaviour, the relative solubilities of constituent species, and the amount and nature of fluids within the zone. Nonetheless, petrographic and chemical data in quartzo-feldspathic mylonites have revealed important changes that may be expected to take place.

Generally, chemical changes accompanying mylonitization indicate decreases of SiO_2, K_2O, Na_2O, CaO, Rb and Sr, and increases of TiO_2, P_2O_5, Nb, V, Zr, Y, MnO, $Fe_2O_3^*$ (Fe_2O_3 as total iron), and MgO (O'Hara, 1988, 1990; O'Hara and Blackburn, 1989; Glazner and Bartley, 1991). Sinha, et al. (1986) document losses of silica and alkalies, accompanied by gains in CaO, FeO and H_2O.

O'Hara and Blackburn (1989) found that the concentration of minor and trace elements varies with median feldspar grain size in the deformed rocks. Large Ion Lithophile (LIL) elements such as Rb and Sr are progressively depleted with decreasing grain size. In contrast, high field strength elements (HFSE) such as Ti, Zr, P, V and Y are progressively enriched. O'Hara (1988) determined that the elemental enrichments can be attributed to refractory phases such as zircon, apatite, ilmenite and epidote found in the protoliths but considerably enriched in the mylonites. The HFSE generally have very low solubilitites and can be assumed to be immobile, even in the presence of large volumes of fluid. The relative enrichments, therefore, must be attributed to volume losses rather than addition of these elements by mineralizing fluids (O'Hara and Blackburn, 1989).

Volume-loss Models

The presence of styolites and solution cleavages in sedimentary rocks and low-

grade metamorphic rocks indicate substantial volume losses. Estimates range from a few percent up to as high as 30% (Hortenbach, 1977). Such estimates are based on the accumulation of inert phases such as zircon, apatite, epidote and ilmenite along styolites or cleavage surfaces. Similar enrichments of inert phases have been reported in mylonites (Winchester and Max, 1984; Vocke et al., 1987; Wayne and Sinha, 1988), but have generally been interpreted to be the result of increased mobility of these chemical species as a result of the presence of large volumes of fluids. Vocke et al. (1987) proposed increased mobility of rare earth elements (REE) in the Roffna Gneiss, Switzerland but Dicken (1988) reinterpreted the data and concluded that a volume loss of approximately 50% would account for the observed REE enrichments.

Experimental and natural studies suggest that the HFSE remain immobile up to very high fluid/rock ratios (e.g.; Cann, 1970; Correns, 1978; Herrmann, 1978; Landergren, 1978). Sinha et al. (1986) document the development of an ultramylonite domain by focused fluid flow, resulting in leaching of selected solutes, and residual enrichment of other phases within the shear zone. O'Hara (1988) attributes enrichments of immobile elements in mylonites from the Hot Springs Window, North Carolina, to large (up to 60%) volume loss. O'Hara and Blackburn (1989) reported the presence of an insoluble residue of zircon, ilmenite, apatite, and epidote along foliation planes in some mylonites and ultramylonites. O'Hara and Blackburn (1989) expanded their volume loss model based on data from the Fries fault, Virginia to include the selective partitioning of some elements. Results indicate that a pure volume-loss or a combined volume-loss plus partitioning model can successfully explain the observed trace element enrichments.

Glazner and Bartley (1991) determined that variable enrichments of low-mobility elements in mylonitic rocks from the Mojave metamorphic core complex reflect differential mobility, but inferred that true mobility was achieved by some elements, including Ti, Zr and Co.

CHAPTER 3

GOLD MINERALIZATION

Alteration Effects

Alteration assemblages in the Superior Province vary according to the metamorphic grade of host rocks and reflect alteration mineral stabilities under elevated ambient pressure and temperature of regional metamorphism (Colvine, 1989). Gold deposits exhibit a high variability in form and distribution of mineralization. Mineralization is most commonly associated with quartz veins, but in some deposits gold is hosted in sulphide-rich rocks adjacent to veins (Colvine, 1989).

Archean gold deposits are accompanied by intense and extensive wall-rock alteration (Colvine, 1989). The particular type of alteration related to gold mineralization is controlled by the nature of the altering fluids and is identified by observing which elements have been added to or subtracted from the system.

One of the most common types of alteration, *phyllic* or *sericitic* alteration involves the leaching of sodium, calcium, and magnesium from aluminosilicate-bearing rocks, accompanied by the introduction of potassium and silicon. Sericitic alteration generally results in the replacement of rock-forming silicates by sericitic muscovite and quartz. Potassium-rich mica is present in virtually all Archean gold deposits (Colvine et al., 1988). and is prevalent in deformed rocks in this study.

Propyllitic alteration is common in originally mafic rocks and involves the formation of new calcium and magnesium minerals such as chlorite, epidote, and calcite by alteration of mafic minerals, calcium-rich plagioclase, and introduction of H^+ and CO_2. Many of the rocks of intermediate composition in the study area exhibit an increase in epidote, chlorite and/or calcite with increasing strain.

Silicic alteration is characterized by the presence of quartz veins and the replace-

ment of both silicate and carbonate minerals by quartz, often accompanied by the removal of alkalies and aluminum.

Secondary alteration involving emplacement of quartz and quartz-calcite veins occurs throughout the study area. Some quartz veins and silicification zones are pre- or syn-deformation. Some large quartz veins cross-cut the shear zone and were avoided by this study. Carbonate alteration is also common throughout the greenstone belt. Locally, tourmaline alteration and sodium-calcium metasomatism have been identified (Sage, 1991).

Chemical Effects

Bulk chemical changes that result from metasomatic reactions vary according to the mineral phases present in the wall rocks, the reactive ions in the metasomatic fluids, and the physical and chemical conditions. Factors such as oxygen fugacity, pH, Eh and the chemical activities of the species available for reaction all determine to some degree the net changes that will occur in the chemistry of the host rocks. These factors are related to the temperature and pressure associated with regional metamorphism, and local factors in the depositional environment. In addition, evolution of fluid composition occurs as wall-rock alteration proceeds, potentially changing the operative reactions and net chemical changes.

The introduction of CO_2, K_2O, S, and H_2O are common in shear-zone hosted gold deposits. Elements such as As, Sb, W, Mo, B, Ag, Li, Ba, Rb, and Cr are sometimes found in association with gold (Colvine et al, 1988). Enrichments of these elements in the host rocks may indicate potential for the presence of gold.

Structural Controls

Gold deposits are found exclusively within deformation zones (Colvine, 1989). Although fluid migration is ubiquitous in shear zone formation, focused fluid migration may be required for significant concentrations of gold. Strain analyses demonstrate that many

sites of gold concentration correspond to local zones of dilation within the shear zone (Robert and Brown, 1986), a likely site for fluid focusing.

Gold precipitation within the shear zones may be promoted by hydrostatic pressure changes caused by seismogenic fault failure (Sibson, et al., 1988), or loss of volatile phases during hydraulic fracturing (Spooner, et al., 1987). Gold precipitation may be caused by other local factors, such as oversaturation, oxidation of the transporting complex, reduction of the fluid, changes in pH and fO_2, and plating onto sulphides even when the fluid is undersaturated with respect to gold (Bancroft and Jean, 1982).

Timing

Many studies of Archean gold deposits propose an epigenetic model of gold deposition (e.g., Perring et al., 1987; Colvine et al, 1988). In many deposits, the major episode of hydrothermal fluid passage related to gold concentration was synchronous with both shearing and regional metamorphism (Colvine, 1989). Alteration studies indicate that the hydrothermal activity in many Archean shear zone-hosted gold deposits took place during or somewhat after the peak of metamorphism, which was related to the emplacement of batholiths surrounding the greenstone belts (Colvine et al, 1988). Geochronological studies have demonstrated a temporal link between gold mineralization and pluton emplacement in the lower crust (Colvine, 1989).

Documented structural observations in the study area have failed to show definitively whether the mineralization has been controlled by the shearing or if early mineralization and hydrothermal alteration has promoted localization of shear strain. Rupert (1975) observed that shearing apparently post-dates vein formation. Helmstaedt (1988) observed on the basis of subsurface structural relationships that there was a structural control on mineralization by an early fault system. He concluded that the penetrative deformation then sheared the mineralized zones, and had no control on their location or orientation.

CHAPTER 4

PETROGRAPHIC STUDIES

Methods

Samples were collected from eight different shear zones; some mineralized and some with no evidence of mineralization. Care was taken to avoid samples in the vicinity of late quartz veins and/or mafic units. The original nature of some mafic schists within the shear zones is suspect. If they represent original mafic units within the predominantly felsic shear zones, their chemical, petrographical, and mineralogical evolution during deformation was unrelated to that of the felsic protoliths.

Samples were selected from a cross-sectional traverse normal to the walls of the shear zone. Deviations from this were necessary where outcrops were not continuous or where cross-cutting units such as quartz veins and lamprophyre dikes were present. Each sampling traverse includes at least one sample of the protolith, taken at a location well-removed from the shear zone, but where continuity in rock type is assured. Where outcrop continuity existed, protolith samples from both sides of the shear zone were taken. Hand samples were characterized in terms of their modal mineralogy and degree of deformation, using the field classification of Hanmer (1987).

Slabs for thin sections were cut from each sample at a moderate to high angle to the foliation. Because of the well-developed schistosity of some of the deformed rocks, and their tendency to break along foliation planes, it was necessary to cut many of the slabs at right angles to the foliation in order to obtain a slab large enough for a thin section. Thin sections were examined using a Leitz Laborlux 12 polarizing microscope. Modal mineralogy was determined by point-counting techniques using a Swift automatic point counter Model F on thin sections stained with a sodium cobaltinitrite solution (see Appendix A for staining techniques). The number of points counted per thin section varied from 600-1000, depending on the overall grain size of the rock. Between 800 and 1000 points were

counted for the finer-grained samples, and between 600-800 for the coarser-grained samples. Step size was chosen according to the number of points desired, and the area of the thin section. Step size ranged from 1 (0.16mm) to 4 (0.64mm) for different samples, but never varied on a single thin section. Modal analyses are provided in Appendix B.

Feldspar grain-sizes were measured using a Lasico digital filar eyepiece, and converted to phi (ϕ) units for presentation. Feldspar grain-sizes are plotted versus frequency distribution. For large populations of grain-size measurements, these distributions are plotted as cumulative percent. The use of cumulative frequency for small populations (less than 50) is precarious because small changes in class populations result in large changes in the frequency distributions. The standard statistical procedure for graphic analysis of small populations is to use ranked normal deviates, or rankits (Sokal and Rohlf, 1969). These values are obtained by repeated sampling of n items from a standard normal population, and ranking the items in each sample by order of magnitude. The first rankit value is the mean of the first item from every sample, the second rankit value is the mean of the second item from every sample, and so on. Tables of rankit values are provided by Rohlf and Sokal (1969).

Distinctions between protoliths, protomylonites, mylonites, and ultramylonites are based on feldspar grain-size distributions (Table 17, Appendix C). These divisions are arbitrary and are used only as indicators of intensity of deformation in order to permit generalization of the chemical changes that have occurred at various stages of mylonitization within each shear zone.

Statistical data on filar grain-size measurements are provided in Appendix C. For each population of grains (either alkali feldspar or plagioclase feldspar), the number of grains measured (n), the mean size (ϕ) of those grains ($\bar{x}$), the median grain-size (M), the standard deviation (σ) of that population, the mode, skewness, kurtosis, and Kolmogorov-Smirnov (K-S) statistic are given. Skewness is a measure of the degree of asymmetry of a

distribution curve. If the curve is skewed to the left, the sign of skewness is negative. For positive skewness values, the curve is skewed to the right. Kurtosis is a measure of the peakedness of a distribution curve. If the distribution has more items near the mean and at the tails than a normal curve with the same mean and variance, it is leptokurtic and has a negative sign. A platykurtic curve has fewer items at the mean and at the tails than the normal curve, and has a positive sign; bimodal distributions are extremely platykurtic. The Kolmogorov-Smirnov test is a nonparametric test based on the absolute differences between observed and expected frequency distributions. Tabled critical values (Rohlf and Sokal, 1969) are used to decide if the maximum difference in observed and expected frequency distributions is significant for a given confidence level.

Petrography of the Shear Zones

Fred C

The Fred C mylonite zone is the widest and most intensely deformed zone in the study. Located in the southernmost portion of the study area approximately 7 km S-SE of the town of Wawa (Figure 2), it strikes 120°-126°N, dips 60°-69°SW and its northern margin is exposed. Ten samples were taken across the exposed zone over a cross-sectional distance of 220 meters (Figure 3).

Modal compositions of the samples collected are presented in Table 1 (Appendix B). The protolith is a coarse-grained leucocratic granodiorite, consisting of quartz, plagioclase feldspar (oligioclase), orthoclase, muscovite, biotite, opaques and accessory zircon. Larger grains of quartz show undulose extinction. Euhedral plagioclase and orthoclase grains have minor sericitic alteration. Trace amounts of biotite, zircon and opaque minerals, and some hematite staining are visible in thin section.

Within the shear zone, the rocks contain abundant muscovite grains which are aligned and define a foliation. The sheared rocks exhibit varying degrees of deformation

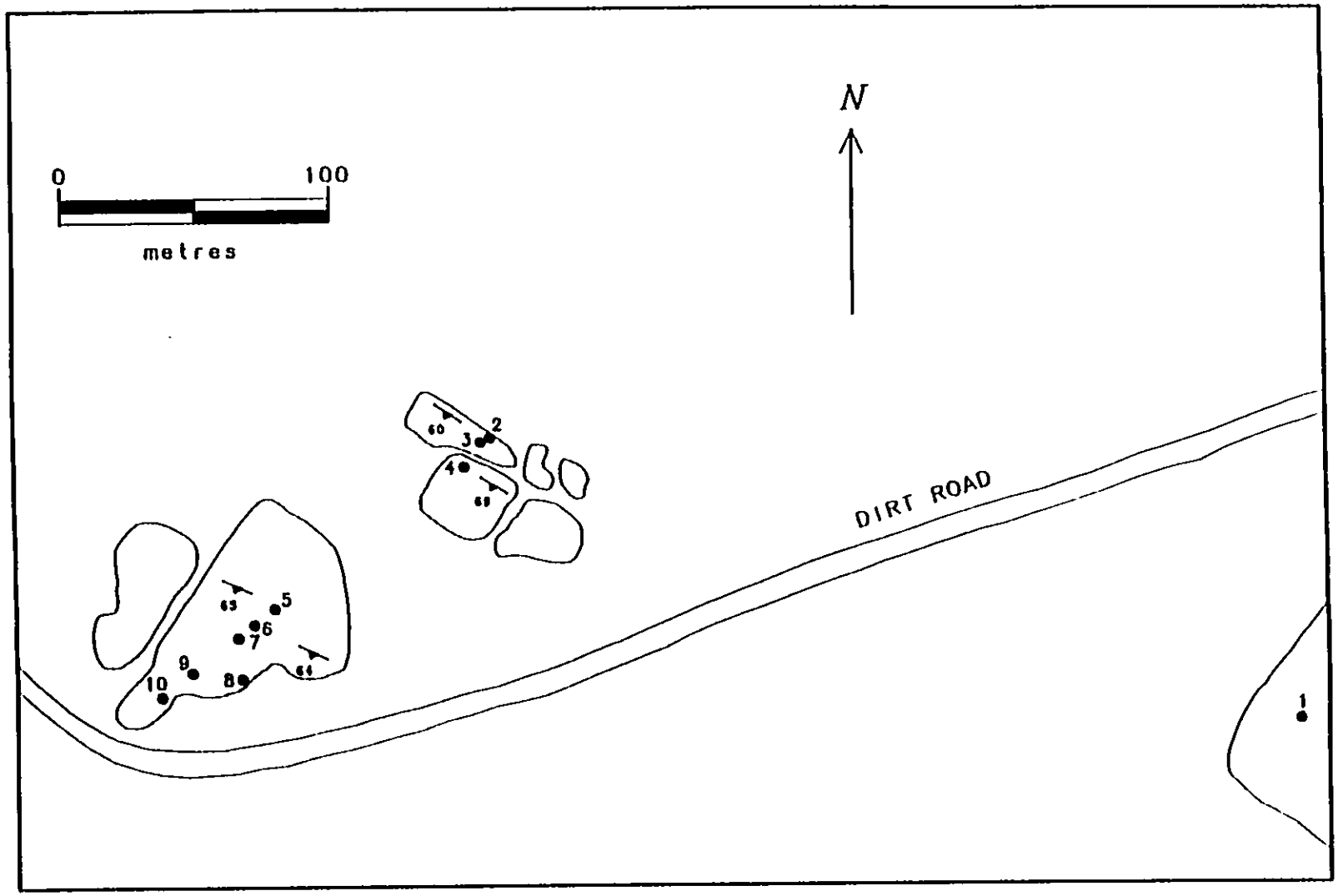

Fig.3. Map showing individual sample locations of the Fred C shear zone. The protolithology is granodiorite.

with the most intensely deformed rocks containing ribbons and augen of quartz, and small feldspar augen. Evidence of feldspar breakdown is observed petrographically with grains appearing increasingly anhedral and progressively altered by fine-grained muscovite and quartz. In some deformed rocks, both muscovite and chlorite occurs as alteration products of feldspar. Some carbonate alteration is observed, and is likely related to the breakdown of plagioclase. The proportions of opaques in the Fred C samples varies from 0.5% in the protolith to 10.9% in FC-90-4.

Filar grain-size measurements of the Fred C shear zone feldspars are shown in Figure 4. Statistical analysis of grain size data are presented in Table 2 (Appendix B). Plagioclase and alkali feldspar display an overall similar grain-size distribution, and a progressive decrease in grain-size. Generally well-sorted, unimodal distributions characterize plagioclase feldspar. Alkali feldspar displays a very pronounced decrease in grain-size, and is absent from some sheared rocks. Some samples (FC-90-4, FC-90-6), appear to have bimodal size distributions which represent the transition from larger to smaller grain sizes. The progressive decrease in the number of alkali feldspar grains in the sheared rocks reflects the breakdown and disappearance of this phase with progressive deformation.

Grace Darwin

The Grace Darwin shear zone is located near the former Grace and Darwin mines, approximately 4 kms S-SE of the town of Wawa (Figure 2). The zone trends 135°N and dips 75° NE. Quartz stockwork pervades the country rock and late hematite staining is prevalent. Eleven samples were taken in a cross-sectional traverse across the zone over a distance of 14 meters (Figure 5).

The modal analysis of samples from this shear zone are presented in Table 3 (Appendix B). The protolith is a porphyritic volcanic of intermediate (andesite) composition. Relict feldspar phenocrysts are extensively altered to epidote. Euhedral biotite and retro-

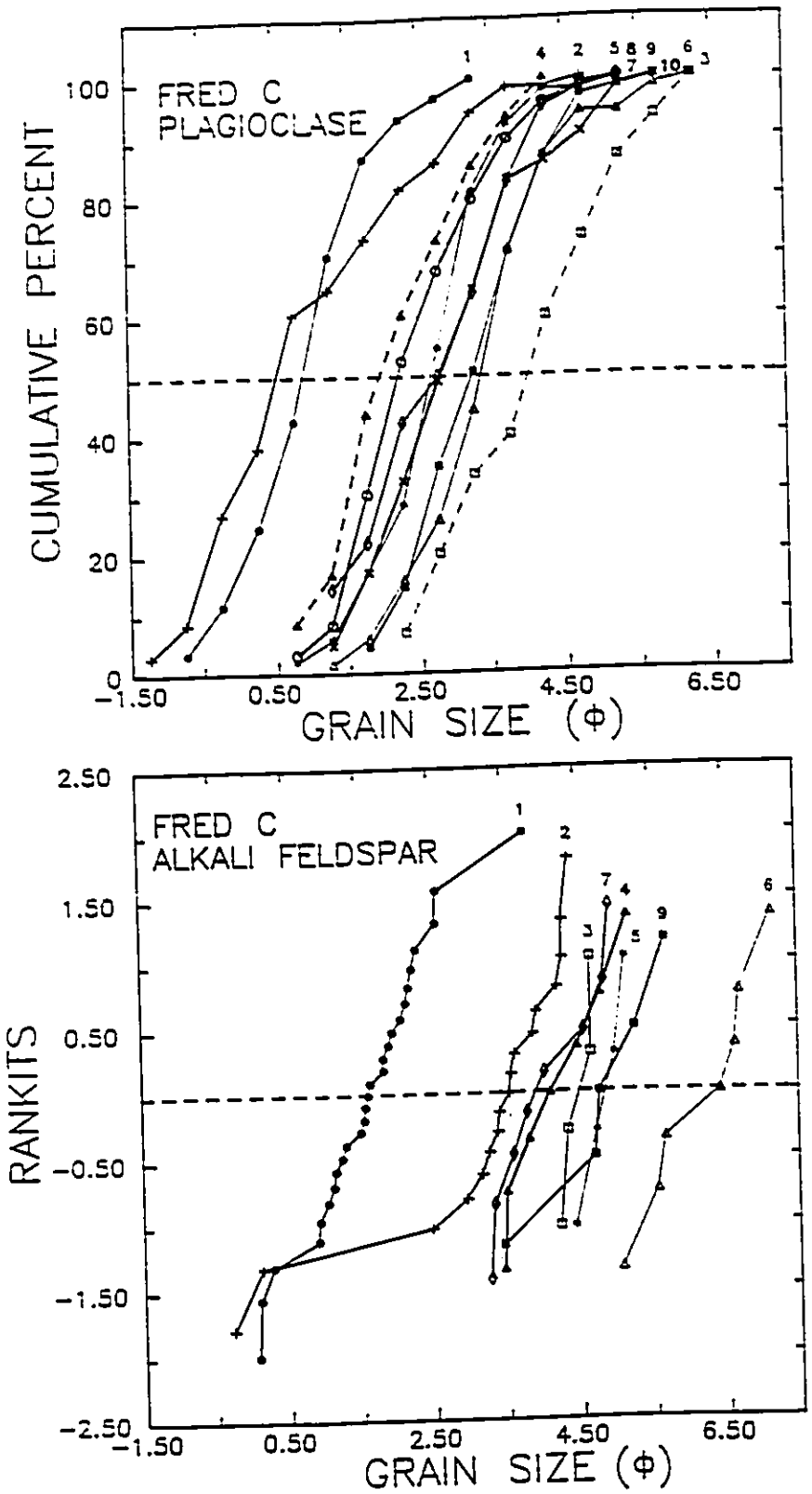

Fig.4. Cumulative frequency grain-size distribution of plagioclase and alkali feldspar in rocks associated with the Fred C shear zone.

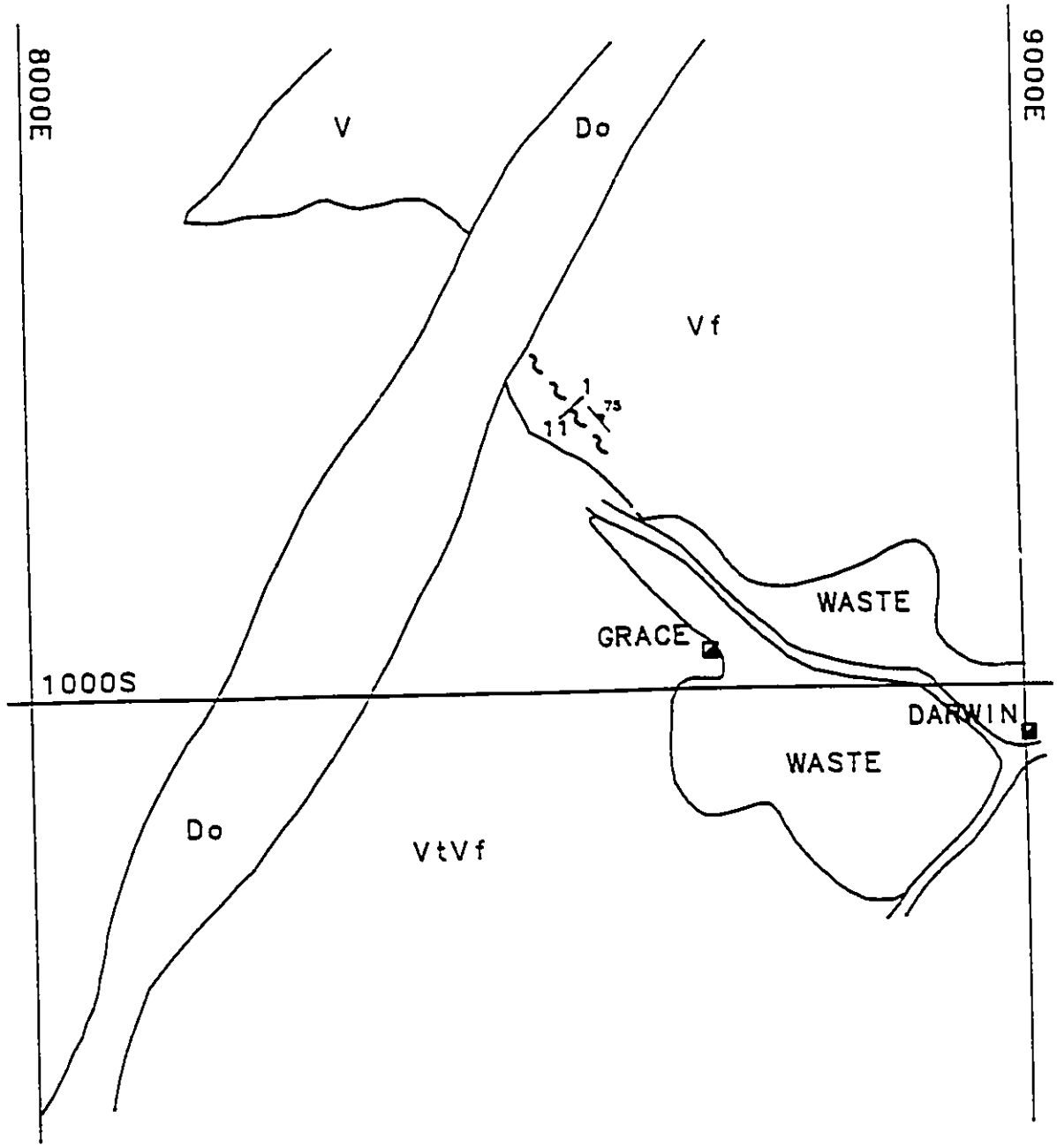

Fig.5. Map showing geology and sample locations of the Grace Darwin shear zone. Do = dolerite; Vf = feldspathic volcanics; V = volcanics; VtVf = volcanic tuffs and subordinate flows. Shear zone indicated by shear pattern. Samples GD-90-1 through GD-90-11 taken across shear zone where indicated.

grade chlorite crystals comprise 49.3% of the rock. Biotite crystals are usually incompletely replaced by chlorite. Plagioclase grains are extensively replaced by epidote, making compositional determinations difficult.

With increasing degree of deformation, the effects of alteration are more pronounced as the foliation, defined by parallel muscovite-rich bands, becomes more developed. Relict feldspar phenocrysts appear increasingly anhedral and show evidence of brittle fracturing and mechanical breakdown in the deformed rocks. Grain-size reduction of biotite grains is also evident in thin section.

GD-90-6 exhibits a parallel alignment of elongate grains and shows no relict feldspar grains. Large post-tectonic poikiolitic biotite crystals with radioactive halos are abundant. The proportion of opaques in this sample is significantly higher than in other, less deformed samples.

Muscovite is a significant phase in samples GD-90-7 through GD-90-9, comprising from 33.3% to 51.0% of the rocks. Small relict feldspar grains show extensive sericitic alteration. Pressure shadows around relict feldspar grains contain fine-grained recrystallized quartz. Pods or augen of quartz and feldspar clasts are wrapped by the foliation. Opaque grains occur along foliation planes and within quartz augen, indicating that the ore minerals may be pre-tectonic. Other opaque grains in the matrix are euhedral, and commonly tabular in form. Biotite ± chlorite generally occurs sub-parallel to the foliation.

GD-90-10 and GD-90-11 contain abundant laths and acicular grains of chlorite. In both samples, muscovite is rare or absent. Small, anhedral plagioclase feldspar grains are present in both samples. Pods and augen of quartz are found in sample GD-90-10, but are absent GD-90-11. GD-90-11 contains rounded and irregular feldspar grains. Small veinlets of calcite + epidote cut the sample.

Plagioclase grain-size analyses are presented graphically in Figure 6. Statistics of the grain-size data are provided in Table 4 (Appendix B). Progressive plagioclase grain-size

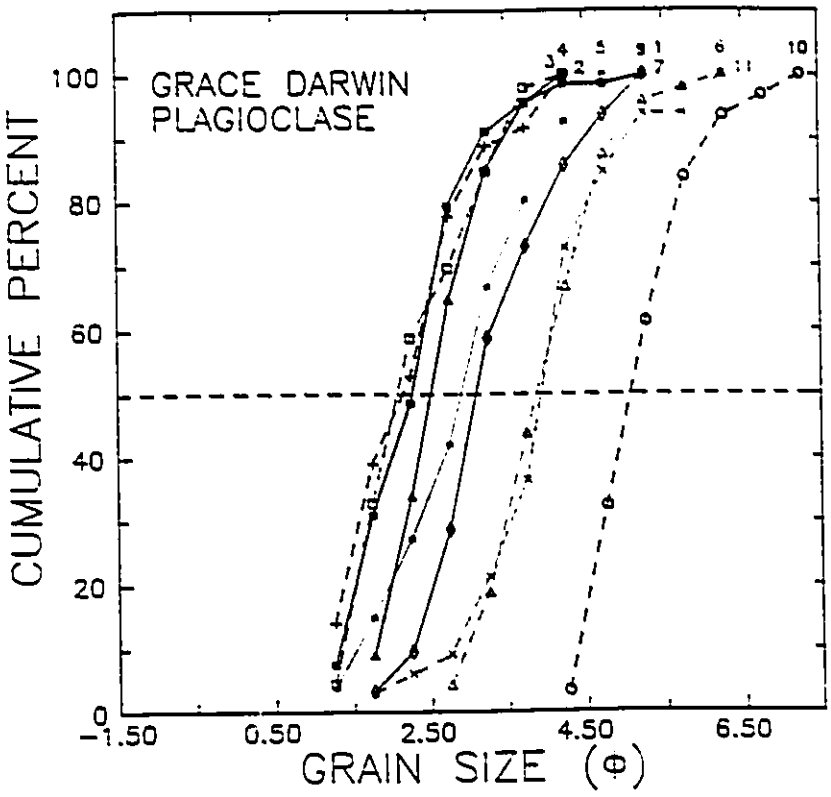

Fig.6. Cumulative frequency grain-size distribution of plagioclase feldspar in rocks associated with the Grace Darwin shear zone.

reduction occurs with increasing mylonitization. Individual curves indicate well-sorted, unimodal distributions of grain sizes in samples 3, 4, 5, 6, 7, 8, 10 and 11. Samples 1, 2, and 9 have bimodal distributions of feldspar grain-sizes.

Jubilee

The Jubilee shear is located approximately 2 km east of the town of Wawa (Figure 2). Cutting both the Jubilee Stock and the country rocks, it is a major regional structure in the Wawa area. Many of the former gold-producing mines are located in the hanging wall of the Jubilee shear. The shear zone trends 010°-028°N and dips 31°-44°E. It is a dextral reverse oblique shear zone indicated by *S/C* fabrics in the mylonites (Samson and Holm, 1991). Eight samples were taken across the shear zone over a distance of approximately 16m (Figure 7).

Modal analyses for samples from the Jubilee shear zone are presented in Table 5 (Appendix B). The protolith samples (JS-90-1 and JS-90-2) are tonalitic crystal tuffs and consist of quartz, plagioclase, orthoclase, minor pyrite, biotite, epidote, chlorite, and calcite. A few secondary veins are observed which contain quartz, epidote and muscovite. Plagioclase composition is not readily determined because of the extensive alteration of the grains.

Sample JS-90-3 has no obvious foliation, but large quartz crystals have undulose extinction and small dynamically recrystallized grains occur. Feldspar grains have significant alteration to fine-grained muscovite and chlorite. Calcite occurs interstitially.

Mylonites have elongated augen of quartz and quartz + calcite which are wrapped by the matrix of fine-grained muscovite and quartz. Biotite and retrograde chlorite grains generally subparallel the foliation. JS-90-6 contains 1.3% tourmaline which subparallels the foliation.

JS-90-7 is the most intensely deformed rock in the zone. It exhibits a well-devel-

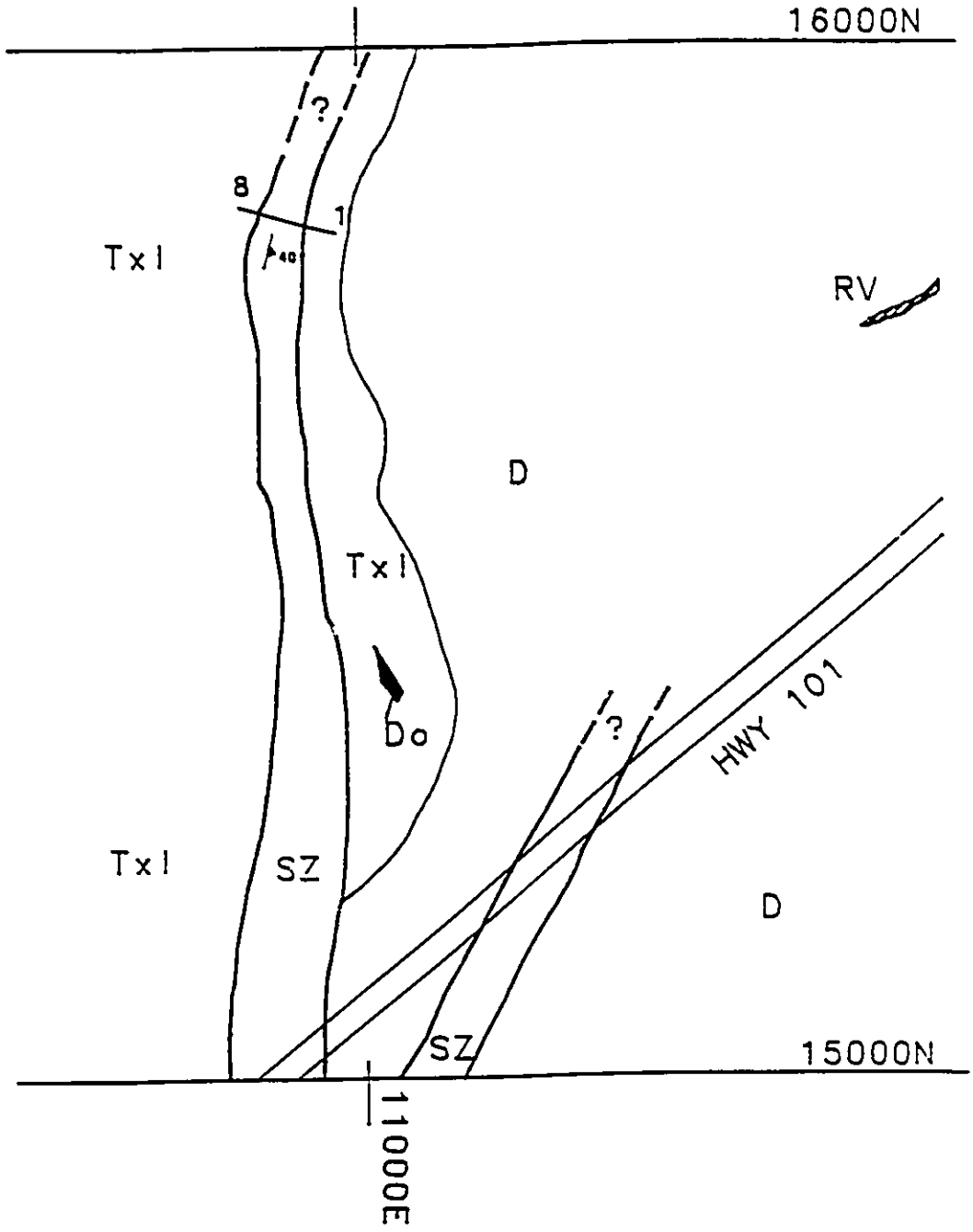

Fig.7. Map showing geology and sample locations of the Jubilee shear zone. Txl = crystal tuff; Do = dolerite; D = diorite; SZ = shear zone; RV = root vein. Samples JS-90-1 through JS-90-8 taken across shear zone where indicated.

oped foliation defined by muscovite, which displays a preferred crystallographic orientation. Large euhedral biotite grains subparallel the foliation. Quartz occurs as fine-grained crystals in the matrix and as large porphyroblasts in pods and ribbons. Anastomosing fabric development is observed.

Plagioclase and alkali feldspar grain-size changes across the shear zone are illustrated in Figure 8. Statistical analysis of grain-size data is given in Table 6 (Appendix B). Alkali feldspar occurs only in samples JS-90-1 and JS-90-3, and only a few grains were found in each. Plagioclase is the dominant feldspar and its distribution shows the progressive decrease in feldspar grain-sizes. Overall, the size distributions appear unimodal.

Minto A

The Minto A shear zone is located approximately 2 kms southeast of the town of Wawa (Figure 2). The overall foliation in the Minto A shear zone is 128°/55°NE. *C/S* fabric relationships and asymmetric boudins of quartz-carbonate vein indicate normal displacement (Samson and Holm, 1990). Within the deformation zone, foliation orientation is variable and anastomosing on the outcrop scale. Four samples were taken over a distance of 12 meters from the unsheared wall rocks to the highly foliated rocks in the center of the shear zone (Figure 9). The presence of a lamprophyre dike on the western side of the shear zone inhibited a full cross-sectional traverse across the zone.

Modal analyses of samples from the Minto A shear zone are presented in Table 7 (Appendix B). The protolith rocks are quartz diorites to granodiorites and consist of quartz, chlorite, plagioclase feldspar (oligioclase), alkali feldspar, muscovite, biotite, minor calcite, opaques, epidote, and accessory zircon. The feldspar grains exhibit minor sericitization and epidotization.

With increasing degree of deformation, the foliated rocks display a lower biotite/ chlorite ratio as biotite appears progressively replaced by retrograde chlorite. Large quartz

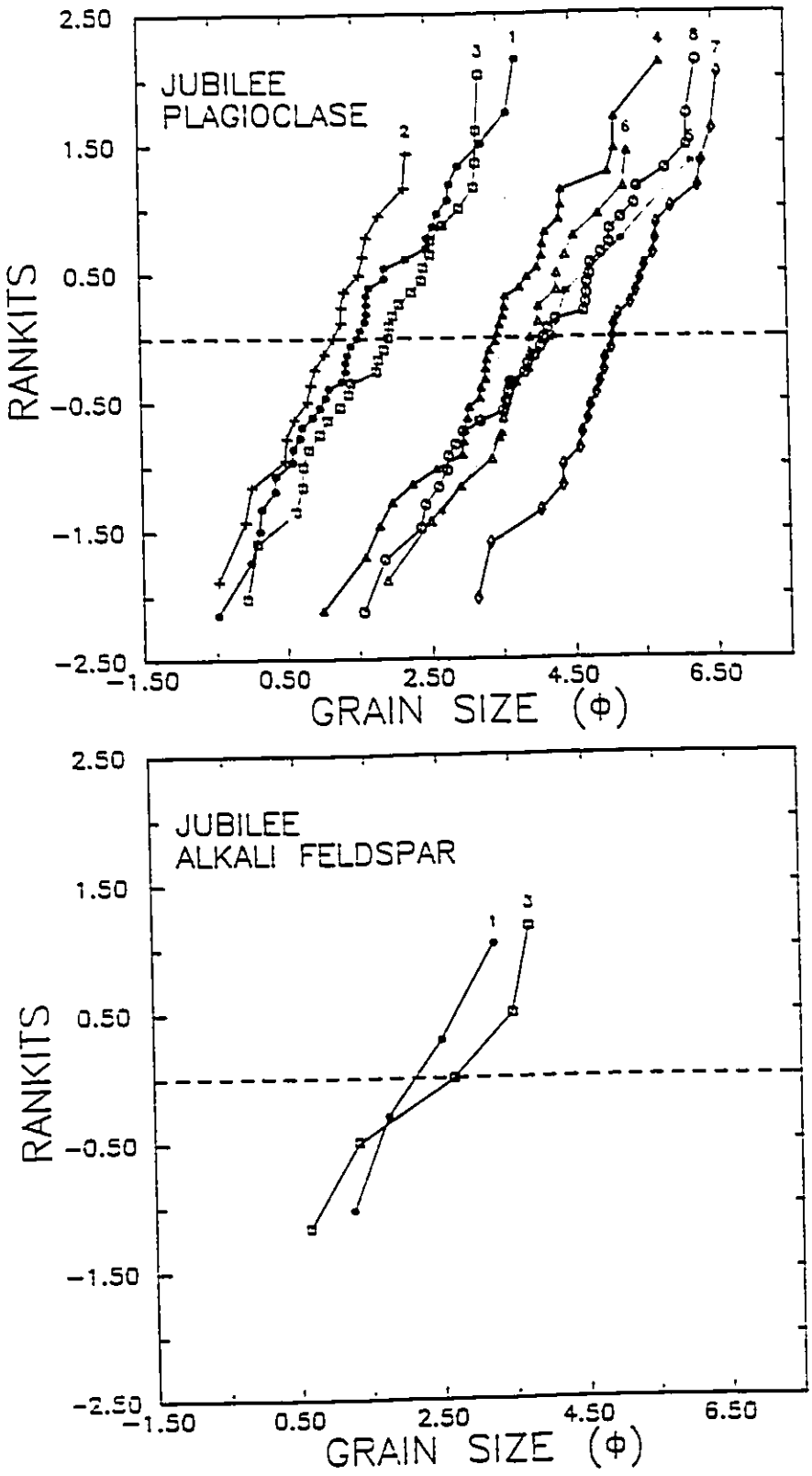

Fig.8. Cumulative frequency grain-size distribution of plagioclase and alkali feldspar in rocks associated with the Jubilee shear zone.

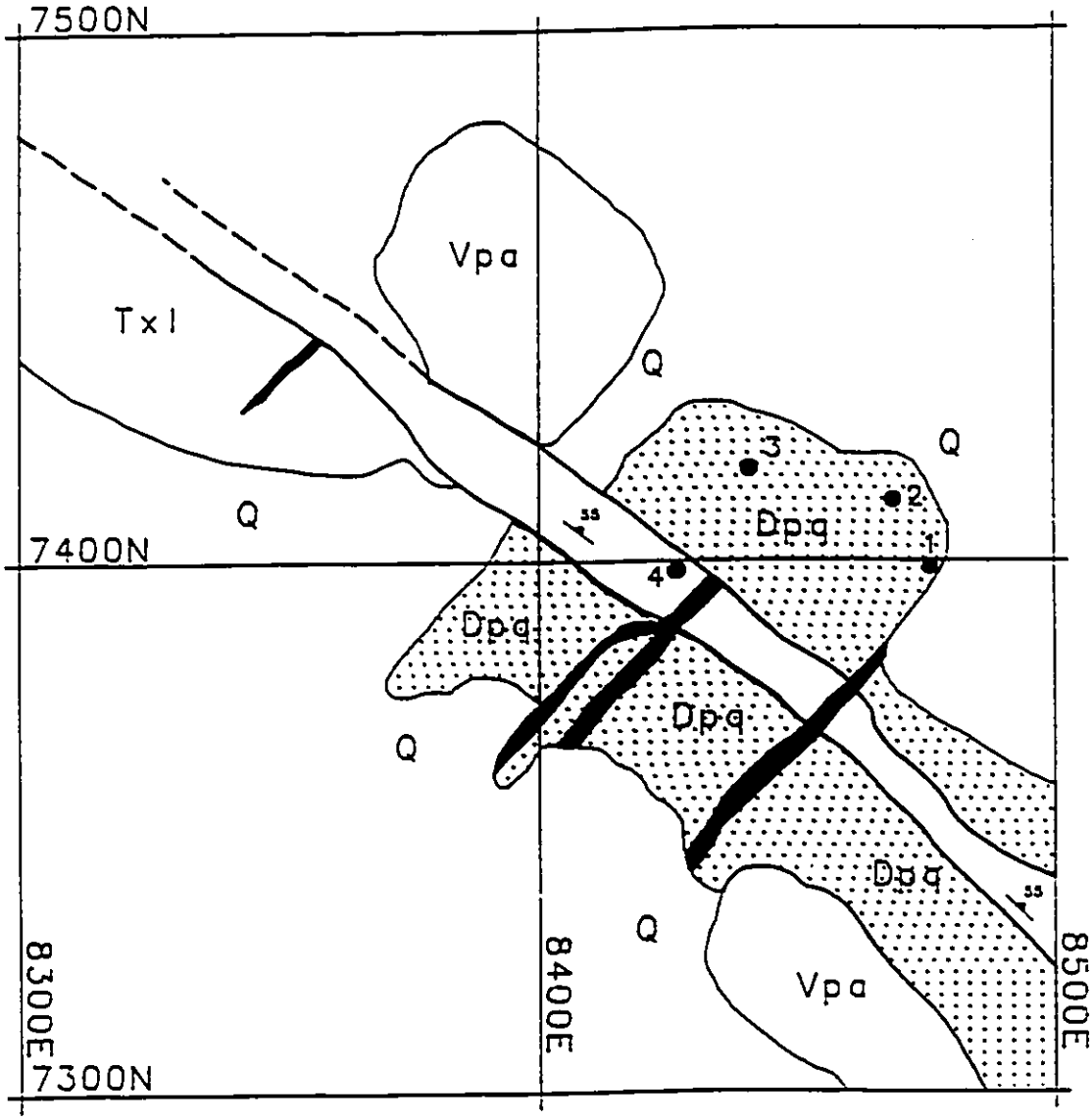

Fig.9. Map showing geology and sample locations of the Minto A shear zone. Txl = crystal tuff; Vpa = porphyritic andesite; Dpq = porphyritic quartz diorite; Q = Quaternary sediments; solid regions = lamphyrophyre dikes.

crystals appear to become progressively more strained, first exhibiting undulose extinction, and then grain size reduction by recrystallization. Opaques appear concentrated along feldspar grain edges and within chlorite grains.

MA-90-4 consists of fine-grained muscovite, quartz, chlorite calcite, epidote, and small anhedral grains of plagioclase, with trace amounts of opaques. It is well-foliated with visible patches of muscovite + quartz and chlorite + calcite + quartz.

Figure 10 shows variations in plagioclase and alkali feldspar grain sizes across the Minto A shear zone. Statistical analysis of this data is provided in Table 8 (Appendix B). There is a very abrupt change in grain-sizes between samples MA-90-3 and MA-90-4. Alkali feldspar grains are few in number and are not as well sorted as plagioclase feldspar.

Minto C

The Minto C shear zone is located approximately 2.5 km southeast of the town of Wawa. It is a narrow shear zone with a foliation at 045°/50°SE. Six samples were taken from a cross-sectional traverse over a distance of 10 meters, from one edge of the shear zone to the other (Figure 11).

Modal analyses of samples from the Minto C shear zone are given in Table 9 (Appendix B). The protolith is a porphyritic quartz diorite. It consists of plagioclase (oligioclase), quartz, biotite, and retrograde chlorite and epidote, with trace amounts of opaques. The feldspar grains are extensively replaced by epidote, although some zoning can be distinguished in thin section.

Within the deformation zone, feldspar alteration to quartz + chlorite ± calcite or quartz + muscovite increases. Foliation development is defined by the preferred orientation of the phyllosilicates. Progressive grain-size reduction of feldspar by alteration and brittle fracturing is accompanied by quartz grain-size reduction by recrystallization.

MC-90-3 is the most intensely deformed sample in the suite. It contains 7% calcite

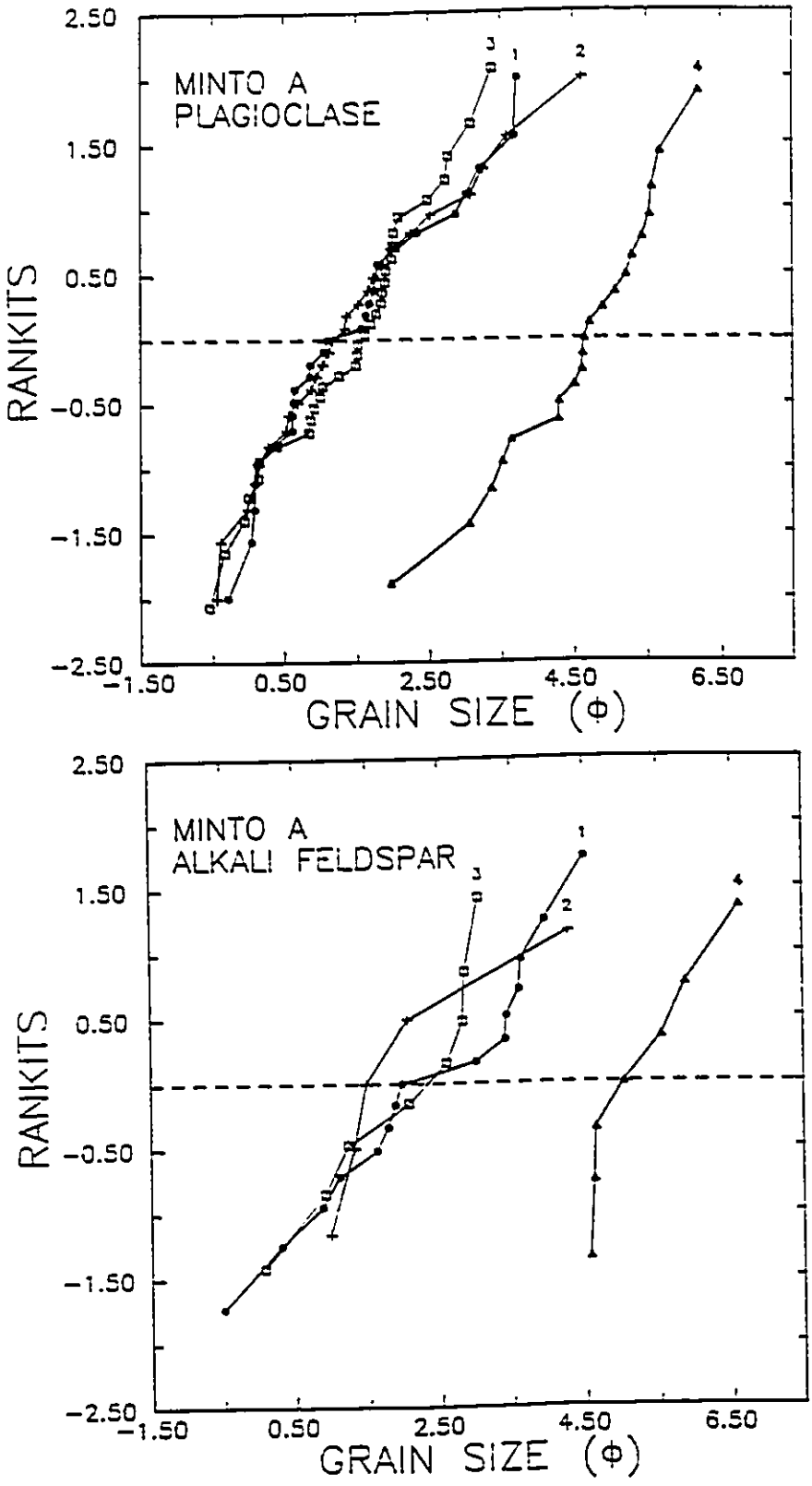

Fig.10. Cumulative frequency grain-size distribution of plagioclase and alkali feldspar in rocks associated with the Minto A shear zone.

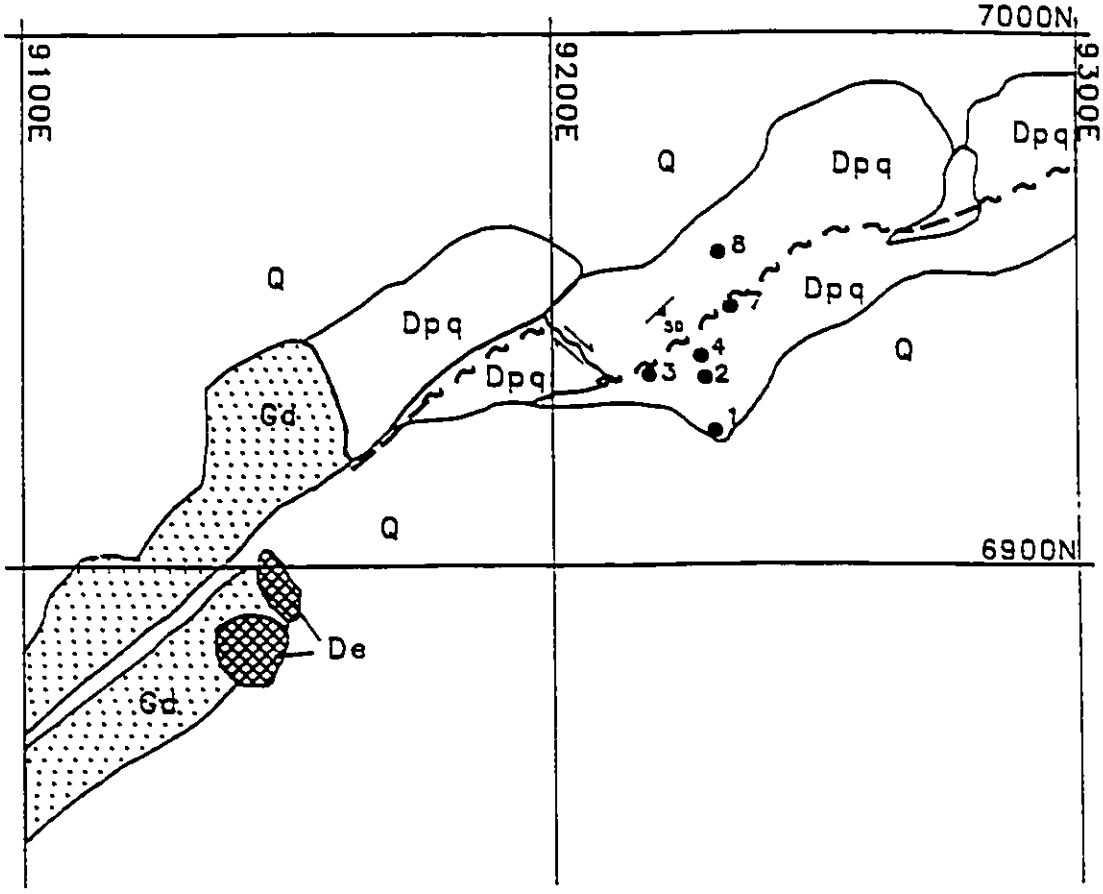

Fig.11. Map showing geology and sample locations of the Minto C shear zone. Dpq = porphyritic quartz diorite; De = augen diorite; Gd = granodiorite; Q = Quaternary sediments. Shear zone indicated by shear pattern; fault offset indicated by arrows.

in granular aggregates which are wrapped by the foliation. The rock has a well-developed anastomosing mylonitic fabric defined by muscovite and chlorite, opaques and small recrystallized quartz augen. It contains only 5.7% plagioclase grains, which are small and rounded, and have been largely replaced by epidote. No biotite occurs in this sample.

MC-90-4 has large quartz augen wrapped by a matrix of fine-grained muscovite + quartz + opaques. Relict plagioclase grains account for only 7.8% of the sample and are found in the muscovite matrix.

Figure 12 illustrates the plagioclase grain-size distribution in samples from the Minto C shear zone. Statistical analysis of this information is given in Table 10 (Appendix B). The progressive decrease in grain-size corresponds to increasing degree of deformation within the shear zone. Generally, grain-size distributions are unimodal. MC-90-3 has the highest matrix/porphyroblast ratio and and the smallest median feldspar grain-size and is therefore the most deformed rock in the zone. MC-90-1 and MC-90-8 are both protoliths, from the south and the north margins of the shear zone, respectively.

Minto E

This narrow shear zone is located approximately 3 km southeast of the town of Wawa. It strikes 050° and dips steeply to the northwest. Five samples were taken over a traverse perpendicular to foliation over a distance of 13 meters (Figure 13). The modal analyses of Minto E are presented in Table 11 (Appendix B). The protolith is a volcanic rock with the composition of dacite. Biotite patches are visible in hand specimen. In thin section, the protolith contains plagioclase feldspar, quartz, biotite, retrograde chlorite, and minor calcite and opaques. Extensive epidotization of the plagioclase phenocrysts has occurred, making the composition of the feldspar difficult to determine.

The deformed rocks in the shear zone appear more felsic than their protolith in hand specimen. In thin section, some samples show significant sericite and epidote alteration of

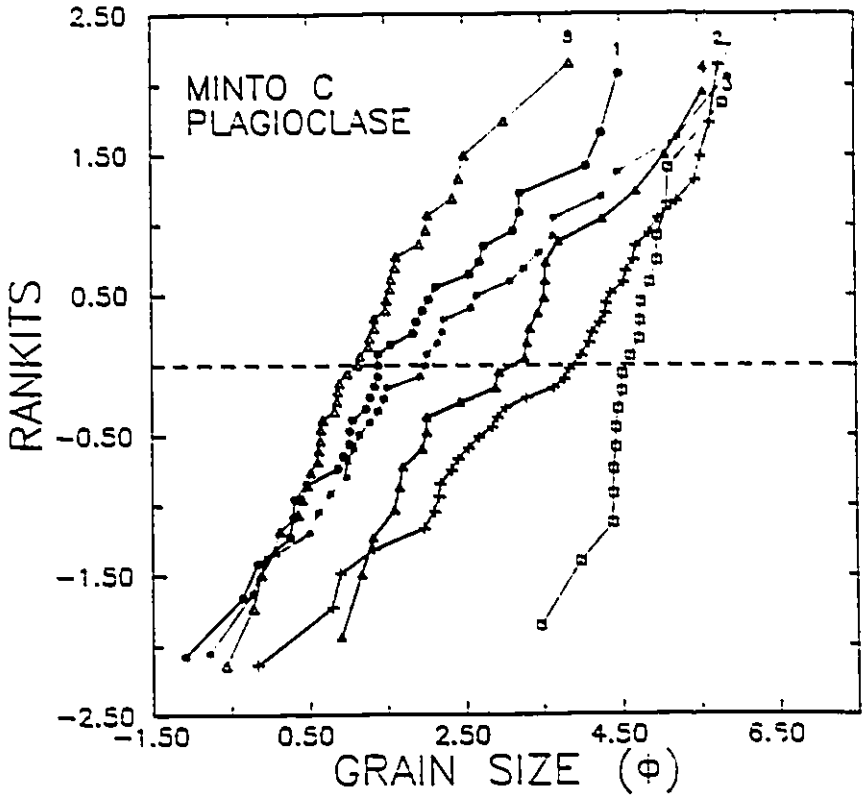

Fig.12. Cumulative frequency grain-size distribution of plagioclase feldspar in rocks associated with the Minto C shear zone.

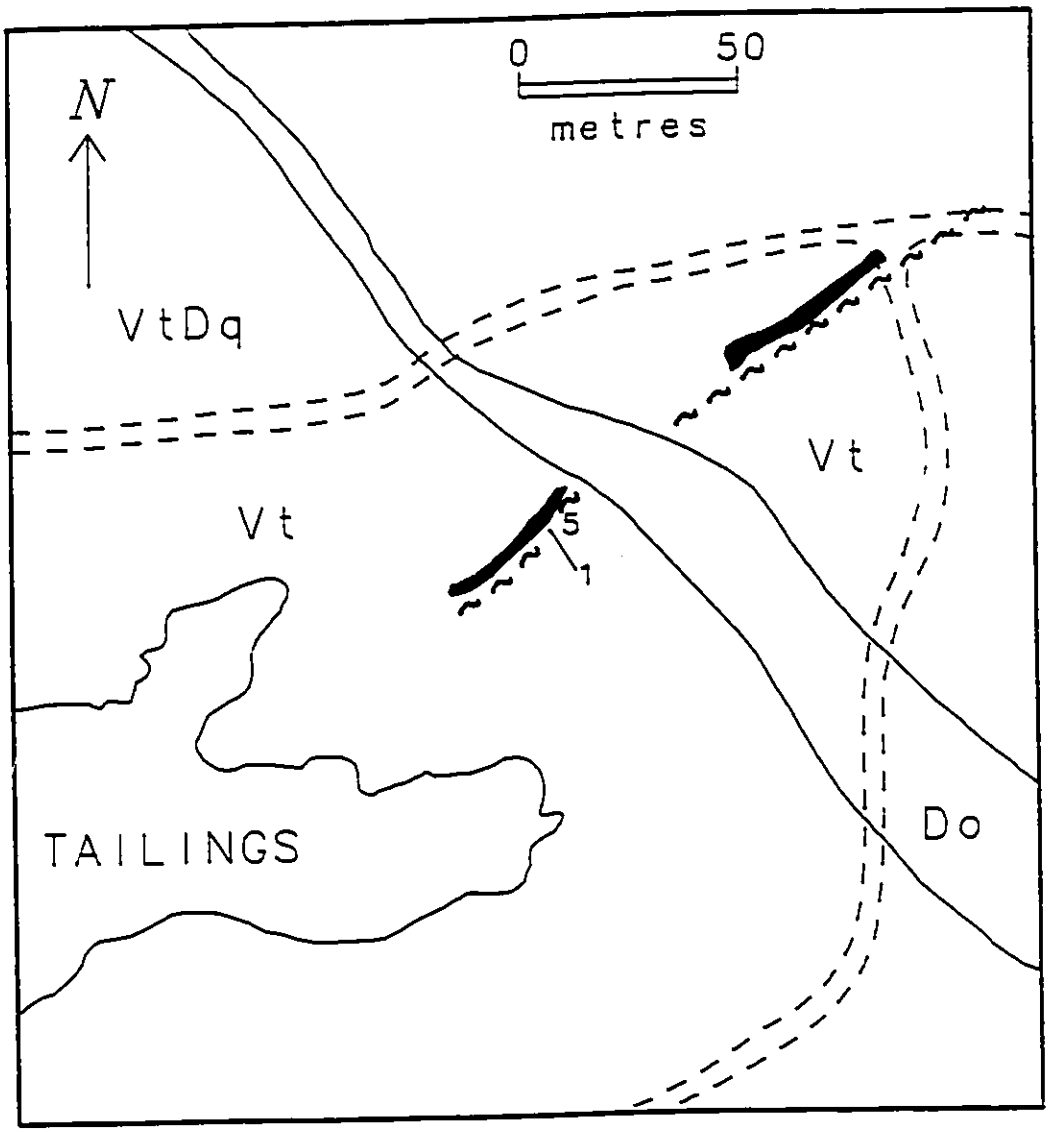

Fig.13. Map showing geology and sample locations of the Minto E shear zone. Do = dolerite; Vt = volcanic tuffs; VtDq = volcanic tuffs with augen diorite; solid regions = lamprophyre dikes. Shear zone indicated by shear pattern. Samples ME-90-1 through ME-90-5 taken across shear zone where indicated.

feldspar grains, and extensive pseudomorphing of biotite by chlorite. Some pods of highly twinned calcite occur in ME-90-3. Accumulations of opaques along foliation planes and the presence of large, cubic opaque crystals were observed in ME-90-5.

With increasing degree of deformation, there is a decrease in the modal amount of feldspar. Retrogradation of biotite to chlorite also becomes more pronounced, decreasing the ratio of biotite to chlorite. Minor pyrite is visible in some samples in hand specimen. ME-90-4 is the most highly-deformed rock. It exhibits a well-developed foliation, defined by muscovite, biotite, chlorite and opaques.

Figure 14 illustrates the cumulative frequency grain-size distributions of plagioclase feldspar in rocks associated with the Minto E shear zone. Statistical analysis of this data is presented in Table 12 (Appendix B). An abrupt decrease in grain-size is evident in ME-90-4, and represents a transition from protomylonite to ultramylonite.

Parkhill East

The Parkhill shear zone is located approximately 3.5 kms SE of the town of Wawa. The shear zone was sampled in two localities; one suite was taken from the eastern pit and one from the western pit near the former mine site (Figure 15). In the Parkhill East exposure, the foliation strikes approximately 060° and dips 45°SE. Offset horizons indicate dextral displacement along the Parkhill shear. Eight samples were taken across the shear zone approximately perpendicular to the foliation over a distance of 7.5 meters.

The modal analyses of the samples from the eastern exposure are given in Table 13 (Appendix B). The protolith is a crystal tuff of dacitic composition with biotitic alteration. It consists of feldspar grains (oligioclase) with extensive epidote alteration, quartz, biotite, chlorite and accessory zircon. Samples PHE-90-2 and PHE-90-3 show slight foliation, and very extensive epidote alteration of the plagioclase grains. Calcite occurs in samples PHE-90-3 through PHE-90-8, although in minor amounts. Some calcite occurs in pods or augen

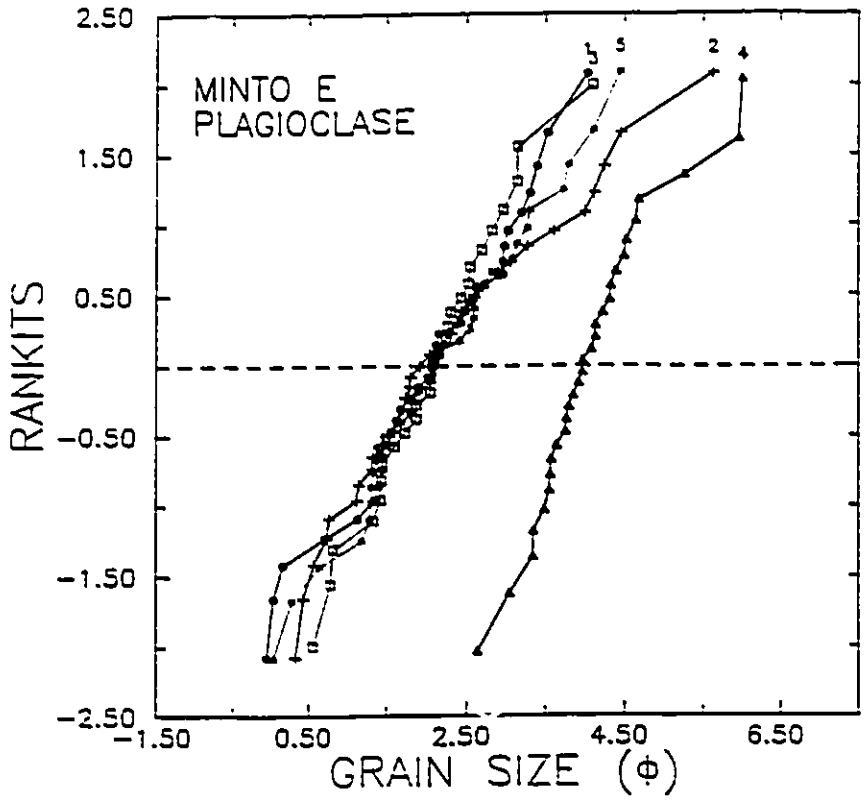

Fig.14. Cumulative frequency grain-size distribution of plagioclase feldspar in rocks associated with the Minto E shear zone.

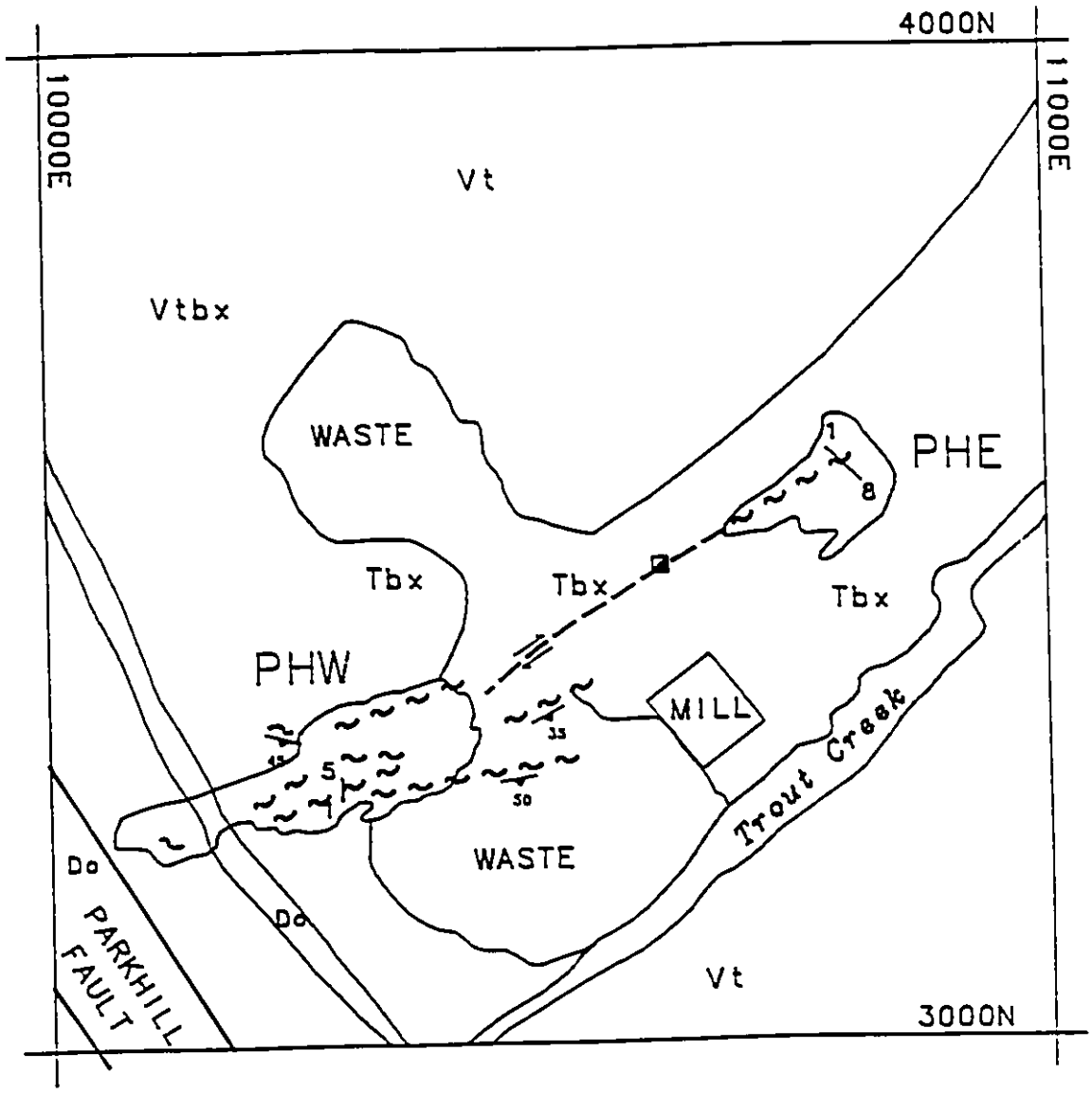

Fig.15. Map showing geology and sample locations of the Parkhill shear zone. Do = dolerite; Vt = volcanic tuffs; Tbx = brecciated tuffs; Vtbx = volcanic tuffs and brecciated tuffs. Shear zones are indicated by shear pattern. Samples PHE-90-1 through PHE-90-8 taken across the Parkhill East shear zone where indicated; samples PHW-90-1 through PHW-90-5 taken across the Parkhill West shear zone where indicated.

with coarse-grained quartz.

PHE-90-5 is well-foliated and has a gneissic texture. Bands of biotite + fine-grained quartz are separated from bands of epidote + fine-grained quartz by layers of coarse-grained quartz ± calcite.

Figure 16 plots grain size versus cumulative percent of plagioclase grains in rocks from the Parkhill East shear zone. Statistical analysis of this data is provided in Table 14 (Appendix B). Distributions are unimodal and a progressive decrease in feldspar grain-sizes reflects increasing degree of deformation.

Parkhill West

The west pit at the Parkhill site exposes another portion of the Parkhill shear zone. Here the shear zone strikes from 060° to 080° and dips up to 55° SE. Five samples were selected over a distance of 8.5 meters, from the protolith to the center of the shear zone (Figure 15). A lamprophyre dike on the eastern side of the deformation zone inhibited a full cross-sectional traverse. Fenitization from adjacent lamprophyre dike has resulted in the addition of a blue fibrous mineral to the assemblage. The mineral occurs as radiating aggregates, and is sometimes in association with calcite pods. The small size and habit of the mineral grains make accurate optical determinations difficult, but its association and habit suggests that it may be riebeckite.

Table 15 (Appendix B) contains the modal analyses of the samples collected from the western exposure at the Parkhill site. The protolith is very fine-grained pyroclastic of dioritic composition. It consists of quartz, feldspar, muscovite, biotite, chlorite, calcite, opaques, and trace amounts of opaques and zircon. Hematite alteration occurs along small brittle fractures.

PHW-90-2 contains a higher proportion of muscovite and calcite. Muscovite occurs in alteration patches on relict feldspar grains. A slight foliation is defined by the preferred

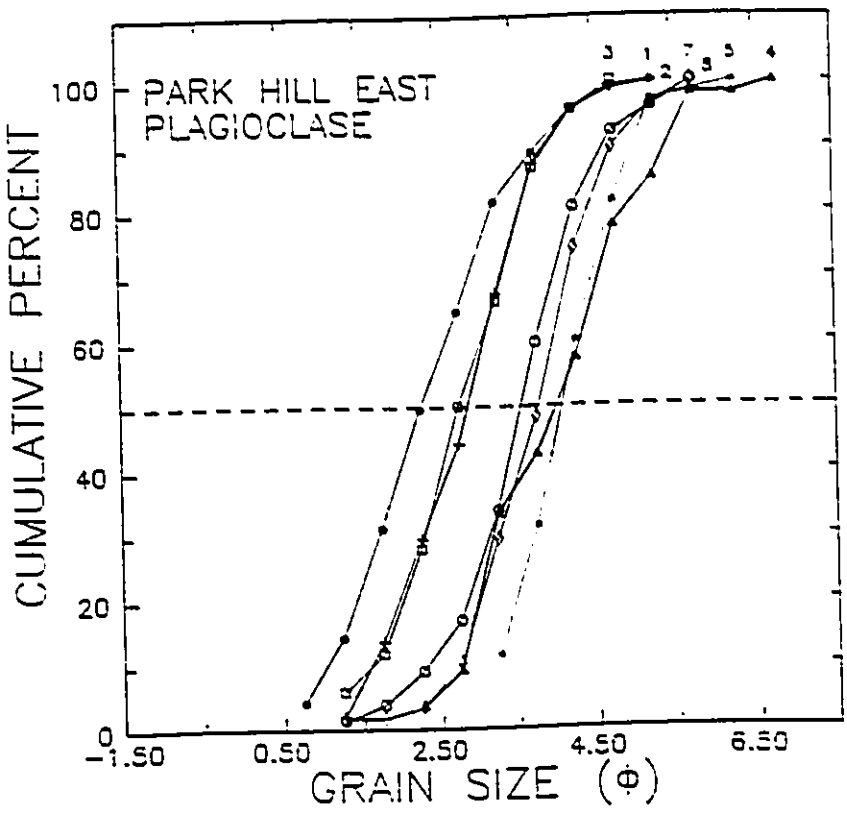

Fig.16. Cumulative frequency grain-size distribution of plagioclase feldspar in rocks associated with the Parkhill East shear zone.

orientation of muscovite grains. Pods of coarse-grained quartz and twinned calcite occur throughout the sample.

PHW-90-3 exhibits a well-developed fabric. Small rounded feldspar grains are wrapped by the foliation bands of muscovite + chlorite. Larger biotite grains appear to be rotated toward the foliation. Calcite veins cross-cut the fabric.

PHW-90-4 is a fine-grained sheared rock containing quartz, feldspar, bands of fine-grained muscovite, biotite, calcite, and opaques. This rock also contains 7.3% of the blue mineral (possibly riebeckite).

PHW-90-5 is contains lenses of finely crystalline quartz, bands of muscovite ± chlorite and patches of quartz + calcite.

Feldspar grain-size distributions are presented in Figure 17. Feldspar grain-sizes are very similar across the zone, and all of the rocks are very fine-grained. Table 16 (Appendix B) is the statistical analysis of filar grain-size measurements of the feldspars. No alkali feldspar occurs in samples PHW-90-4 and PHW-90-5.

Hydrothermal Alteration and Timing

The most prominent mineralogical features of hydrothermal alteration are the sericitization and epidotization of feldspar. These alterations are related to the influx of aqueous fluids in the regions of the shear zones. Evidence of CO_2-rich fluids exists in some of the rocks where secondary carbonate minerals exist. Other alteration features include the presence of late-stage biotite, introduction of sulphides ± gold, hematite alteration, minor fenetization and minor tourmaline alteration.

The alteration in several of the shear zones in this study has been studied by Bas (1992). He identifies up to five alteration events, and up to two deformation events. In sites adjacent to the Jubilee shear zone, he has identified an alteration event which pre-dates the deformation. This event is characterized by a quartz-chlorite-ankerite-muscovite-

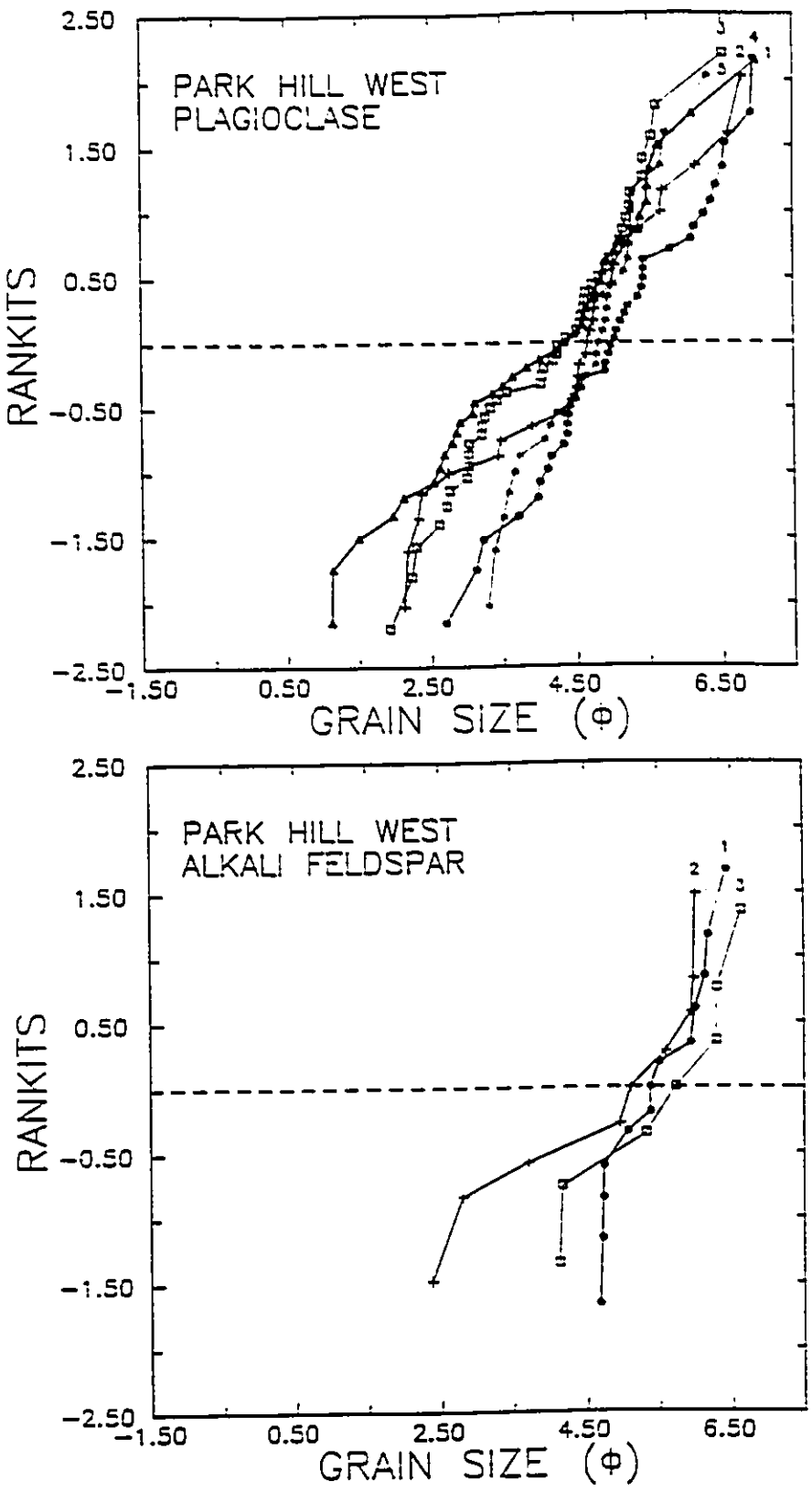

Fig.17. Cumulative frequency grain-size distribution of plagioclase and alkali feldspar in rocks associated with the Parkhill West shear zone.

pyrite assemblage and is temporally associated with auriferous quartz veins. Later alteration events include an ankerite-hematite-kaolinite assemblage and chloritic alteration.

In the Minto A shear zone, early alteration is characterized by an assemblage of quartz-muscovite-ankerite-pyrite-feldspar. Post-deformation alteration includes a chlorite-ankerite-tourmaline assemlage, hematite-kaolinite alteration and late-stage fenetization associated with the intrusion of lamprophyre dikes (Bas, 1992).

Three alteration events have been characterized in the Minto C shear zone (Bas, 1992). The earliest alteration assemblage of quartz-muscovite-chlorite-ankerite-feldspar is pre- or syn-deformation. The second alteration event is an ankerite-hematite assemblage, which was followed by a later biotite alteration.

Originally felsic protoliths in the Minto E shear zone contain an alteration assemblage of quartz-muscovite-ankerite-chlorite-biotite-feldspar which is pre- or syn-deformation. Post-deformation alteration is marked by ankerite-hematite assemblages (Bas, 1992).

The relationship of deformation and mineralization is complex and variable throughout the study area. Petrographic evidence points to multiple alteration and perhaps multiple deformation events. Chemical patterns associated with deformation can be distinguished from those related to mineralization and the resultant patterns may be used to determine temporal relationships between mineralization and deformation.

There is petrographic evidence for a pre-deformation or syn-deformation alteration characterized by the addition of sulphides and gold. In many of the foliated rocks, opaque phases parallel the foliation. Some of these samples contain abundant opaques and have anomalous values of As, Cu and sometimes Au. This indicates that mineralization occurred prior to or during the main deformation. Bas (1992) found that gold-bearing vein systems related to this event contained CH_4-rich fluid inclusions.

CHAPTER 5

CHEMICAL STUDIES

Theoretical Background

Gresens (1967) developed a series of mathematical equations to illustrate the relationships between composition and volume changes during metasomatic alteration. His theory is based on a general assumption that some elements are immobile during the metasomatic process. For those components, the ratios of concentrations in the original and altered samples are the same and the ratio is used as an independent constraint to calculate the mass or volume loss that has occurred. Gresens' equations allow the chemical analyses of rocks to be readily used to assess the gains and losses that occurred during metasomatism. Using the specific gravities and the chemical analyses of the unaltered and altered rocks, volume changes, and gains and losses of constituent components may be identified. The general equation derived by Gresens may be written as:

$$100\ [f_v\ (\rho^i/\rho^f)\ C_n^f - C_n^i] = W_n \qquad (4)$$

where i and f refer respectively to the unaltered (initial) and altered (final) samples, ρ is the specific gravity, C_n is the weight fraction of component n, f_v is the volume factor, and W_n is the total amount of material lost or gained (in grams). Because analyses commonly add up to 100 weight percent the term 100 is arbitrarily chosen to represent the weight in grams of the unaltered rock.

Grant (1986) developed a graphical solution to Gresens' (1967) equations to compare the chemistry of altered and unaltered rocks. By relating Gresens' equations directly to mass, he derived the equation:

$$C_n^f = M^i/M^f\ (C_n^i + \Delta C_n), \qquad (5)$$

where C_n^f is the concentration of component n in the altered sample, C_n^i is the concentration of the same component in the original unaltered sample, ΔC_n is the change in concen-

tration of component n, M^i is the reference mass of the original sample, and M^f is the mass of the altered sample.

By plotting C_n^f against C_n^i for elements 1...n, the immobile components generate a straight line through the origin. All points on this line have a constant ratio of (M^i/M^f), and therefore $\Delta C_n = 0$. The slope of this line, the isocon, defines the mass change that occurred during the alteration. The equation of the isocon as given by Grant (1986) is:

$$C^f = (M^i/M^f)C^i. \qquad (6)$$

If constant mass is assumed,

$$C^f = C^i. \qquad (7)$$

If constant volume is assumed,

$$C^f = (\rho^i/\rho^f)C^i, \qquad (8)$$

where ρ^i is the specific gravity of the original sample and ρ^f is the specific gravity of the altered sample. Where the ratios of specific gravities of the unaltered and altered samples is small, the isocon can be said to very closely approximate a line of constant volume.

By plotting the concentrations of components in the original protolith against their concentrations in the altered rocks, an isocon line can be drawn though the immobile elements. The slope of this line may then used to estimate the amount of volume loss that has taken piace, using the following equations:

$$C^iV^i = C^fV^f \qquad (9)$$

where V^i is the initial volume of the protolith, and V^f is the final volume of the altered rock. The volume change represented by the new isocon is then given by:

$$C/C_i = 1/(1 + \Delta) \qquad (10)$$

where $\Delta = (V_f - V_i)/V_i$, the fractional volume loss.

Olsen and Grant (1991) defined four important sources of uncertainties which may contribute to scatter of the data points about the isocon. They are a) the choice of the protolith, b) the choice of the altered rock, c) the degree to which a component is immobile

and d) analytical errors. The method of sampling in this study reduces the likelihood of errors in the choice of protolith and altered equivalents, because the samples were all taken from continuous outcrops. Some suites, however, display heterogeneity in the chemistry and mineralogy of protolith samples. The degree of immobility of some components may be variable, but some components are generally assumed to be highly immobile, and these can be used as a guide.

O'Hara (1988, Figure 7) found that, in mylonite zones, refractory elements such as Ti, Y, V, Zr lay within the field of enrichment, while other components such as SiO_2, Al_2O_3, K_2O, Na_2O, and CaO remain constant, i.e., lie close to the isovolumetric line. Since it is highly unlikely to have enrichments of insoluble components without accompanying large enrichments of the soluble components, O'Hara constructed an isocon of higher slope, passing through those elements considered to be immobile and representing a volume-loss. All elements lying below the isocon, including Si, Al, Ca, K and Na, were assumed to be mobile and depleted from the system. The loss of silica and alkalies are explained by fluid-transport processes accompanying the breakdown of alkali feldspar to muscovite. Using the slope of the isocon, O'Hara and Blackburn (1989) estimated volume loss on the order of 60% or more for the Fries Fault of North Carolina and Virginia.

Where later alteration overprints the chemical effects accompanying deformation, the isocon can only yield an estimate of the minimum volume loss because of possible addition of components during metasomatism.

A line of unit slope passing through the origin is the line of constant mass, which closely approximates the line of constant volume given that density changes during alteration are generally very small. Components will plot along this line if there has been no net changes in their concentrations between the protolith and the mylonitic rock under isovolumetric conditions. If there has been no change in volume, components plotting above this line lie within the field of enrichment (i.e., they are enriched in the altered rock

relative to the protolith), and those plotting below this line lie within the field of depletion. Where there is more than one sample of a particular rock type, the average concentrations of each component in those samples are reported. On the isocon diagrams, error bars are drawn to represent one standard deviation from the mean of the sample values. These error bars do not represent analytical error.

Relative concentrations of the immobile elements are used to construct a second isocon representing constant composition accompanying a change in volume. Where this isocon has a slope greater than one, a loss of volume is inferred. The amount of volume change is calculated using the slope of the isocon drawn and equations (9) and (10). Any components plotting above the second isocon lie within the true field of enrichment and any components plotting below lie within the true field of depletion.

The development of broad alteration haloes is associated with mineralization, and is the premise on which geochemical exploration is based. Mineralization in the Wawa area is generally characterized by additions of Si, K, Rb, Ba, As, Cu, Au and sometimes Zn. Chemical enrichments of these components over a relatively broad area indicate alteration by mineralizing fluids. If this pattern is truncated by the chemical patterns related to deformation and volume loss within shear zones, a temporal relationship may be indicated where early mineralization is overprinted by later deformation. If the expected patterns of enrichment of refractory components and depletion of soluble components in deformed rocks is overprinted by enrichments of components associated with mineralization, it may be implied that deformation occurred prior to or was synchronous with mineralization along permeable conduits within the shear zone. The combined effects of alteration events result in complex chemical patterns across the shear zones.

Methods

Whole-rock major, minor, and trace element data complement the petrographic

studies and can be used to monitor the chemical changes that have occurred in association with shear zone development and hydrothermal alteration and mineralization.

Sample preparation was performed at the University of Windsor facilities. The rocks were first washed and trimmed using a diamond rock saw to remove weathered rinds. After slabs for thin sections were cut, the remainder of the sample was crushed using a Braun Jaw Crusher and then powdered to -200 mesh using a Spex shatterbox. The powder was homogenized and a representative sample of approximately 50 grams submitted to X-Ray Assay Laboratories for whole-rock analyses.

Major elements, minor elements and selected trace elements were determined by X-ray fluorescence spectrometry (XRF), induced coupled plasma spectrometry (ICP) or instrumental neutron activation analysis (INAA) techniques. Appendix D contains information on methods used for individual components, detection limits, accuracy and precision. The results are shown in Tables 19-26 (Appendix E).

Chemical variations across each shear zone are illustrated by variation diagrams in which the concentrations of selected components are plotted as the ordinate versus distance across the shear zone as the abscissa. It is assumed in every case, unless otherwise stated, that there was original homogeneity across the zone prior to deformation, although some minor differences in original rock chemistry could be expected to exist. Major and minor element oxides are reported in weight percent; trace elements are reported in parts per million, with the exception of gold which is reported in parts per billion. To accommodate all the relevant data, some components are scaled for presentation. It should be noted that changes in composition are exaggerated where the scale factor is greater than one and are supressed where the scale factor is less than one.

In each suite, approximate divisions between rock types determined petrographically are indicated by vertical dotted lines. Across the top of each graph, these domains are labelled as P_o for protolith, P for protomylonite, M for mylonite, and U for ultramylonite,

where they exist. On some diagrams, the label H is used to represent a domain of distinct hydrothermal alteration.

Isocon diagrams are plotted for each suite. On these, the concentrations of components in the protolith are plotted as the abscissa against the concentrations of the same components in the deformed rocks as the ordinate.

Chemistry of the Shear Zones

Fred C

Figure 18 is a plot of the components SiO_2, Al_2O_3, Na_2O, CaO, K_2O, TiO_2, P_2O_5, Sc and V against distance across the Fred C shear zone. The sampling traverse of over 220 meters began in the protolith and included a sequence of deformed rocks which are classified on the basis of feldspar grain-size data. FC-90-2 is a protomylonite, FC-90-4, FC-90-9 and FC-90-10 are mylonites, and FC-90-5 through FC-90-8 are ultramylonites. FC-90-6 has been subject to additional metasomatism. Sample FC-90-3 appears to belong to a different rock unit and therefore is not shown on the variation diagrams.

Generally, the proportions of SiO_2, K_2O and Na_2O_3 decrease with increasing degree of deformation. This chemical change is representative of the progressive breakdown of feldspar which is observed petrographically. The Al_2O_3 content increases slightly. CaO is highest in the most intensely deformed mylonites and ultramylonites.

The refractory components TiO_2, P_2O_5, Sc and V all are negatively correlated with SiO_2, exhibiting an increase in concentration with increasing degree of deformation. This pattern is attributed to the progressive enrichment of these immobile components as silica, K_2O and Na_2O are removed from the system during deformation.

Figure 19 is a plot of the patterns of TiO_2, CaO, $Fe_2O_3^*$, MgO, MnO, Zr, Zn, Cu, As and Au. Generally, the CaO pattern is correlated with that of the TiO_2, indicating that its behaviour is similar to the refractory components and its concentration is not controlled by

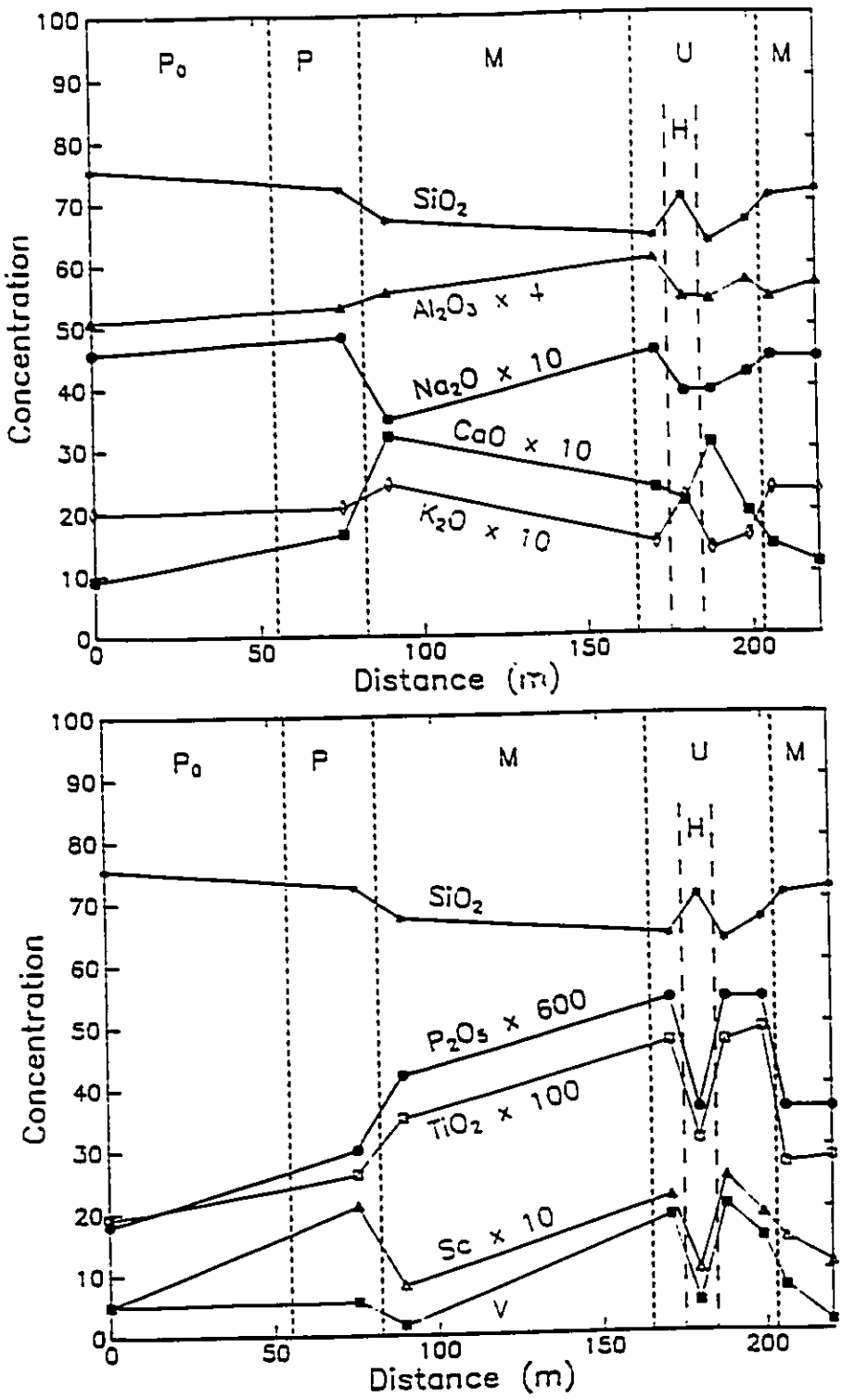

Fig.18. Plot of scaled concentrations of selected major and trace elements versus distance across the Fred C shear zone. Divisions between rock types are based on feldspar grain sizes (P_o = protolith; P = protomylonite; M = mylonite; U = ultramylonite; H = zone of hydrothermal alteration).

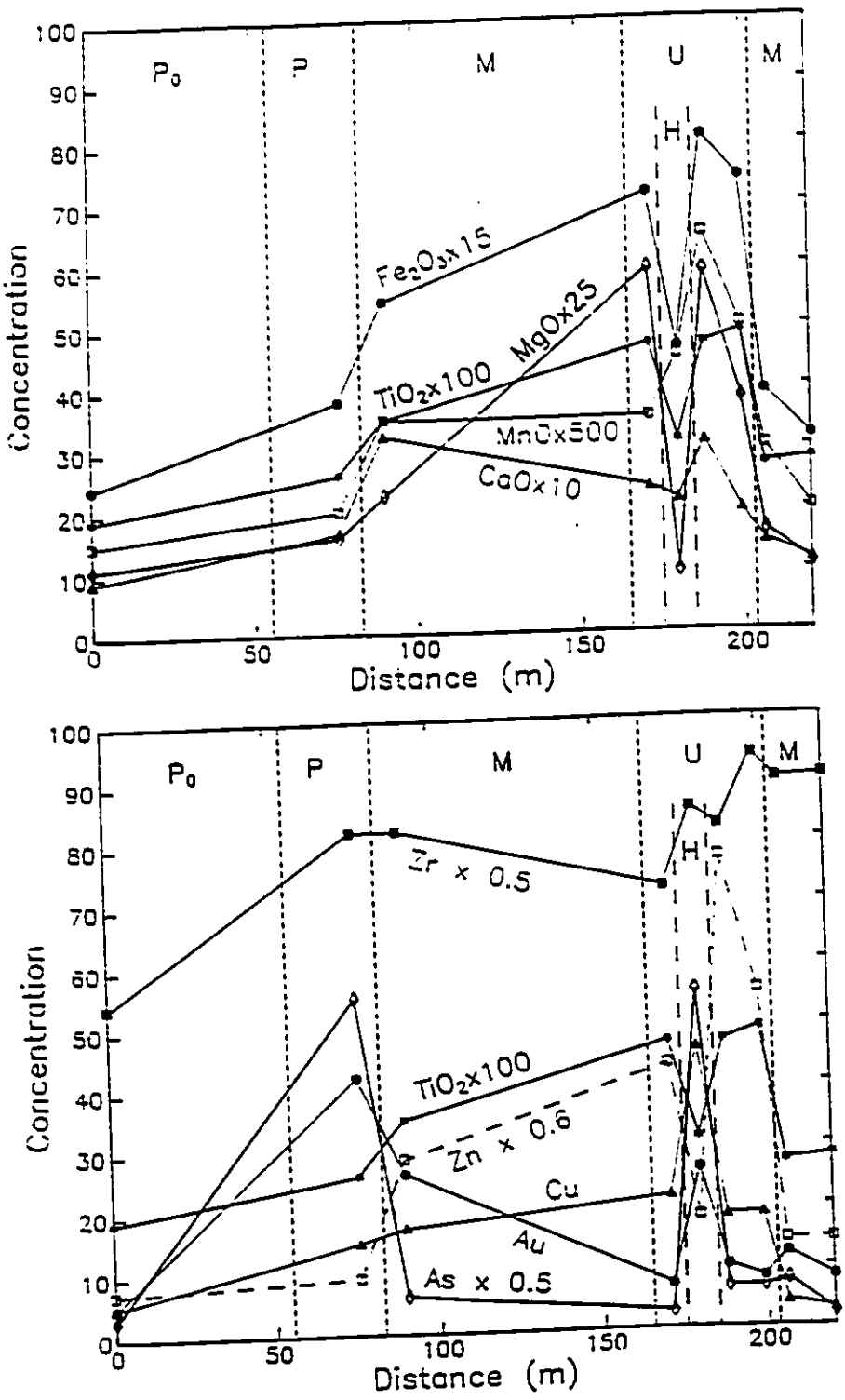

Fig.19. Plot of scaled concentrations of selected major and trace elements versus distance across the Fred C shear zone. Divisions and labels as in Fig.18.

feldspar dissolution. Fe_2O_3*, MgO and MnO also correlate well with TiO_2 and essentially act as refractory components, increasing in concentration as silica and the alkalies are removed from the deformed rocks. There is an overall increase in Zr and Zn within the deformation zone. Zn values are highest in the ultramylonites. Cu, Au and As all have peak values in samples FC-90-2 and FC-90-6, indicating minor hydrothermal alteration has locally added these components to the rocks.

Figure 20 is a Grant-type diagram (Grant 1986) for the major oxides and trace elements in rocks from the Fred C shear zone. Here, the concentrations of the oxides in the protolith (FC-90-1) are plotted against the average concentrations in the protomylonite (FC-90-2).

The line of unit slope through the origin represents a line of constant mass, and approximates constant volume. This line on Figure 20 passes close to components including Si, Al, Na, K, and Rb. All the components above this line would be inferred to be added to the system under isovolumetric conditions. This implies that components such as TiO_2, MnO, MgO, Fe_2O_3*, and Zr, were added to the system while relatively soluble components such as silica and the alkalies remained. Silica and the alkalies are some of the most soluble components (Holland and Malinin, 1979), and it is unlikely that they could remain undissolved while less soluble components were dissolved and removed.

A second isocon is therefore drawn on Figure 20 through those components considered to be immobile. This implies that components below this line, such as Al, K, Na, Rb, Sr, Ba, Y, Ni, Pb and Si were removed from the system. The loss of these soluble components would produce a residual enrichment in the immobile components, thereby explaining their apparent enrichment in the mylonites. The implied loss of silica and alkalies is consistent with the hydrolysis of feldspar observed petrographically.

The second isocon represents a change in mass and volume. The slope of this line is 1.31, which represents a dilation of -0.24 (from equations (9) and (10)). Thus, loss of

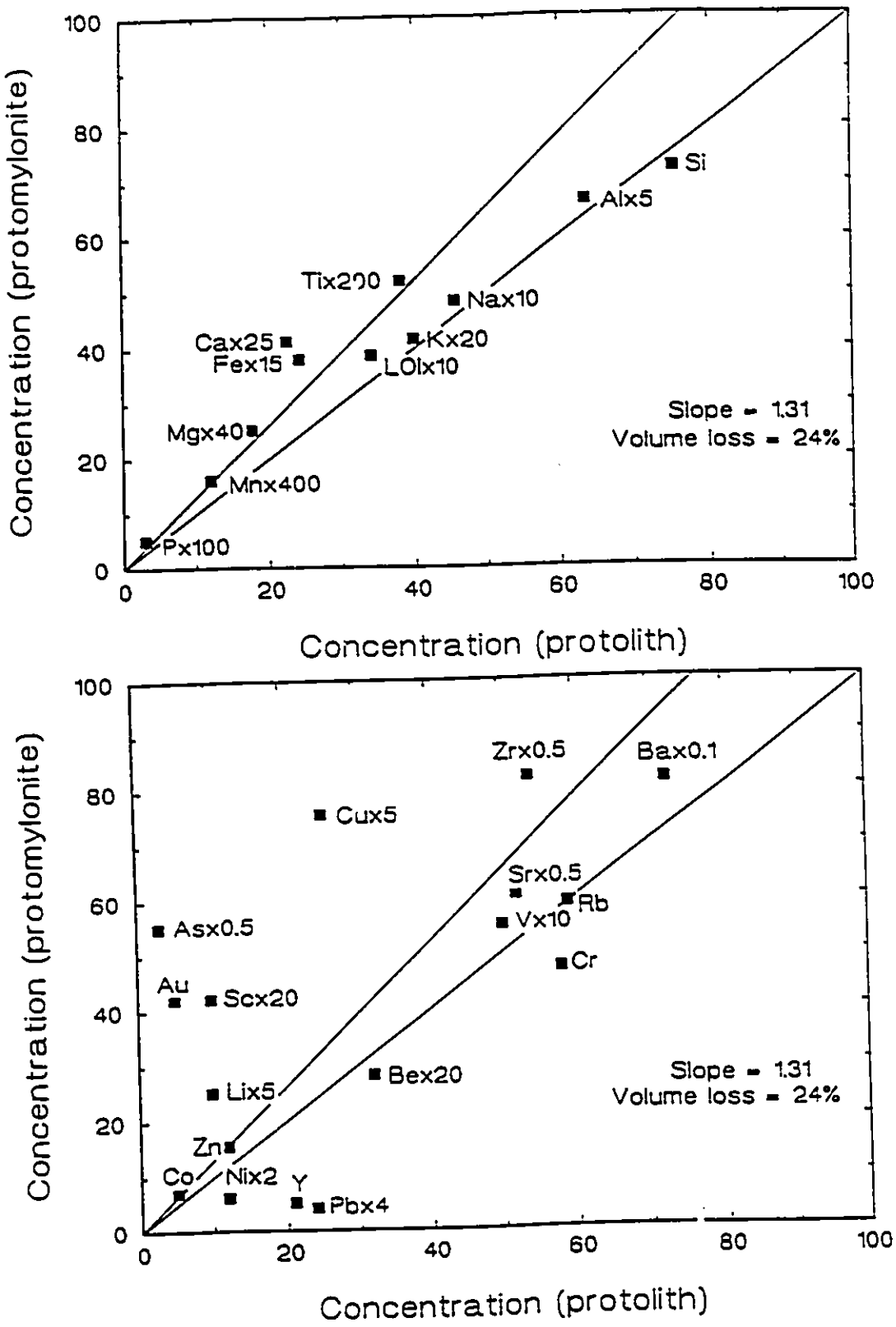

Fig.20. Plot of concentrations of major and trace elements in Fred C protomylonite versus concentrations in the protolith. An isocon line of slope 1.31 through elements assumed to be immobile represents volume loss of 24% in the protomylonite.

silica, alkalies, and accompanying minor and trace elements that occurred during deformation has resulted in a volume loss of 24%.

Figure 21 is a similar diagram for the major and trace element concentrations in the protolith versus their average concentrations in the mylonites (samples FC-90-4, FC-90-9 and FC-90-10). Once again a line of slope 1 representing a line of constant mass, and approximating an isovolumetric line is drawn for reference. HFSE such as Ti, P, Zr, Co, Ni, and other immobile components such as Cu, Pb, Zn, Mn, Fe, Mg, Sc and LOI define a second isocon of slope 1.63. This isocon represents a volume loss of 39% in the mylonites. Here, LOI may represent the amount of water that was added to the rocks in order to drive reaction (1) or (3) to form muscovite. Small enrichments in Au and Sc have occurred. Depletions in Si, Al, K, Na, Ba, Rb, Sr, Cr, V, Li, Be and Y imply mobility of these components.

Figure 22 is a plot of the average concentrations of major and trace elements in the ultramylonites (FC-90-5, FC-90-7, and FC-90-8) versus their concentrations in the protolith. The isocon line of slope 2.63 is based on relative enrichments of the HFSE Ti and P, and represents an average volume loss of 62% in the ultramylonites. Other elements are immobile in this system including Ca, Fe, Mg, Cu, Ni, Sc, and Co lie close to this isocon. Substantial depletions of Si, Al, Na, K, Ba, Rb, Cr, Be, Y, and Pb have occurred.

Grace Darwin

The sampling traverse at the Grace Darwin shear zone is shown in Figure 5. Figure 23 is a plot of the components SiO_2, Al_2O_3, CaO, Na_2O, K_2O, P_2O_6, TiO_2, Zn, Sc and V across the Grace Darwin shear zone. The rock types encountered include protolith and a sequence of deformed and hydrothermally altered rocks. The central zone labelled H contain rocks of variable strain and is the site of significant hydrothermal alteration, resulting in complex geochemical patterns and significant mineralogical variations. Outside this zone,

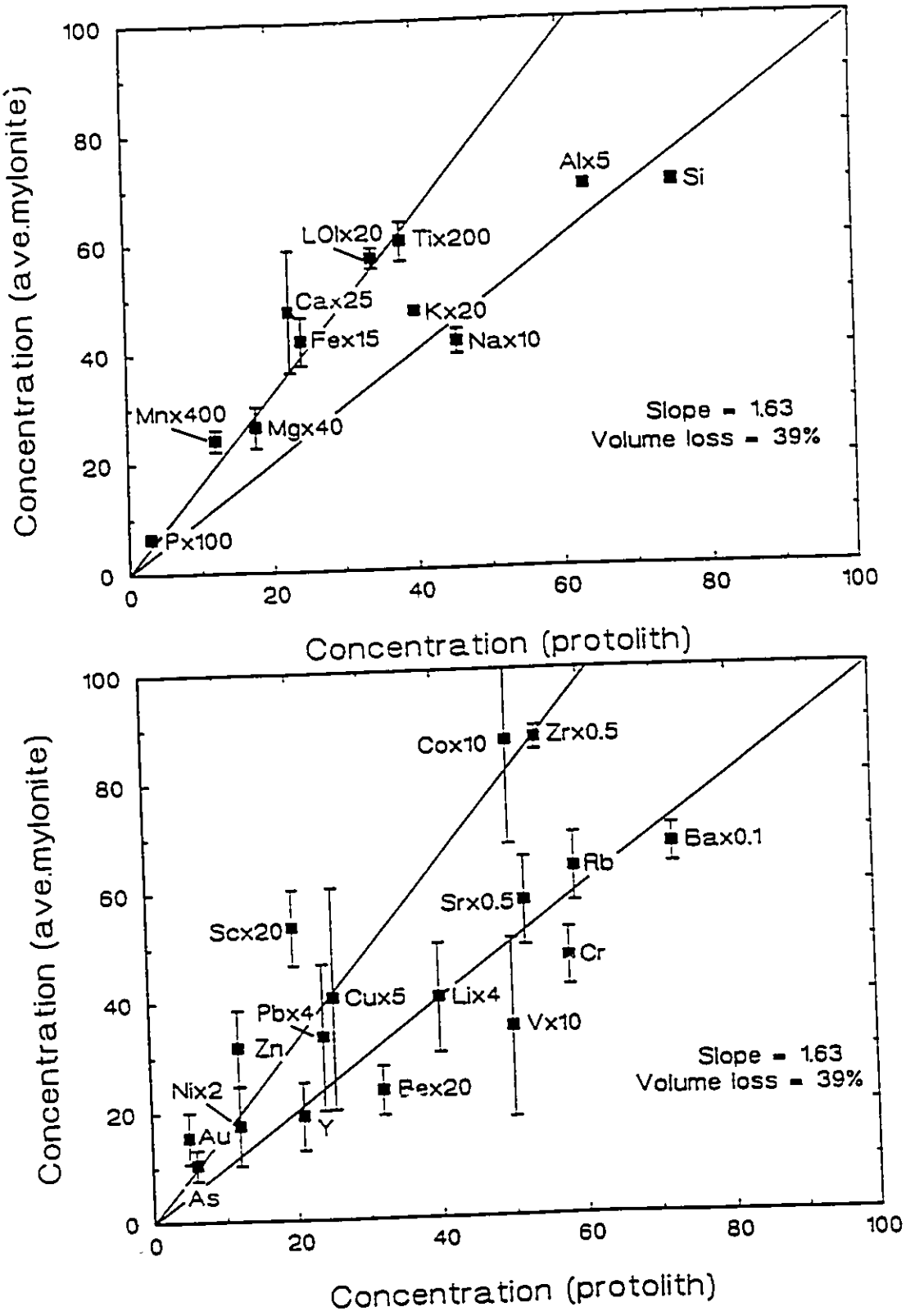

Fig.21. Plot of average concentrations of major and trace elements in Fred C mylonite versus concentrations in the protolith. Error bars represent one standard deviation. An isocon line of slope 1.63 through elements assumed to be immobile represents an average volume loss of 39% in the mylonites.

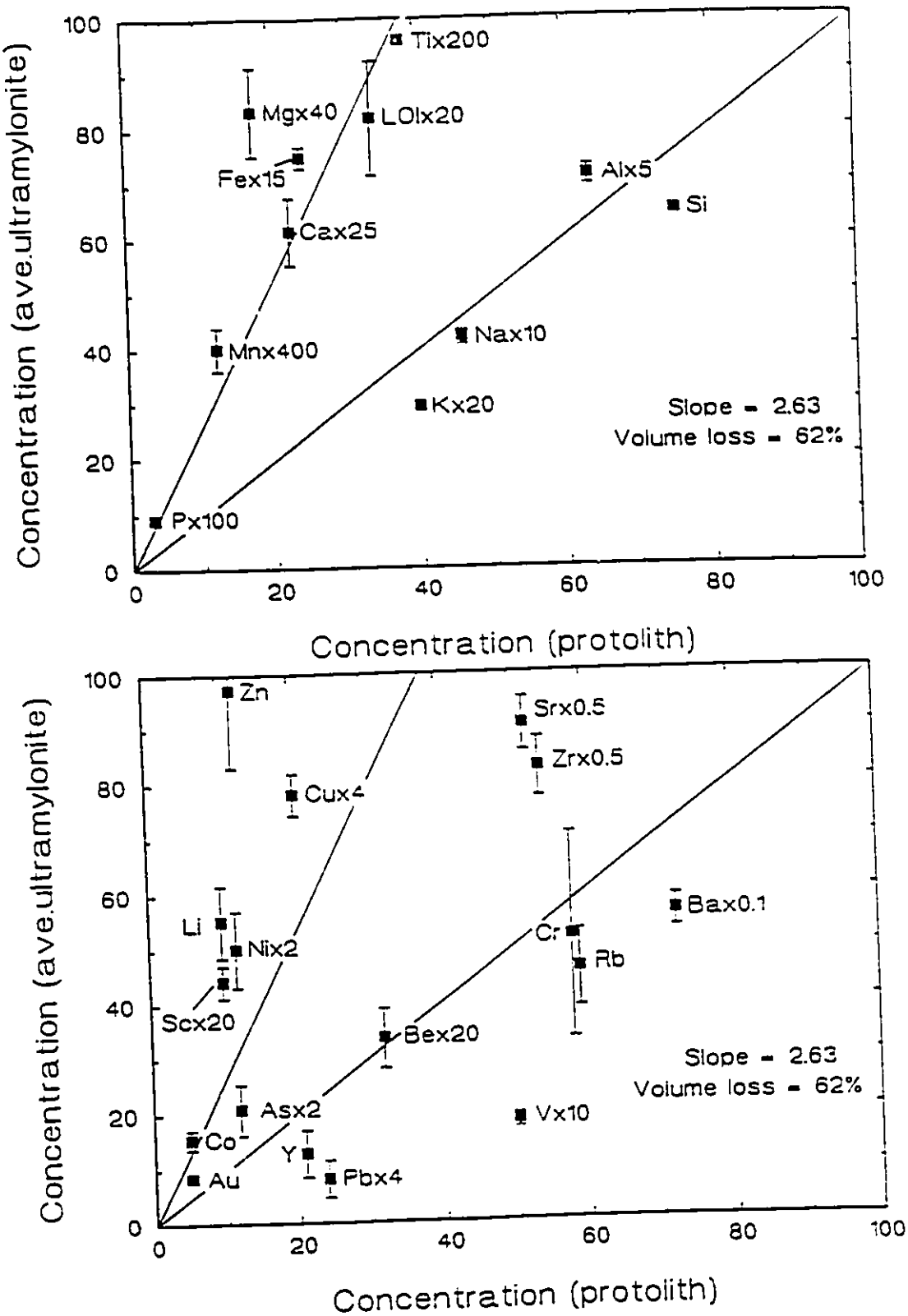

Fig.22. Plot of average concentrations of major and trace elements in Fred C ultramylonite versus concentrations in the protolith. Error bars represent one standard deviation. An isocon line of slope 2.63 through elements assumed to be immobile represents an average volume loss of 62% in the mylonites.

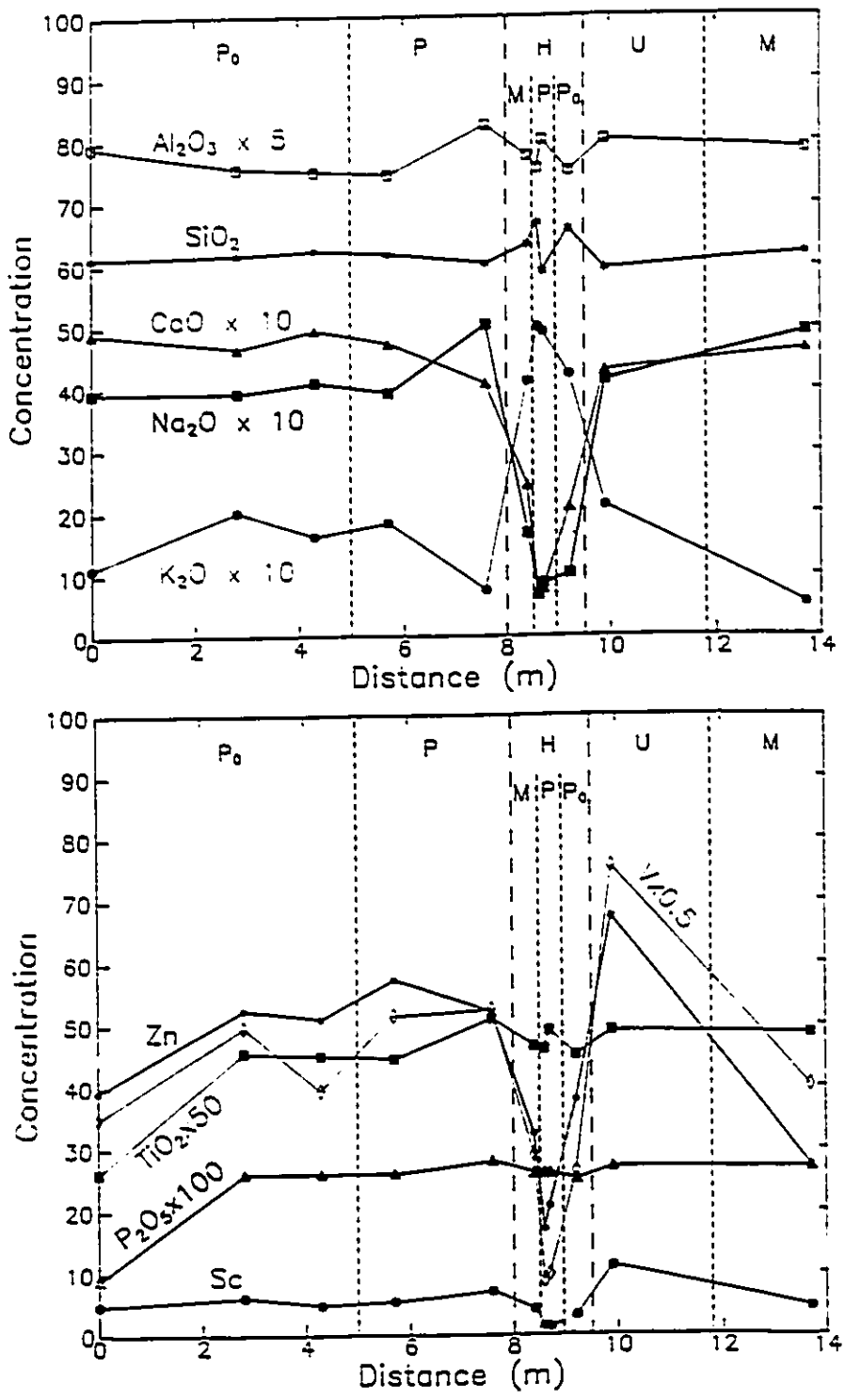

Fig.23. Plot of scaled concentrations of selected major and trace elements versus distance across the Grace Darwin shear zone. Divisions between rock types are based on feldspar grain sizes (P_o = protolith; P = protomylonite; M = mylonite; U = ultramylonite; H = zone of hydrothermal alteration).

protomylonites, mylonites and ultramylonites exist.

With increasing degree of deformation, there is a general decrease in the concentrations of SiO_2 except where the values are anomalously high within the zone of alteration. This is accompanied by a general decrease in the concentration of CaO, which becomes more pronounced in the central alteration zone H, and a decrease in the concentration of Al_2O_3. Na_2O is enriched in the protomylonites and mylonites, but is strongly depleted in the altered zone. K_2O is strongly enriched in the alteration zone, indicating significant potassic metasomatism. This is consistent with the observed loss of feldspar and increase in proportion of micas in these rocks.

The refractory components TiO_2, P_2O_6, V and Sc are negatively correlated with silica concentration. There is a general increase in the concentrations of the HFSE in the unaltered protomylonites and mylonites with increasing degree of deformation. Within the narrow zone of alteration, the patterns are more erratic. TiO_2 and P_2O_6 patterns are consistent in that they increase where SiO_2 decreases and are depleted where silica has been added hydrothermally. V and Sc have patterns similar to CaO, indicating that they were mobile within the hydrothermal system.

Figure 24 is a plot of the variations in concentrations of TiO_2, $Fe_2O_3^*$, MgO, MnO, CaO, Zr, Cu, As and Au. $Fe_2O_3^*$ and MgO both initially decrease in the protomylonites, and then increase in the mylonites. $Fe_2O_3^*$ is depleted in the zone of alteration, except for sample GD-90-8 which contains 12.7% opaques minerals, including pyrite, and possibly chalcopyrite and arsenopyrite. MgO is depleted in the alteration zone. MnO behaves similarly to the refractory components and is enriched in the unaltered protomylonites and mylonites, but significantly depleted in the alteration zone. The pattern of variation for Zr approximately parallels that of TiO_2, indicating its immobile nature. Cu, As and Au have anomalously enriched values in the zone of alteration, reaching peak values of 471 ppm Cu, 21 000 ppm As and 10 000 ppb Au, reflecting alteration fluids rich in copper, arsenic and

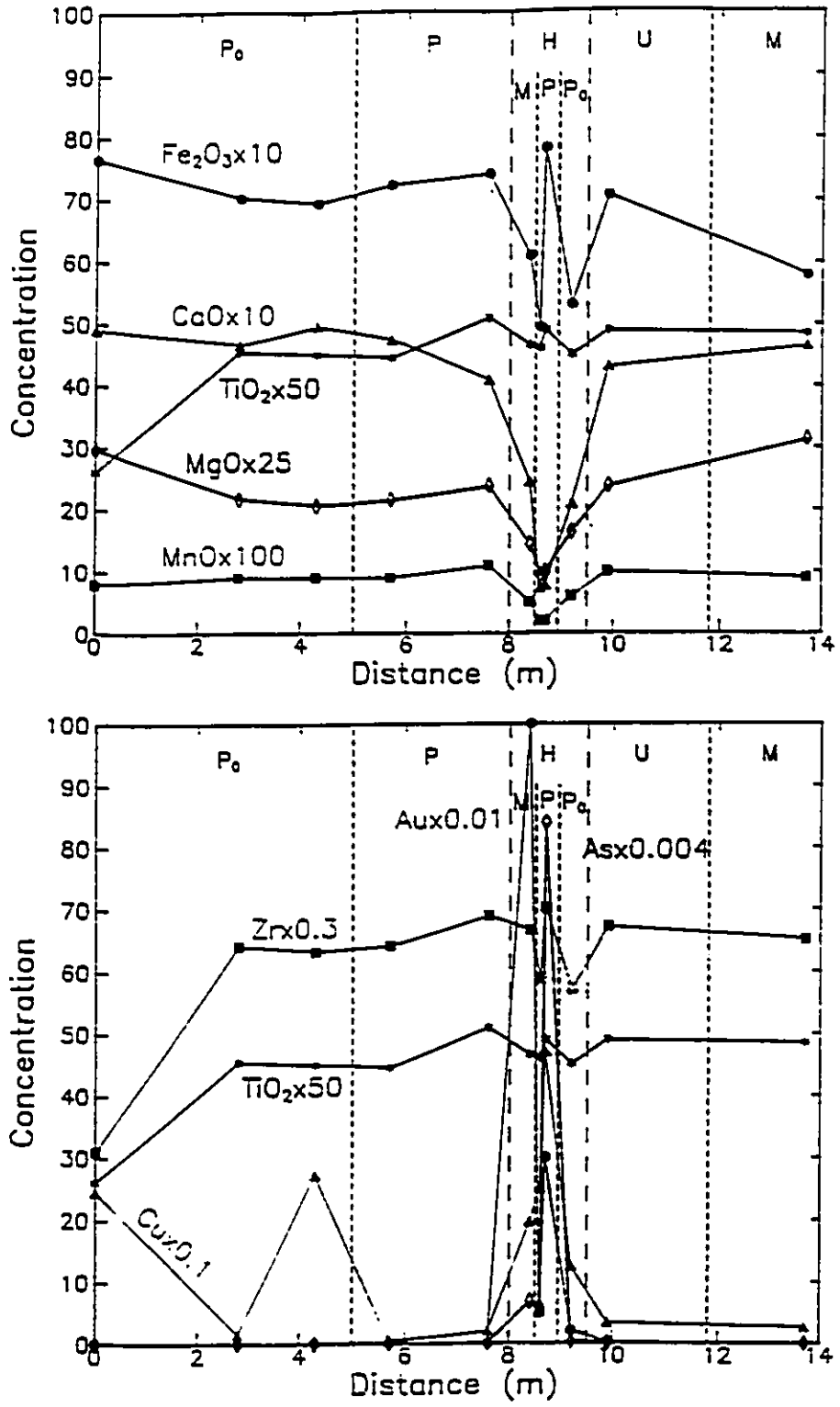

Fig.24. Plot of scaled concentrations of selected major and trace elements versus distance across the Grace Darwin shear zone. Divisions and labels as in Fig.23.

gold, as well as SiO_2 and K_2O.

Figure 25 is a Grant-type diagram (Grant, 1986) for the Grace Darwin shear zone. Plotted are the average concentrations of the major oxides and trace elements in the unaltered protomylonites versus the average concentrations in the protolith. A line of slope one is drawn which represents constant concentration under isovolumetric conditions. A second isocon of slope 1.25 is drawn based on the relative enrichments of Ti, P, Sc, V, Nb, and Zr, which are assumed to be immobile. Pb and LOI also behave as immobile components and lie along this line. Loss on ignition may represent the amount of water added to the system in order to drive the reaction (2) to form muscovite and epidote from feldspar. This isocon represents an average volume loss of 20% in the protomylonites. The components Ca, Fe, Si, Mg, Mn, Na, Al, K, Sr, Cr, Rb, Y, Ba, Ni, Co, Cu and Au lie below this line in the field of depletion, implying that these components were mobile and were removed from the system. Enrichments of As and Be may be related to minor hydrothermal alteration associated with the intense metasomatism in the central hydrothermally altered zone.

Figure 26 illustrates the relative depletions and enrichments in the mylonite versus the average protolith. The isocon of slope 1.24 representing a volume loss of 19% in the mylonite is drawn based on the concentrations of Zr, Ti and P, which are assumed to be immobile. Mg, Na, LOi, Y, As and Nb lie close to this isocon and are assumed to be immobile in these rocks. Loss on ignition may represent the amount of stoichiometric water in the hydrous minerals. Depletions of Ca, Fe, Mn, Al, Si, Sr, Cr, Ba, Zn, Rb, V, Ni, Li, Cu, Co, Sc and Au are implied, and enrichments of Be and Pb.

Figure 27 is a plot of the major and trace element concentrations in the ultramylonite versus the average protolith from Grace Darwin. The isocon of slope 1.27 represents a volume loss of 21% in the ultramylonite and is based on the ratios of concentrations of Ti, P, and Zr. The components K, LOI, Ba, Rb, Sc and Au lie close to the isocon and may have been immobile in these rocks. Depletions of Ca, Fe, Si, Mg, Mn, Na, Al, Cr, Sr, Ni, Y, Co,

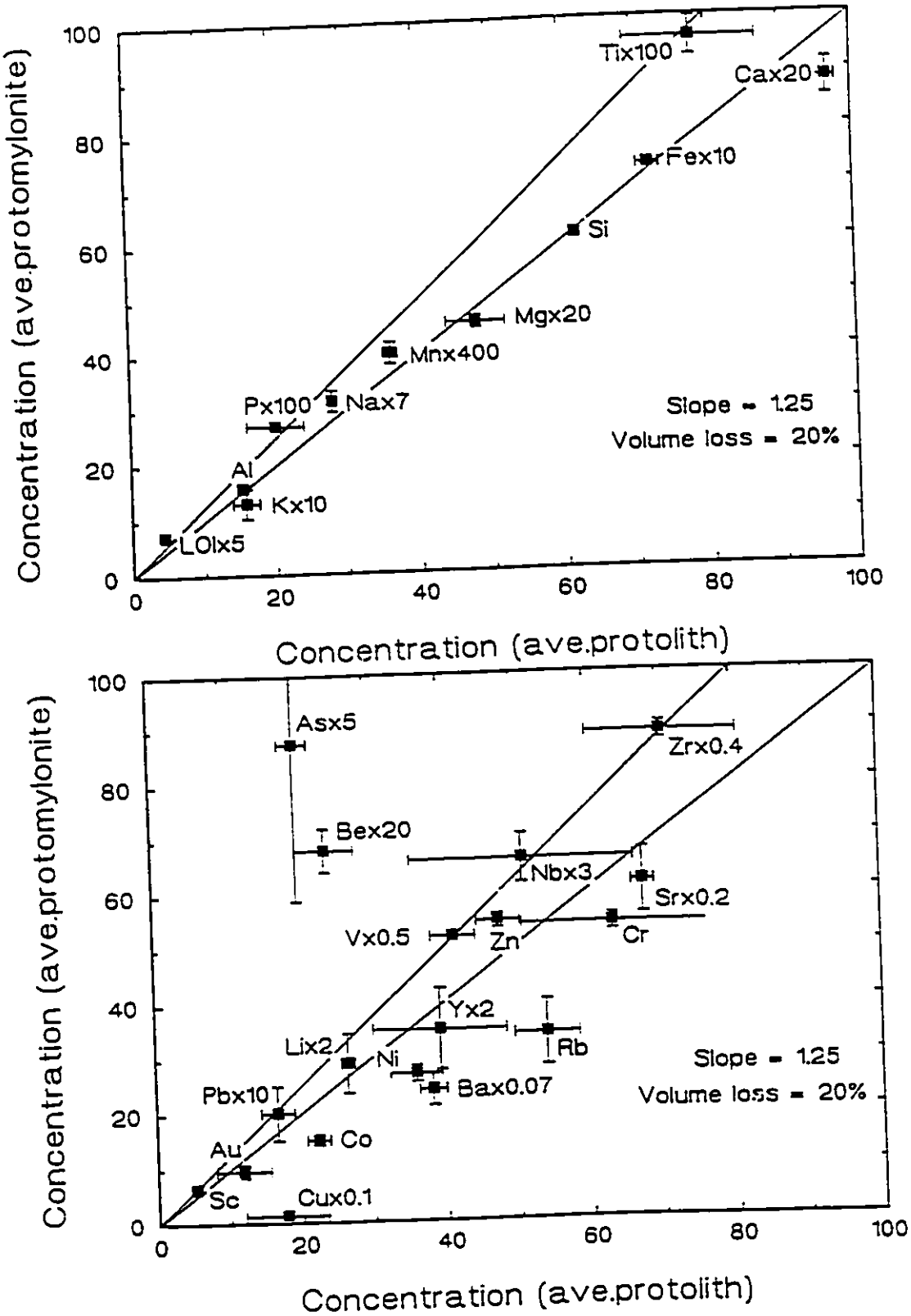

Fig.25. Plot of average concentrations of major and trace elements in Grace Darwin protomylonite versus average concentrations in the protolith. Error bars represent one standard deviation. An isocon line of slope 1.25 through elements assumed to be immobile represents an average volume loss of 20% in the mylonites.

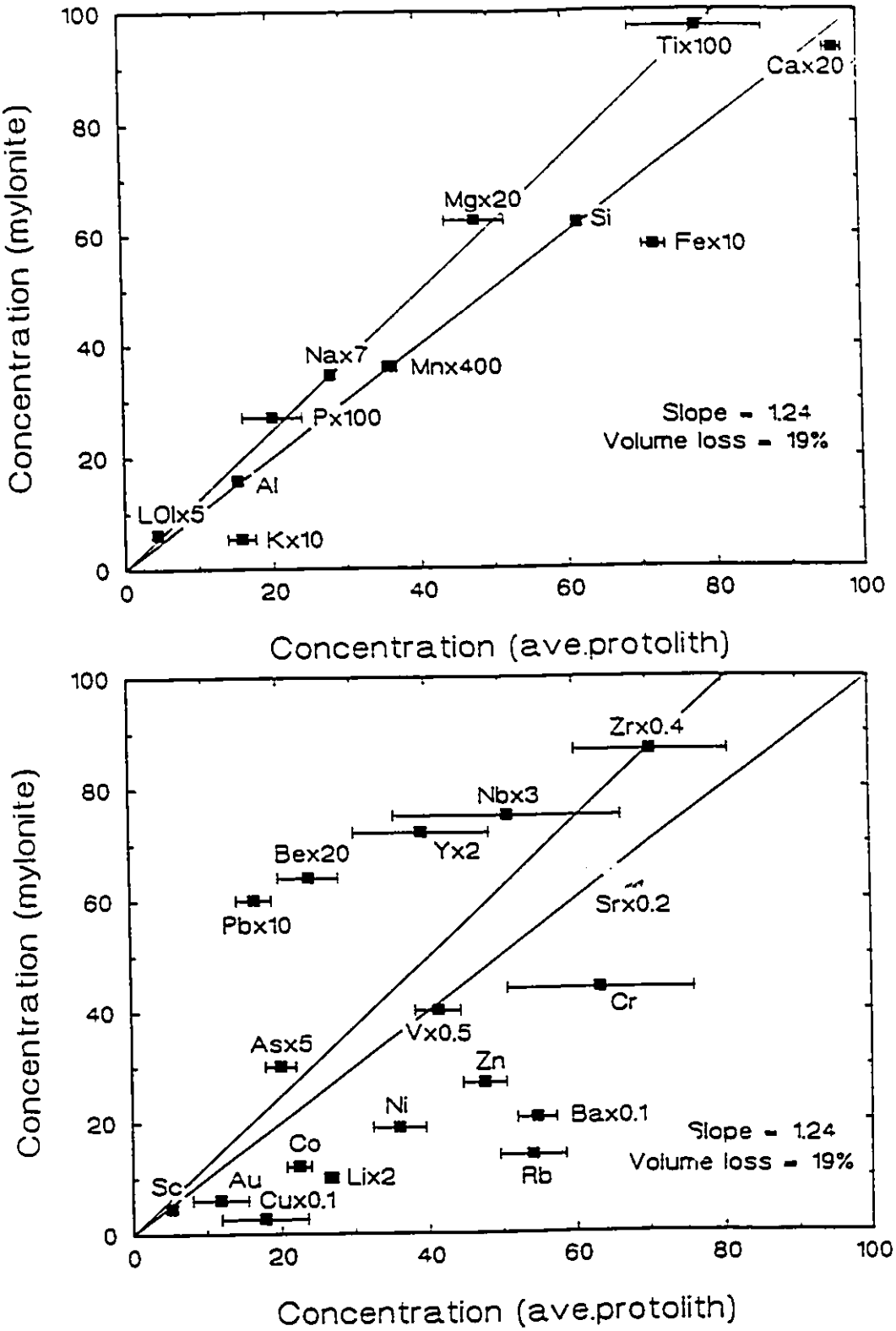

Fig.26. Plot of concentrations of major and trace elements in Grace Darwin mylonite versus average concentrations in the protolith. Error bars represent one standard deviation. An isocon line of slope 1.24 through elements assumed to be immobile represents an average volume loss of 19% in the mylonites.

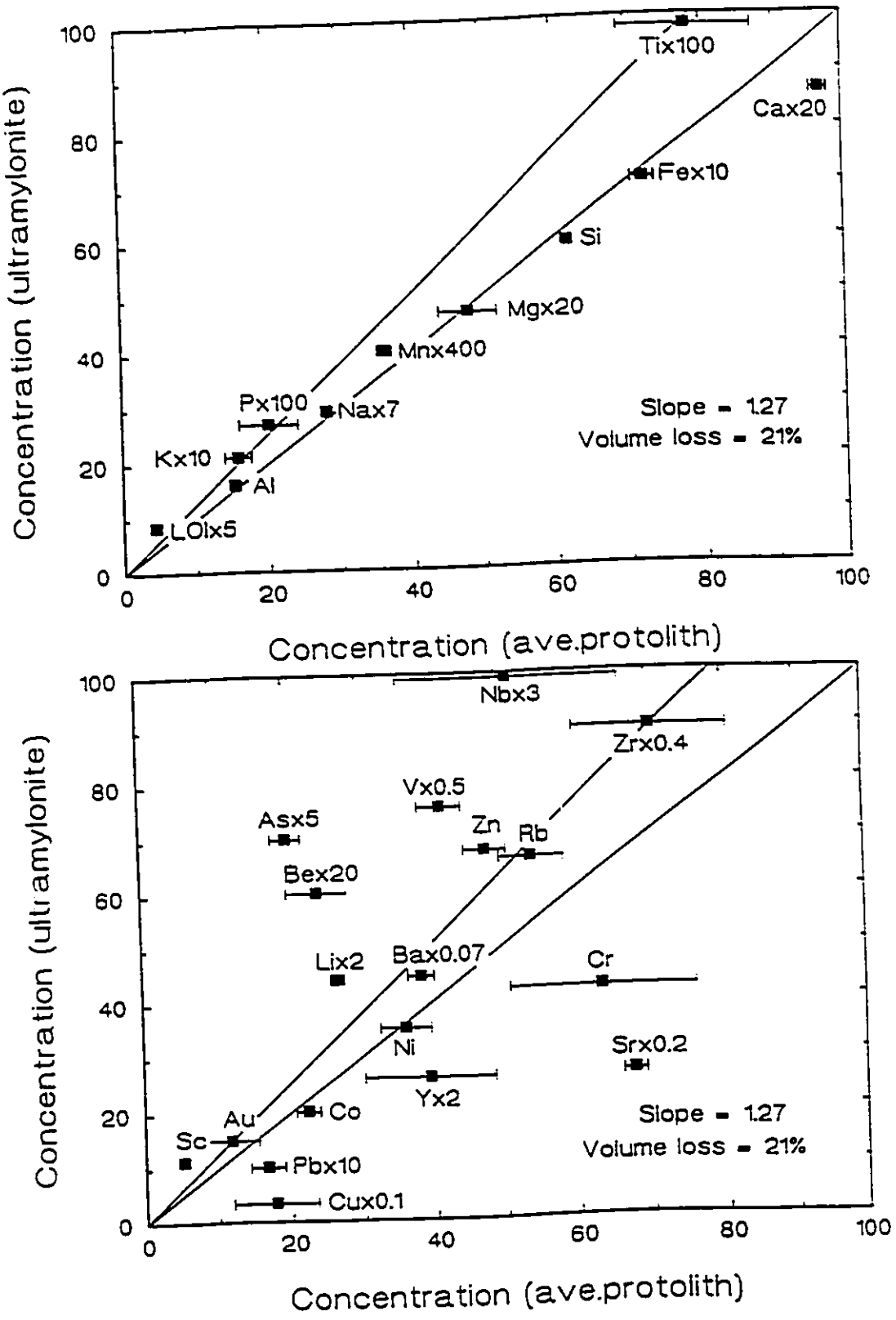

Fig.27. Plot of concentrations of major and trace elements in Grace Darwin ultramylonite versus average concentrations in the protolith. Error bars represent one standard deviation. An isocon line of slope 1.27 through elements assumed to be immobile represents an average volume loss of 21% in the mylonites.

Pb and Cu are implied, along with enrichments in the concentrations of Nb, V, Zn, As, Be, Li, and LOI in the ultramylonite.

Jubilee

Figures 28-30 illustrate the chemical variations that occur in selected major and trace elements across the Jubilee shear zone. The samples selected include two protolith samples, a protomylonite, four mylonites, and an ultramylonite. Hydrothermal alteration does occur across the zone but is difficult to delineate because of the complex chemical patterns. Multiple alteration events are likely to have occurred, resulting in very erratic chemical patterns.

Figure 28 represents the variations in the components SiO_2, Al_2O_3, CaO, Na_2O, K_2O, TiO_2, P_2O_5, Zr, Nb and Sc in rocks sampled from the Jubilee shear zone. SiO_2, Al_2O_3 and CaO show only minor variations across the zone. Na_2O becomes depleted in the central mylonites, and K_2O becomes enriched. TiO_2, P_2O_5 and Sc become progressively depleted with increasing degree of deformation. Zr and Nb patterns are erratic across the shear zone, but also show an overall general pattern of depletion.

Figure 29 is a plot of the concentrations of $Fe_2O_3^*$, MgO, V, Cr, Co, Sr, Rb, Ba, Li and Be in rocks associated with the Jubilee shear zone. Individual patterns are highly variable but generally there is a depletion in $Fe_2O_3^*$, Sr, V and Li within the sheared rocks. MgO, Ba, and Rb are generally enriched in the deformed rocks. Cr and Co have anomalously high values in JS-90-6 and Ba is anomalously high in JS-90-4.

Figure 30 shows the variation of Zn, Cu, Y, Ni and Au. There is a general enrichment of Ni within the shear zone and pronounced enrichment of Cu and Au in JS-90-5. Y becomes progressively depleted. Zn concentration is heterogeneous in the protolith and displays chemical patterns similar to V, showing a tendency to become depleted in the deformed rocks.

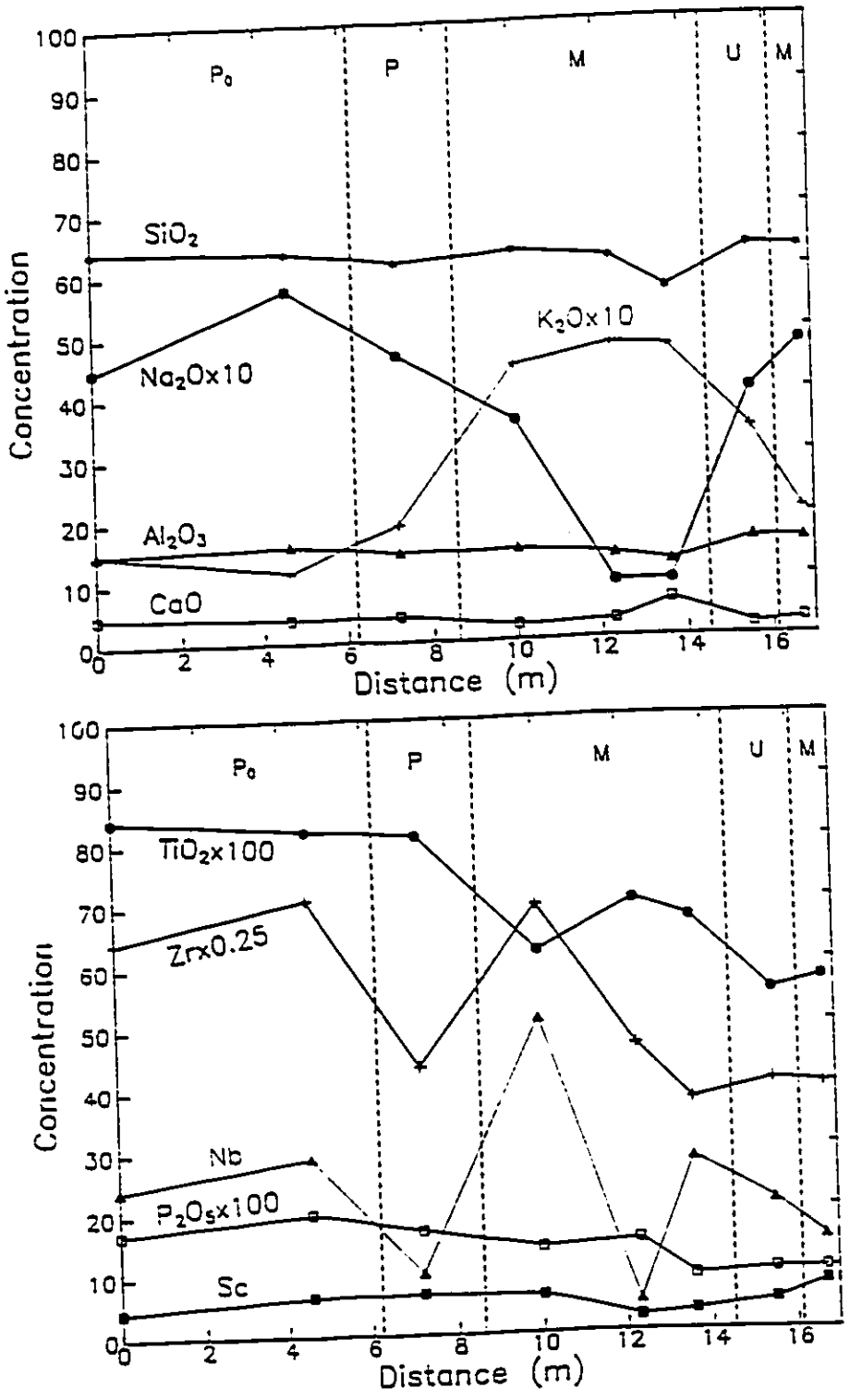

Fig.28. Plot of scaled concentrations of selected major and trace elements versus distance across the Jubilee shear zone. Divisions between rock types are based on feldspar grain sizes (P_o = protolith; P = protomylonite; M = mylonite; U = ultramylonite).

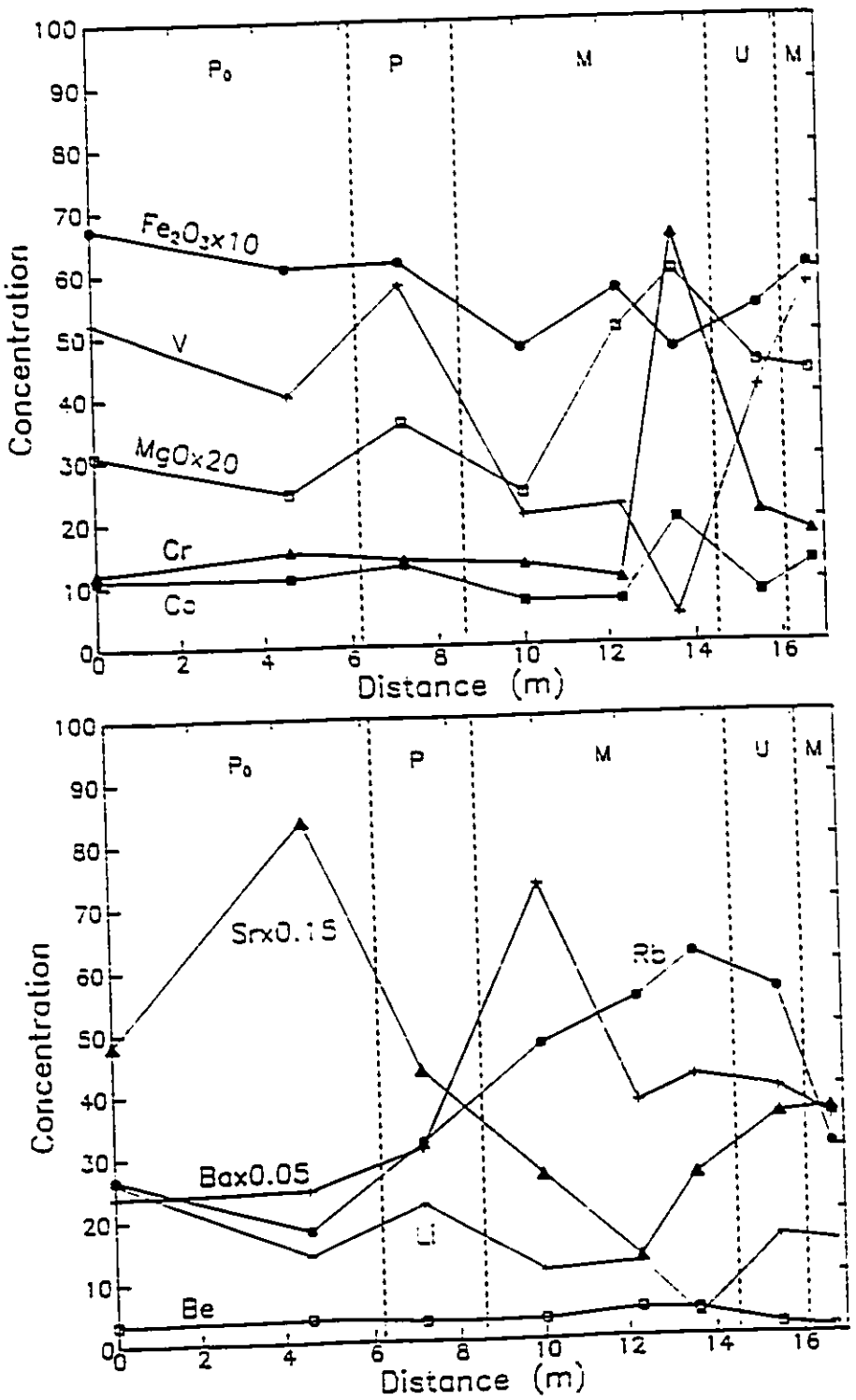

Fig.29. Plot of scaled concentrations of selected major and trace elements versus distance across the Jubilee shear zone. Divisions and labels as in Fig.28.

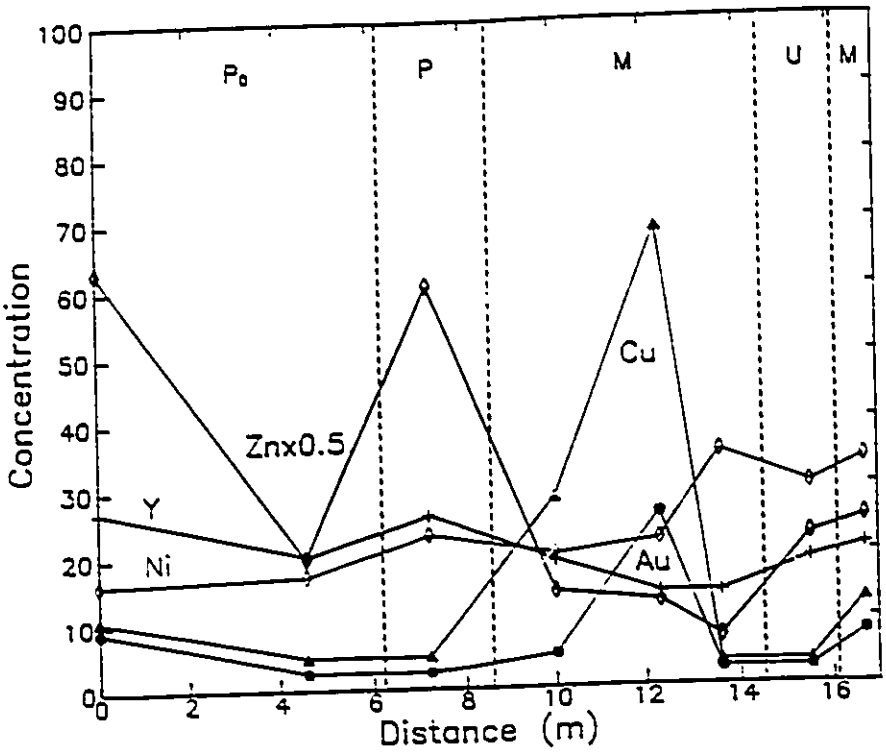

Fig.30. Plot of scaled concentrations of selected trace elements versus distance across the Jubilee shear zone. Divisions and labels as in Fig.28.

Figure 31 is a Grant-type isocon diagram for the Jubilee shear zone. The concentrations of major oxides and trace elements in the ultramylonite are plotted against the average concentrations in the protolith samples. The isocon of slope one representing constant mass under isovolumetric conditions is drawn. On this diagram there are depletions of many components in the ultramylonite relative to the protolith which are expected to be immobile, including Ti, P, Sc, Nb, and Zr. Also shown is the relative enrichment of K, Rb, Ba, Ni and Cr. These observations, in conjunction with observations from the previous diagrams imply that hydrothermal fluids have added and subtracted various components to and from the rocks. The complicated patterns of enrichments and depletions shown above in Figures 28-30 further attests to the complexity of the hydrothermal history of the rocks in the Jubilee shear zone. If we assume immobility of Ti, for example, the isocon diagrams indicate enrichments in Si, Fe, Na, Mn, K, Mg, Al, Rb, Ba, Cr, Sc, V, and Ni to the ultramylonites. Also, since a line through Ti and the origin would have a slope of less than one, the only alternative is to assume a gain in volume. However, the grain-size data indicates that feldspar dissolution was an active process in the Jubilee rocks.

Minto A

Figure 32 illustrates the chemical variations in SiO_2, Al_2O_3, K_2O, Na_2O, CaO, TiO_2, P_2O_5, Zr, Sc, and Nb that occur across the Minto A shear zone. The sampling traverse intersected protoliths, a protomylonite and an ultramylonite. Many components show variability between the protolith samples, so it is difficult to access some of the patterns. In general, there is little variation in the concentrations of SiO_2, Al_2O_3, or CaO across the zone. A steady decrease in Sc and Na_2O is accompanied by a increase in K_2O. The refractory components TiO_2, P_2O_5 and Zr show variable concentrations in the protolith, have peak values in the protomylonite, and drop off sharply in the ultramylonite. Nb shows slight

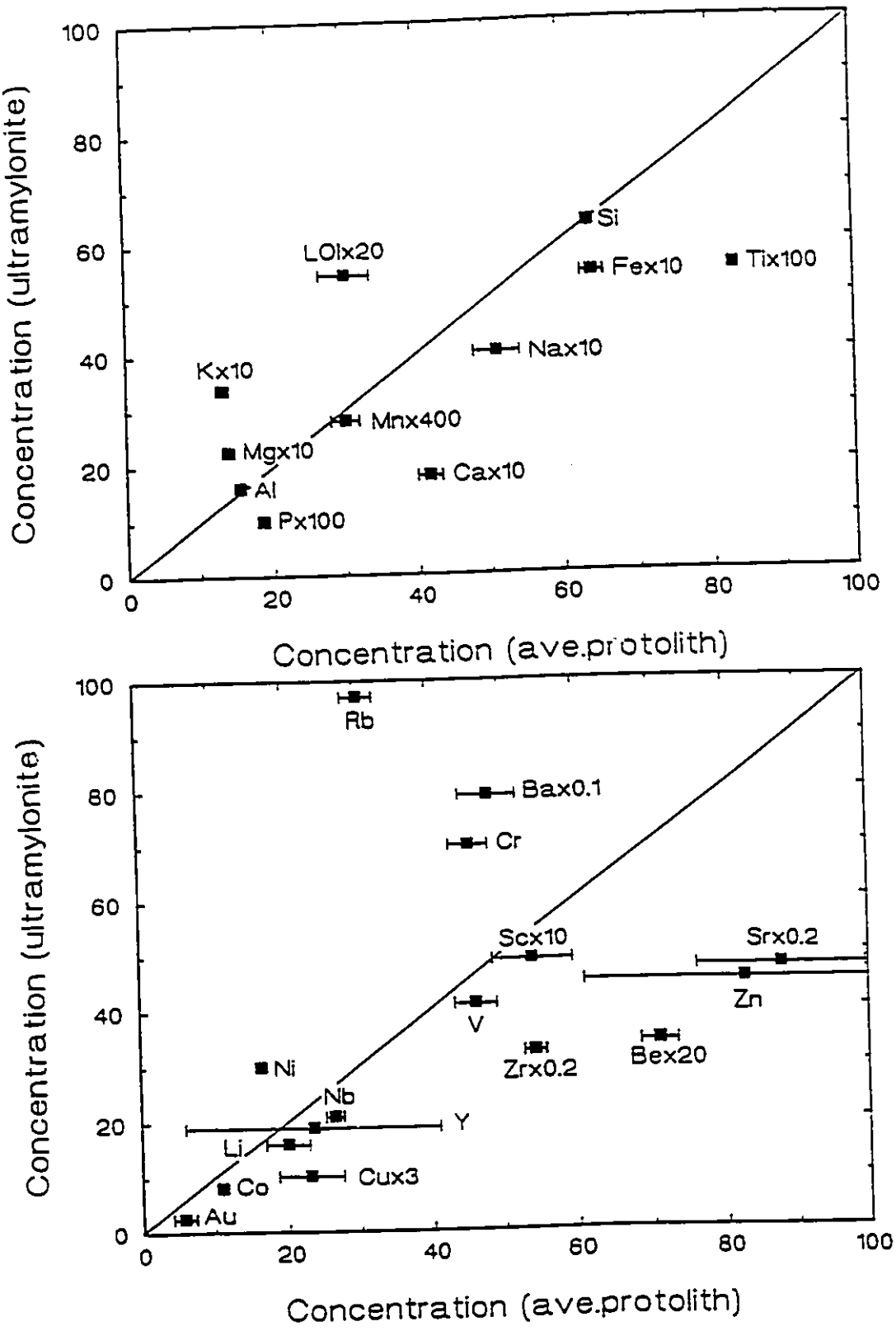

Fig.31. Plot of concentrations of major and trace elements in Jubilee ultramylonite versus average concentrations in the protolith. Error bars represent one standard deviation. K, Rb and Ba enrichment indicates substantial metasomatism.

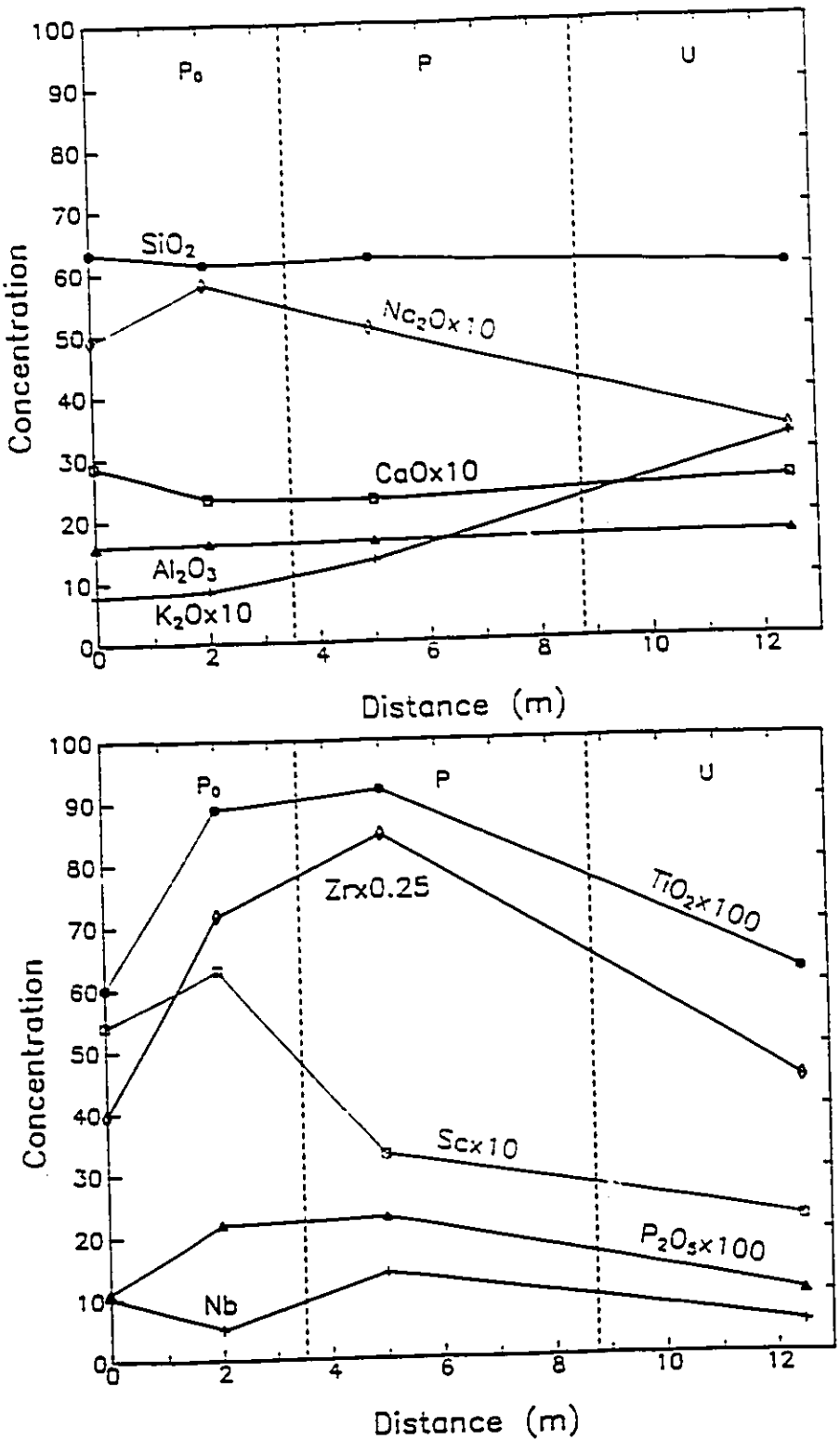

Fig.32. Plot of scaled concentrations of selected major and trace elements versus distance across the Minto A shear zone. Divisions between rock types are based on feldspar grain sizes (P_o = Protolith; P = protomylonite; U = ultramylonite).

variations across the zone.

Figure 33 plots the concentrations of $Fe_2O_3^*$, Cr, MgO, V, Co, Rb, Ba, Sr, Be and Li across the Minto A shear zone. Again, some components have variable concentrations in the protoliths and this original heterogeneity makes it difficult to interpret chemical variations reliably. In general, there appears to be a depletion of MgO and Li, and increases in Rb and Ba. Cr, and V are depleted in the protomylonite and their concentrations are slightly higher in the ultramylonite. Sr, Fe and Be have their highest concentrations in the protomylonite.

Figure 34 illustrates the variations across the Minto A shear zone of the elements Zn, Cu, Y, Ni and Au. Y and Au have higher concentrations in the protomylonite, Cu and Ni increase steadily and Zn shows slight depletion with increasing degree of deformation.

Figure 35 is a Grant-type diagram showing the ratios of major oxides and trace elements in the Minto A ultramylonite compared to the average protolith. Many of the HFSE lie below the isovolumetric line, implying volumetric gain in the ultramylonites. If Ti and Zr immobility was assumed, increases in Rb, Ba, Cu, Ni, K, Si, Ca, Al and LOI are implied, as well as decreases in Y, Sr, Sc, Be, Na, Mg and P. However, as in the Jubilee example, feldspar grain-size reduction does occur in the deformed rocks, and is very pronounced in the ultramylonites. Therefore, substantial changes in rock chemistry have taken place, above and beyond the simple addition of H_2O and reaction of feldspar to form muscovite. The anomalous enrichments of K, Rb and Ba support this assertion.

Minto C

Figure 36 illustrates the chemical variations in SiO_2, Al_2O_3, K_2O, Na_2O, CaO, TiO_2, P_2O_6, Zr, Sc, and Nb that occur across the Minto C shear zone. Protoliths on both sides of the shear zone were sampled, as well as a protomylonite, mylonites, and an ultramylonite. Some heterogeneities in protolith chemistry are observed. General trends in chemical

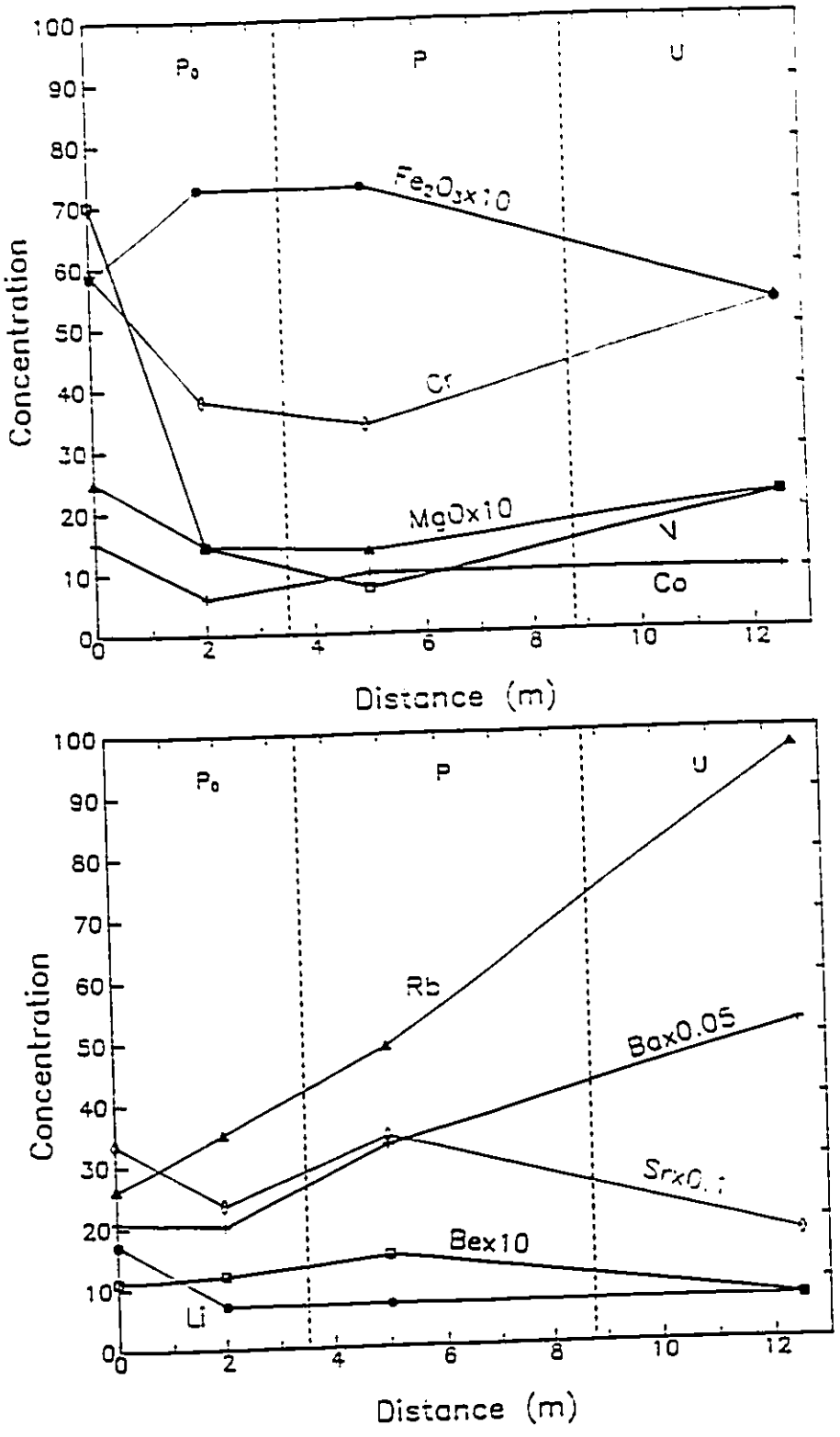

Fig.33. Plot of concentrations of selected major and trace elements versus distance across the Minto A shear zone. Divisions and labels as in Fig.32.

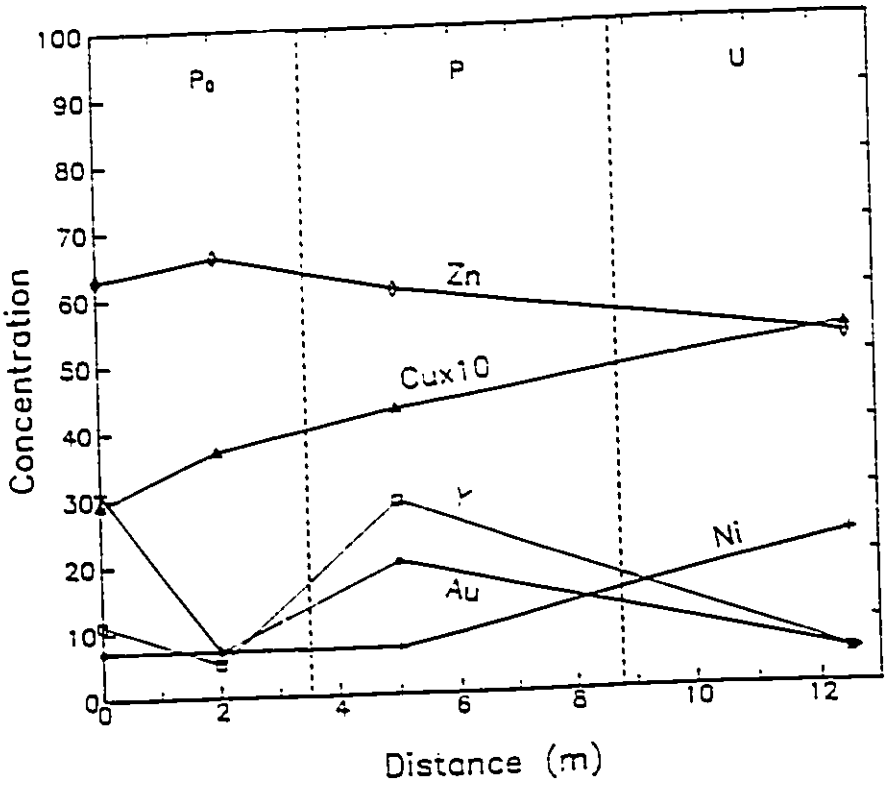

Fig.34.Plot of scaled concentrations of selected trace elements versus distance across the Minto A shear zone. Divisions and labels as in Fig.32.

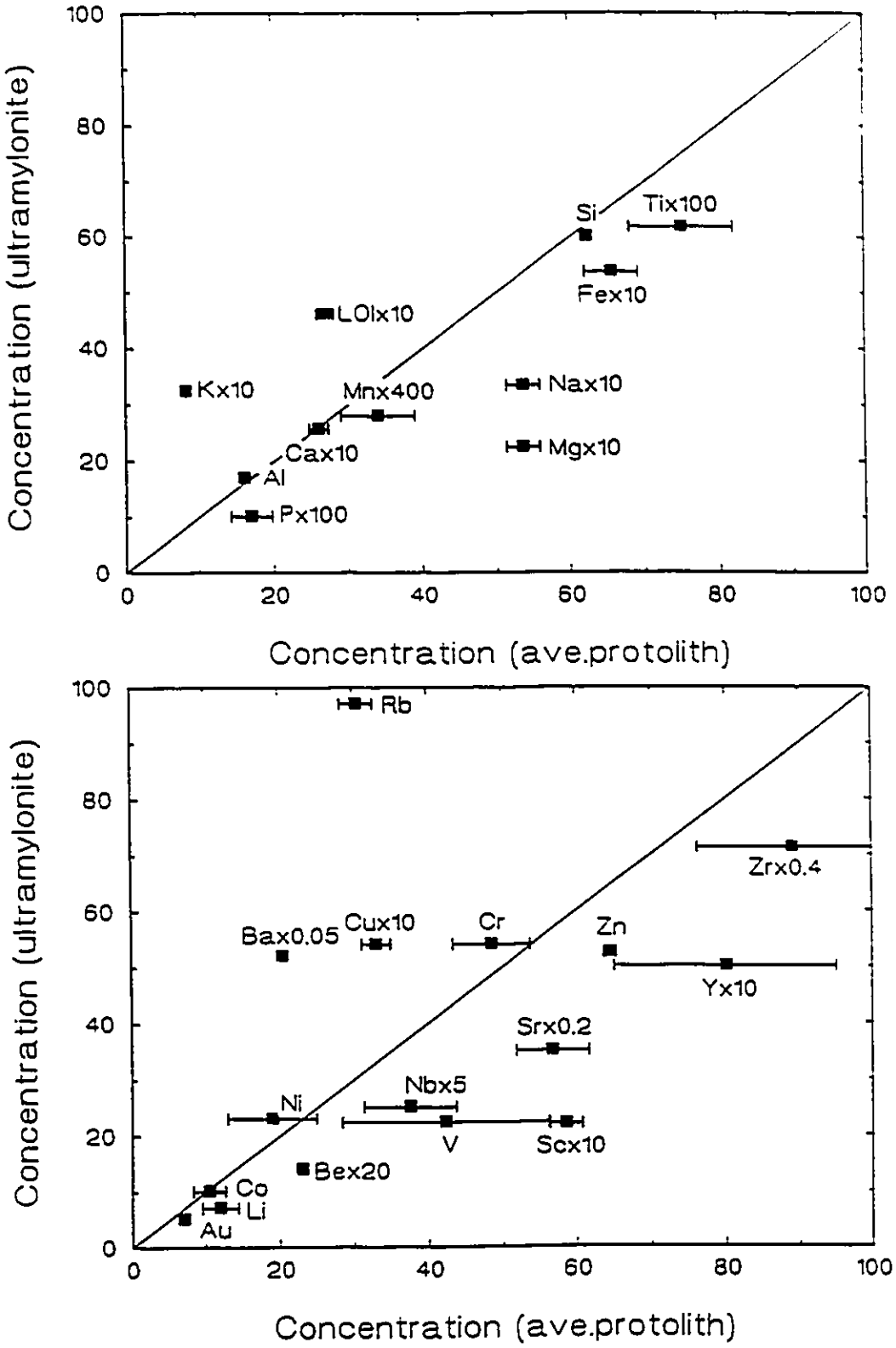

Fig.35. Plot of concentrations of major and trace elements in Minto A ultramylonite versus average concentrations in the protolith. Error bars represent one standard deviation. K, Rb and Ba enrichment indicates substantial metasomatism.

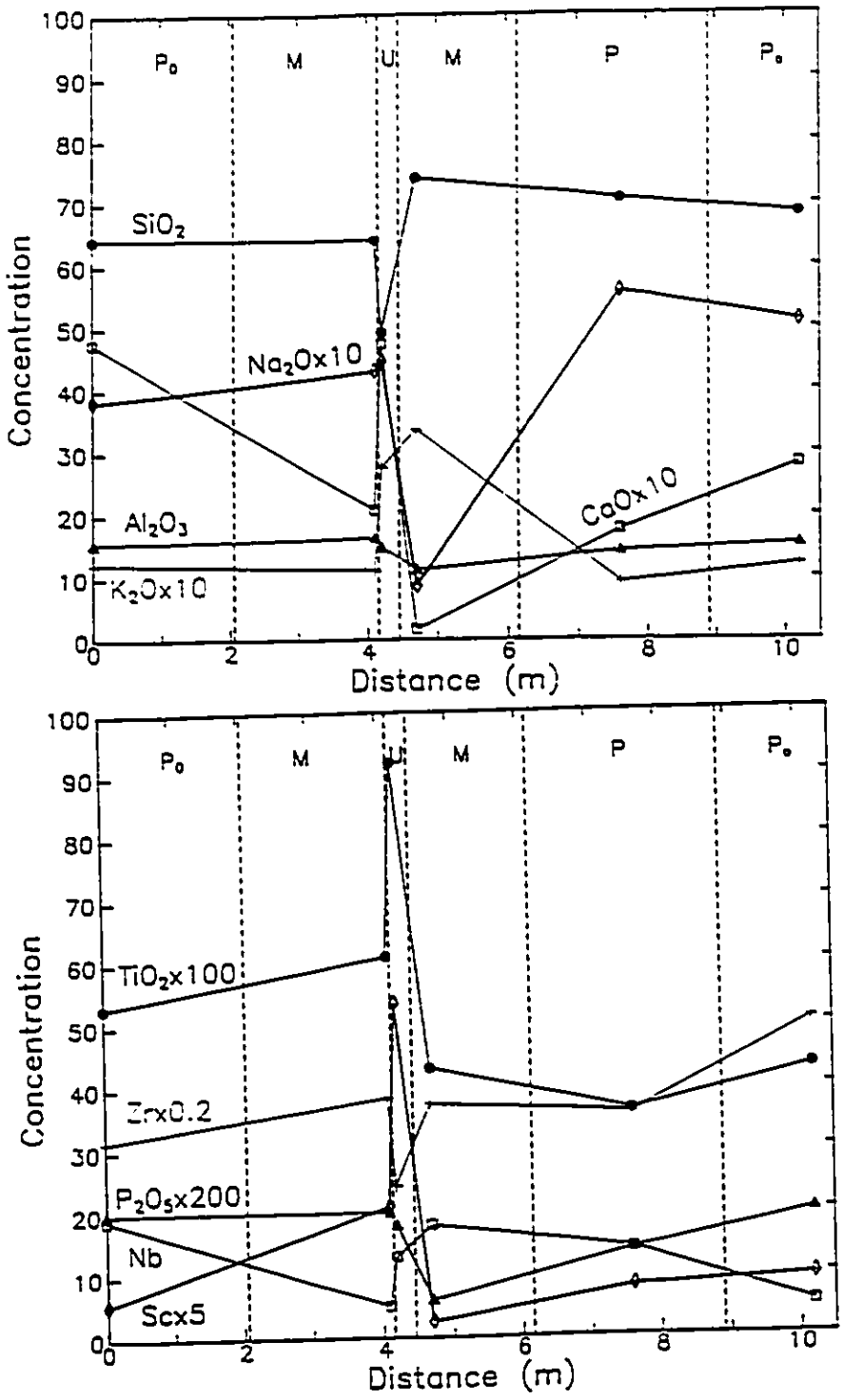

Fig.36. Plot of concentrations of selected major and trace elements versus distance across the Minto C shear zone. Divisions between rock types are based on feldspar grain sizes (P_o = protolith; P = protomylonite; M = mylonite; U = ultramylonite).

variation with degree of deformation include depletion of SiO_2, K_2O, CaO, Sc and Nb, and enrichment of Na_2O, Al_2O_3, TiO_2, Zr, and P_2O_5.

Figure 37 plots the concentrations of $Fe_2O_3^*$, MgO, V, Cr, Co, Sr, Rb, Ba, Li and Be in samples from the Minto C shear zone. $Fe_2O_3^*$, Cr, V, MgO, Co, Rb and Be show very similar patterns. All exhibit pronounced enrichments in the ultramylonite, and are generally depleted in the other sheared rocks. Ba is strongly enriched in MC-90-4 whereas Li and Sr are most depleted in this sample.

Figure 38 plots the concentrations of Zn, Cu, Y, As and Au in rocks associated with the Minto C shear zone. The most outstanding characteristic of the chemical trends shown on this diagram is the very high anomalous values of As, Cu and Au in MC-90-4. This is accompanied by a significant depletion in Zn and Y. Zn has anomalously high values in the adjacent ultramylonite, and has chemical patterns very similar to the immobile elements depicted on figure 37. Fluids which deposited As, Cu and Au were also rich in SiO_2, K and Rb, as can be seen from the previous diagrams. This metasomatism is most intense in sample MC-90-4, but may affect a wider area of the shear zone, which is implied by the asymmetry of chemical patterns for most components.

Figure 39 plots the ratios of concentrations of major elements oxides and trace elements in the ultramylonite versus the concentrations in the average protolith of the Minto C shear zone. The isocon line of slope 1.82 is drawn through the immobile components Ti, Fe, Mg, and Mn. This line represents a minimum volume loss of 45% in the ultramylonite. Depletions in Al, Si, Na, Ca, Sr, Rb, Ba and perhaps Y can be attributed to feldspar breakdown. Enrichments in components including Au, Ca, K, Cu, As, Ni, Sc, Be, and LOI indicate some additional metasomatism. The nature of these altering fluids is not readily apparent from the chemical patterns.

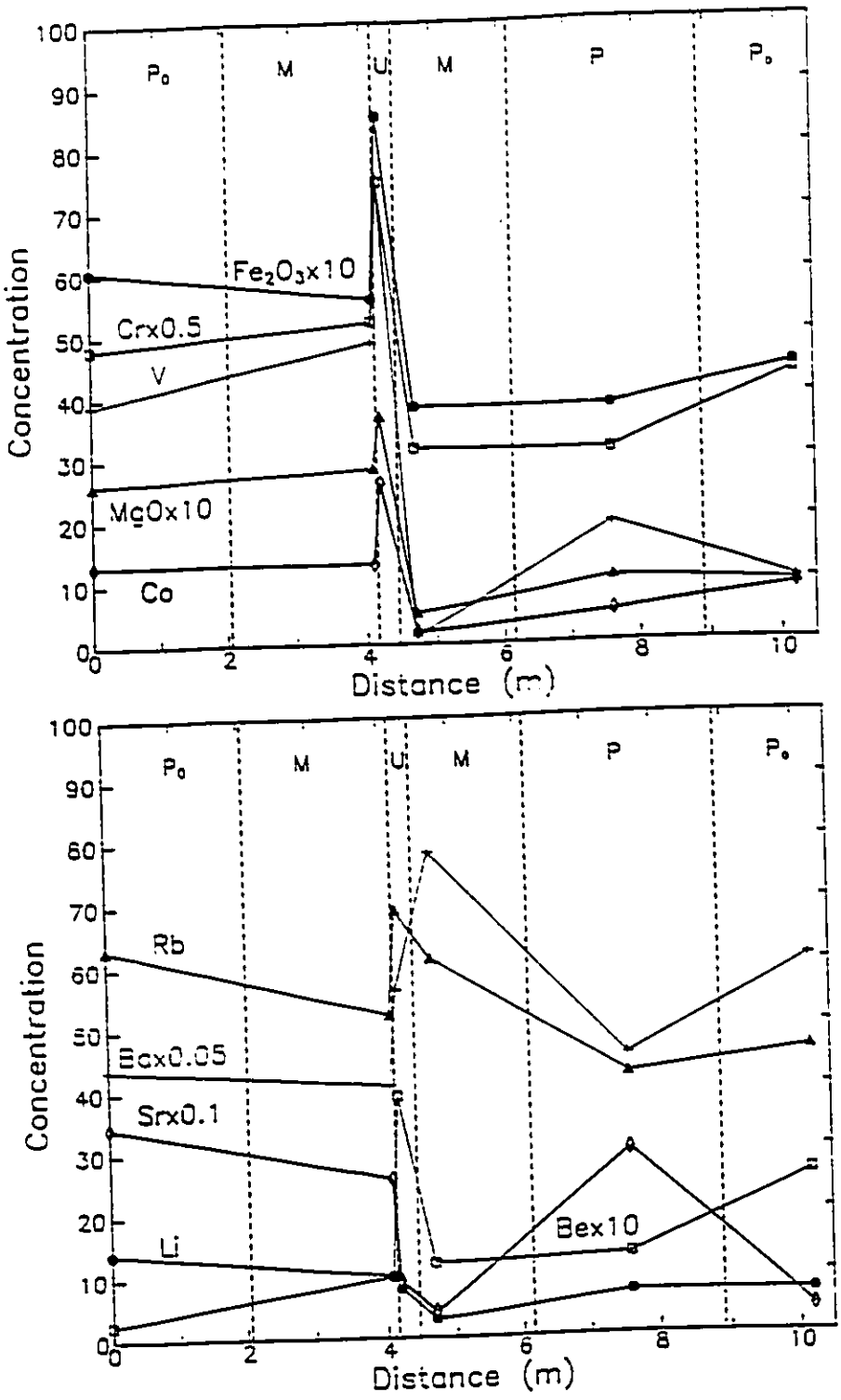

Fig.37. Plot of scaled concentrations of selected major and trace elements versus distance across the Minto C shear zone. Divisions and labels as in Fig.36.

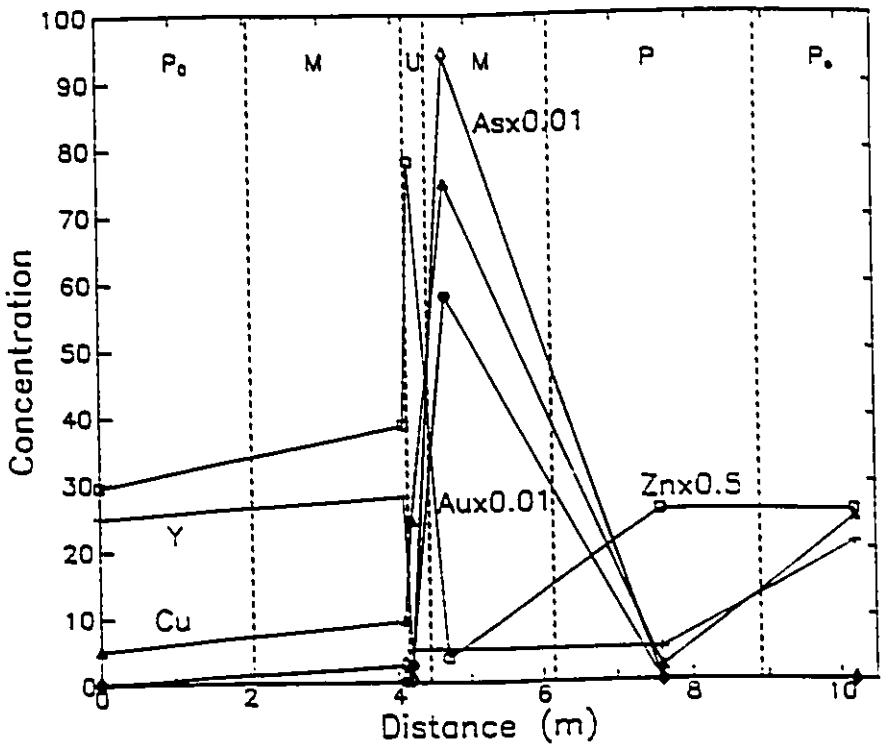

Fig.38. Plot of scaled concentrations of selected trace elements versus distance across the Minto C shear zone. Divisions and labels as in Fig.36.

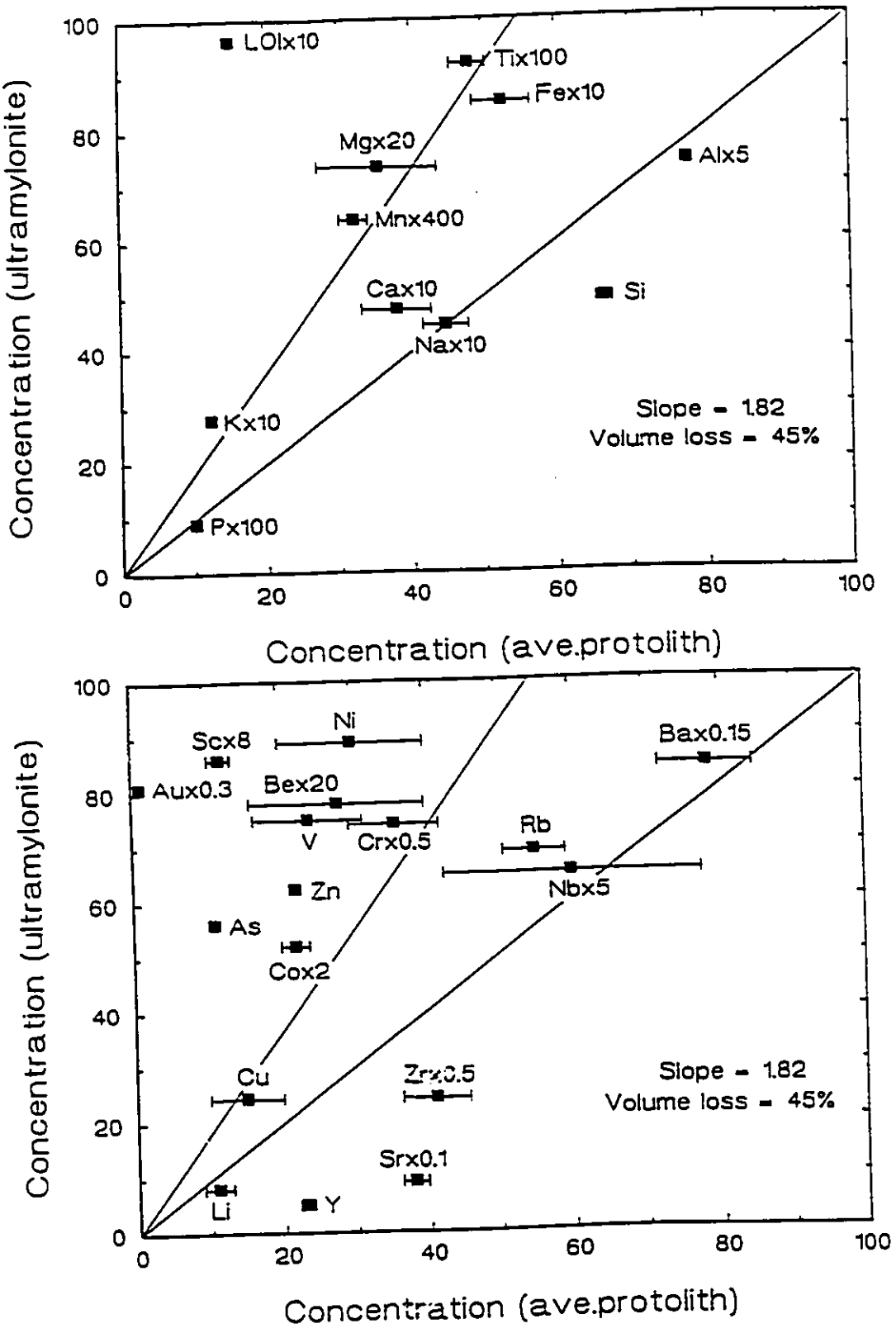

Fig.39. Plot of concentrations of major and trace elements in Minto C ultramylonite versus average concentrations in the protolith. Error bars represent one standard deviation. An isocon line of slope 1.82 through elements assumed to be immobile represents an average volume loss of 45% in the mylonites.

Minto E

Only protomylonites and a single mylonite are included in the suite of rocks associated with the Minto E shear zone. ME-90-5, labelled H, is the site of significant hydrothermal alteration. This alteration is characterized by increases in SiO_2, K_2O, Nb, Zr, and P_2O_5, as seen on figure 40. Chemical trends associated with mylonite development include depletion of CaO, K_2O, Nb, and P_2O_5, accompanied by enrichments of Na_2O, Al_2O_3, TiO_2, and Sc.

Figure 41 shows the variations in concentrations of $Fe_2O_3^*$, MgO, V, Cr, Co, Sr, Rb, Ba, Li and Be across the Minto E shear zone. Chemical changes in the rock in the alteration zone include substantial enrichments in Ba, Be, Sr and Rb, and depletions in Li, Co, Cr, MgO, V, and $Fe_2O_3^*$. Outside of this zone, depletions in Sr, Co, V, and $Fe_2O_3^*$ are accompanied by increases in the concentrations of Cr, and MgO in the mylonite.

Figure 42 plots the concentrations of Zn, Cu, Y, As and Au in rocks of the Minto E shear zone. Zn becomes progressively depleted with increasing degree of deformation and this depletion is accentuated in the altered protomylonite. The other components are depleted in the mylonite but have been added to the hydrothermally altered protomylonite.

The hydrothermal alteration has added Ba, Rb, Cu, Y, As, and Au to the protomylonitic rock ME-90-5.

Figure 43 is a Grant-type diagram showing the ratios of major oxides and trace elements in the mylonite versus the average protolith. Assuming Ti immobility, there has been increases in the proportions of Na, Cr, Sc, Ni, Mg and Al in the deformed rocks. Depletions in Fe, Mn, Ca, LOI, K, Zn, V, Rb, Sr, Y, Li, Cu and Au have also occurred.

Parkhill East

Figure 44 is a plot of the chemical variations of SiO_2, Al_2O_3, K_2O, Na_2O, CaO, TiO_2, P_2O_5, Zr, Sc, and Nb from rock samples taken in a traverse across the Parkhill shear zone at

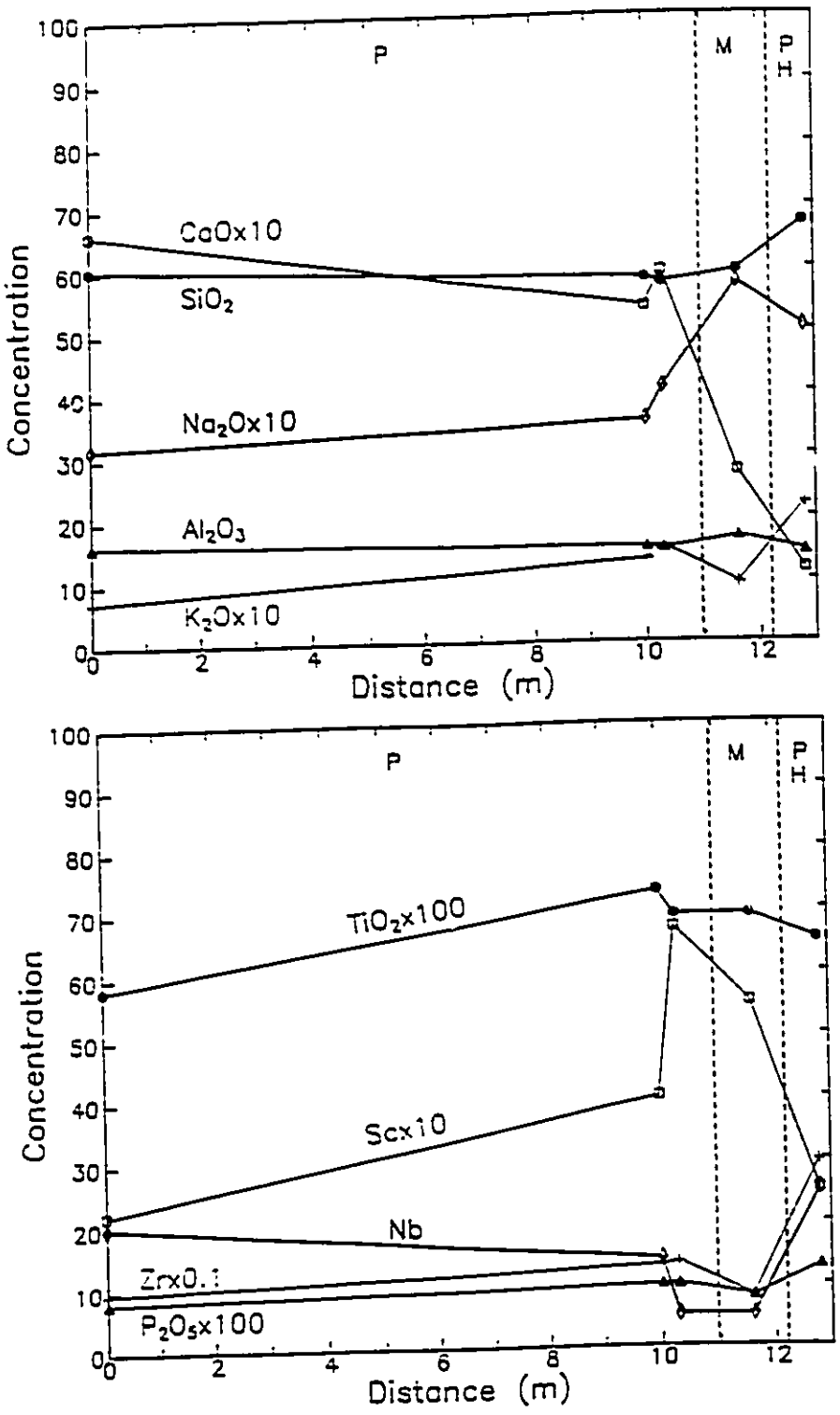

Fig.40. Plot of scaled concentrations of selected major and trace elements versus distance across the Minto E shear zone. Divisions between rock types are based on feldspar grain sizes (P=protomylonite; M=mylonite; H=zone of hydrothermal alteration).

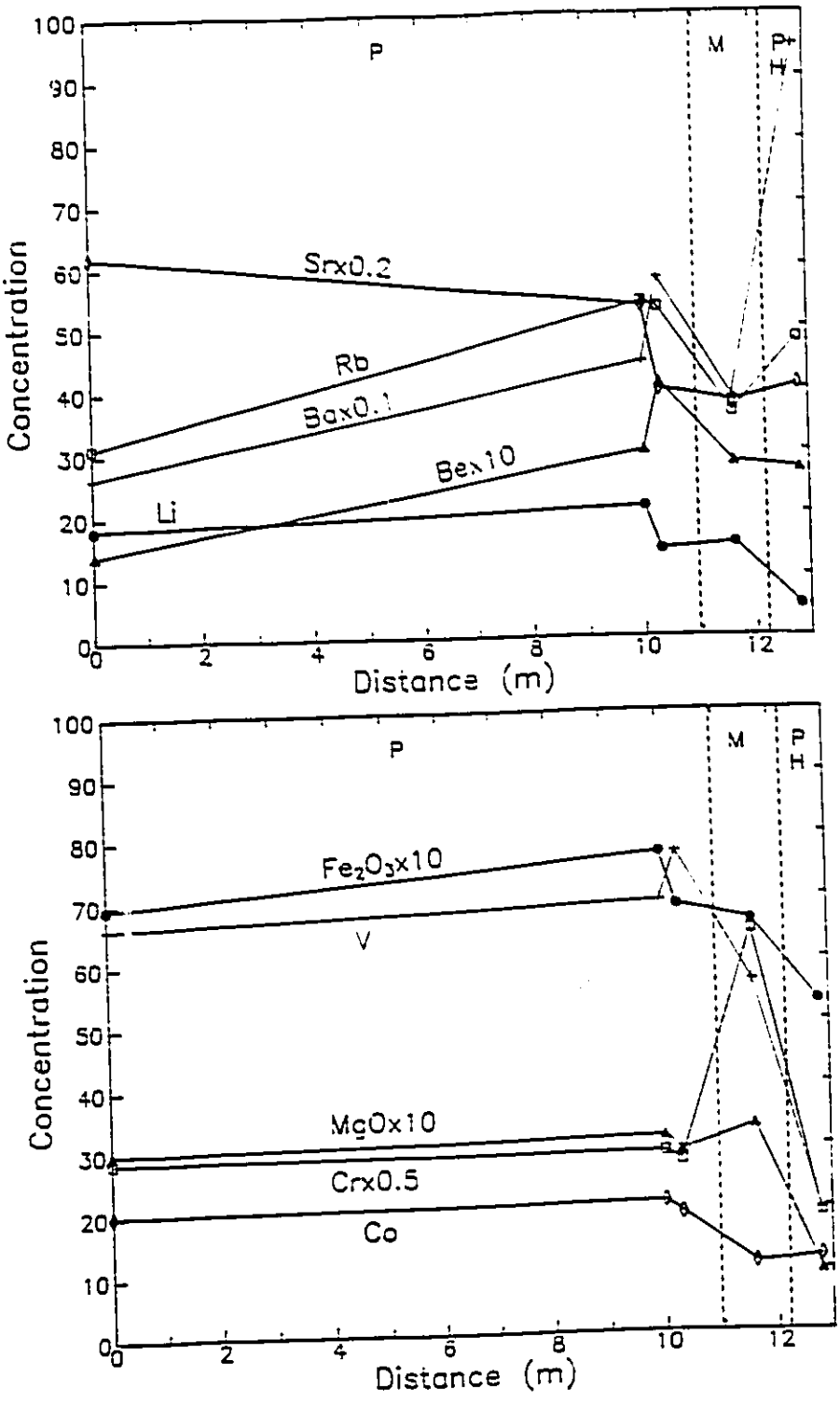

Fig.41. Plot of scaled concentrations of selected major and trace elements versus distance across the Minto E shear zone. Divisions and labels as in Fig.40.

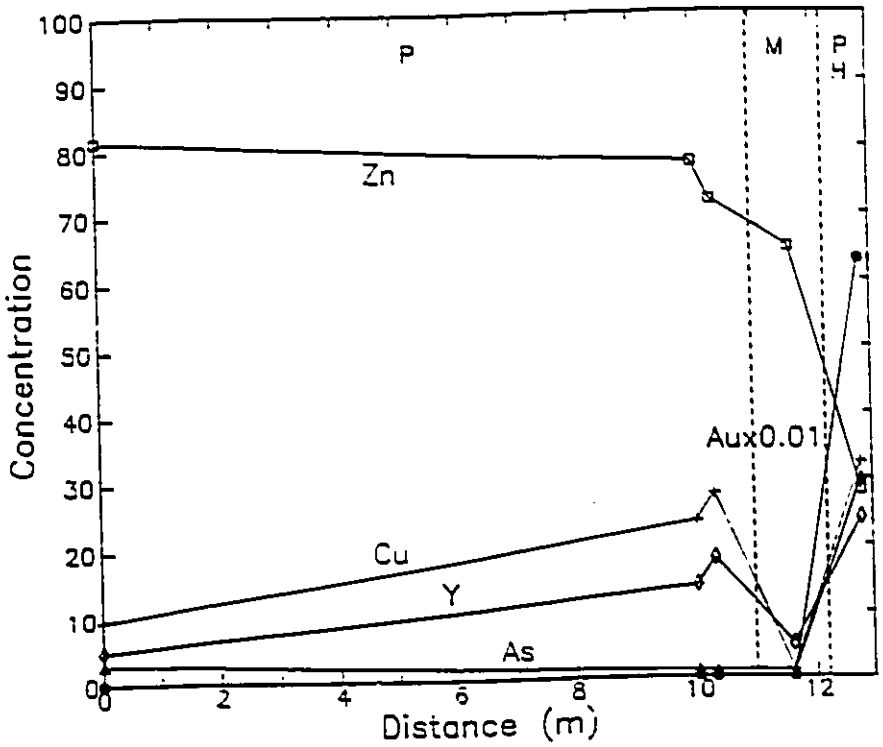

Fig.42. Plot of scaled concentrations of selected trace elements versus distance across the Minto E shear zone. Divisions and labels as in Fig.40.

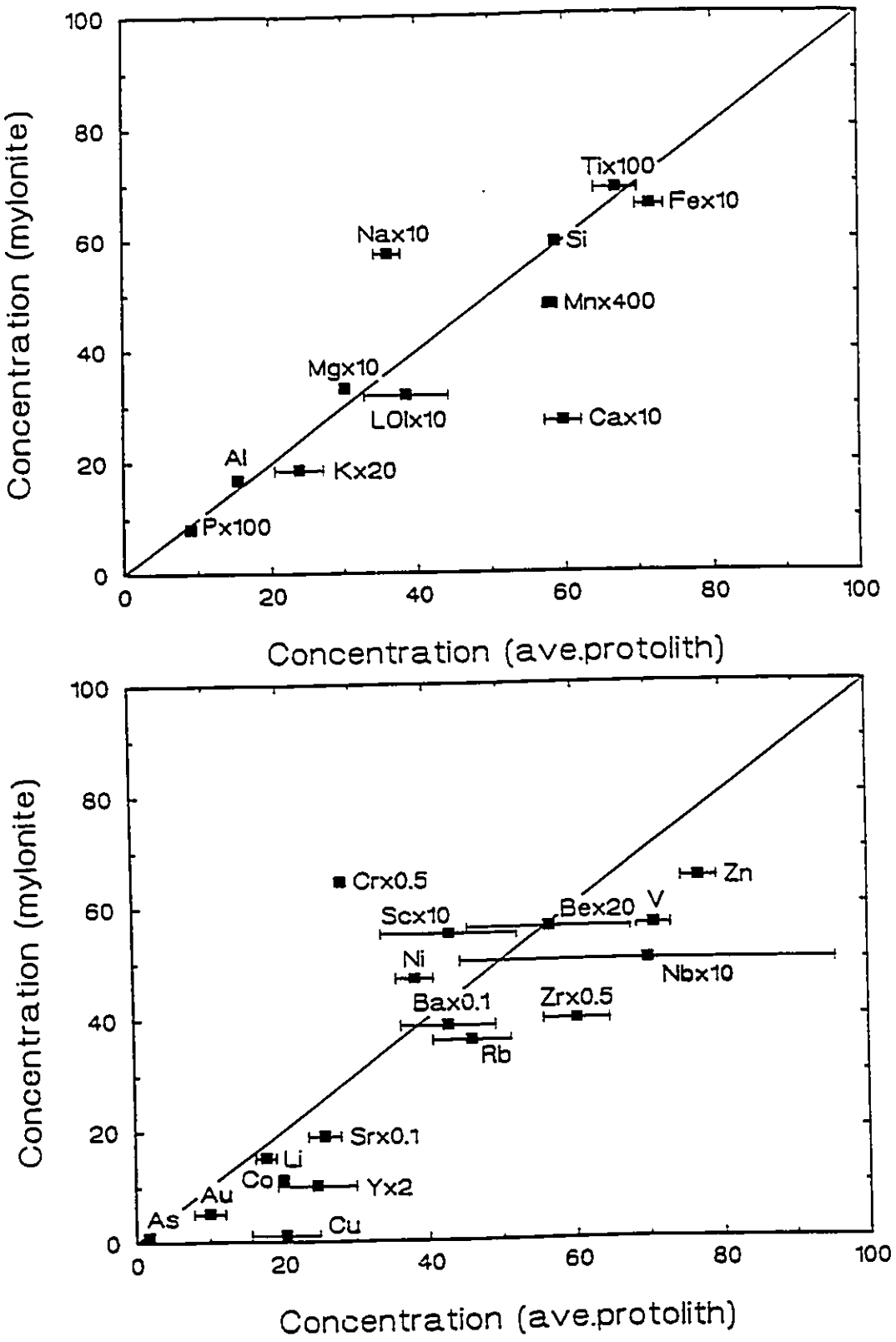

Fig.43. Plot of concentrations of major and trace elements in Minto E mylonite versus average concentrations in the protolith. Error bars represent one standard deviation.

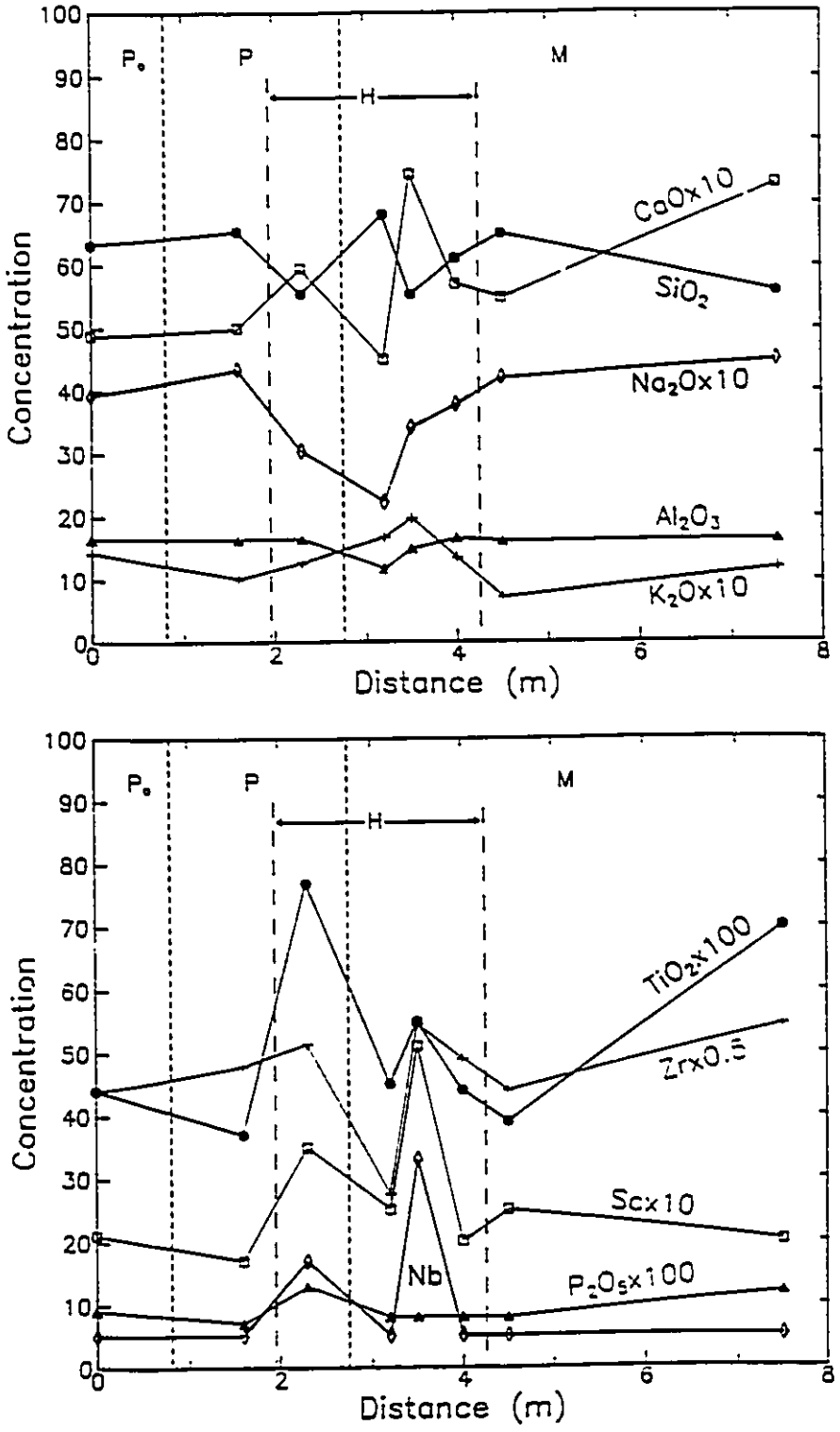

Fig.44. Plot of scaled concentrations of selected major and trace elements versus distance across the Parkhill East shear zone. Divisions between rock types are based on feldspar grain sizes (P_0 = protolith; P = protomylonite; M = mylonite; U = ultramylonite)

the east pit. The central zone labelled H contains a protomylonite and three mylonites and has undergone extensive metasomatic alteration; there is a depletion in Na_2O and Al_2O_3, variable changes in SiO_2 and CaO, and an enrichment of K_2O in this zone. The enrichment/depletion patterns of SiO_2 are mirrored by the patterns of the HFSE in the lower diagram.

Excluding the hydrothermal alteration zone H, there are increases in the concentrations of CaO, TiO_2, Na_2O, and Zr in rocks of increasing strain. Concomitant depletions of SiO_2, and K_2O are also observed.

Figure 45 illustrates the chemical variations in the components $Fe_2O_3^*$, MgO, V, Cr, Co, Sr, Rb, Ba, Li and Be across the shear zone. Increases in $Fe_2O_3^*$, MgO, Cr, Co, V, Rb, Li and Be in the zone of hydrothermal alteration suggest that these components were introduced into this zone. They also show relative enrichments in the most deformed mylonite.

Figure 46 shows the variations in the concentrations of Zn, Cu, As, Y and Au across the Parkhill East shear zone. Au, Zn, As and Y have all been added in the zone of hydrothermal alteration, whereas Cu is depleted.

Figure 47 is an isocon diagram for the major oxide and trace element concentrations in the average mylonite versus the protolith in rocks from the Parkhill East shear zone. An isocon of slope 1.27 representing an average volume loss of 21% in the mylonites is drawn through the components Ca, Ti, Mg, Mn and LOI. These components, as well as Co, and Ni behave as immobile elements in this system. Enrichments in Cu, Co, As, Be, and Y may be attributed to additions by hydrothermal fluid influxes, related to the metasomatism noted in the central zone of alteration. Depletions in Si, Fe, Na, K, Al, Zn, Ba, Zr, V, Rb, Sr, Sc, Li and Au suggest that these components were mobile and removed from the mylonites.

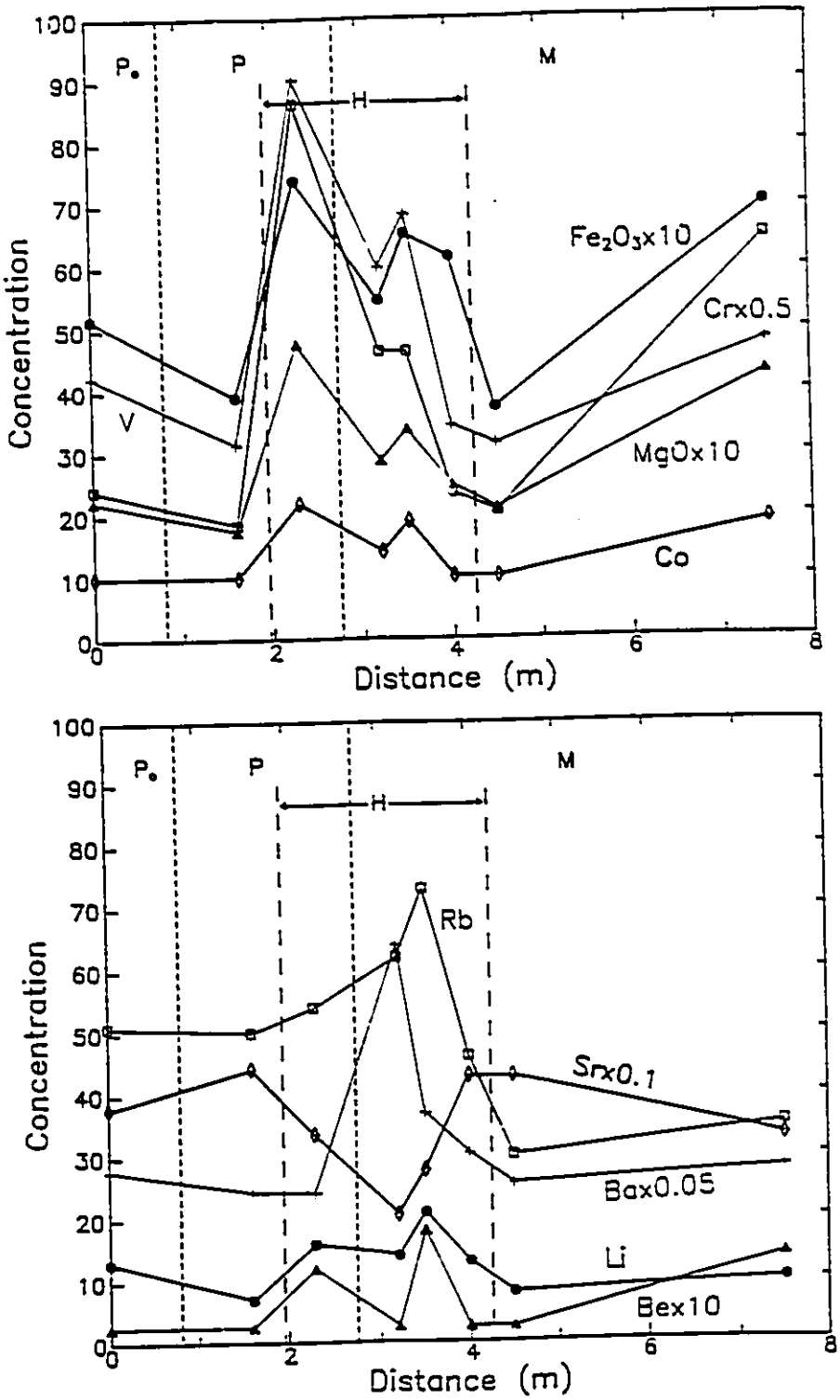

Fig.45. Plot of scaled concentrations of selected major and trace elements versus distance across the Parkhill East shear zone. Divisions and labels as in Fig.44.

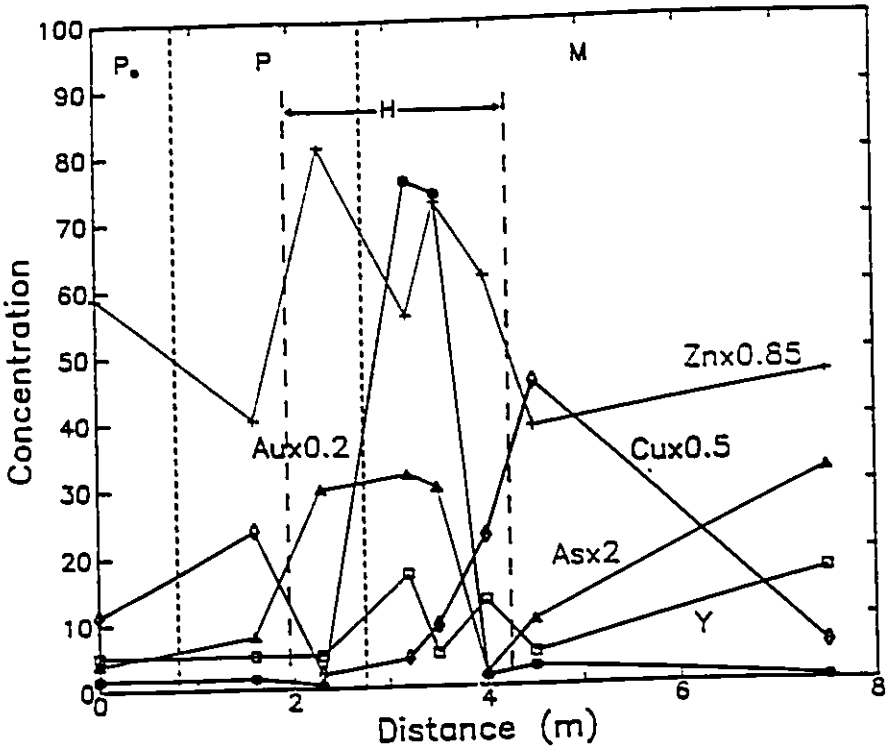

Fig.46. Plot of scaled concentrations of selected trace elements versus distance across the Parkhill East shear zone. Divisions and labels as in Fig.45.

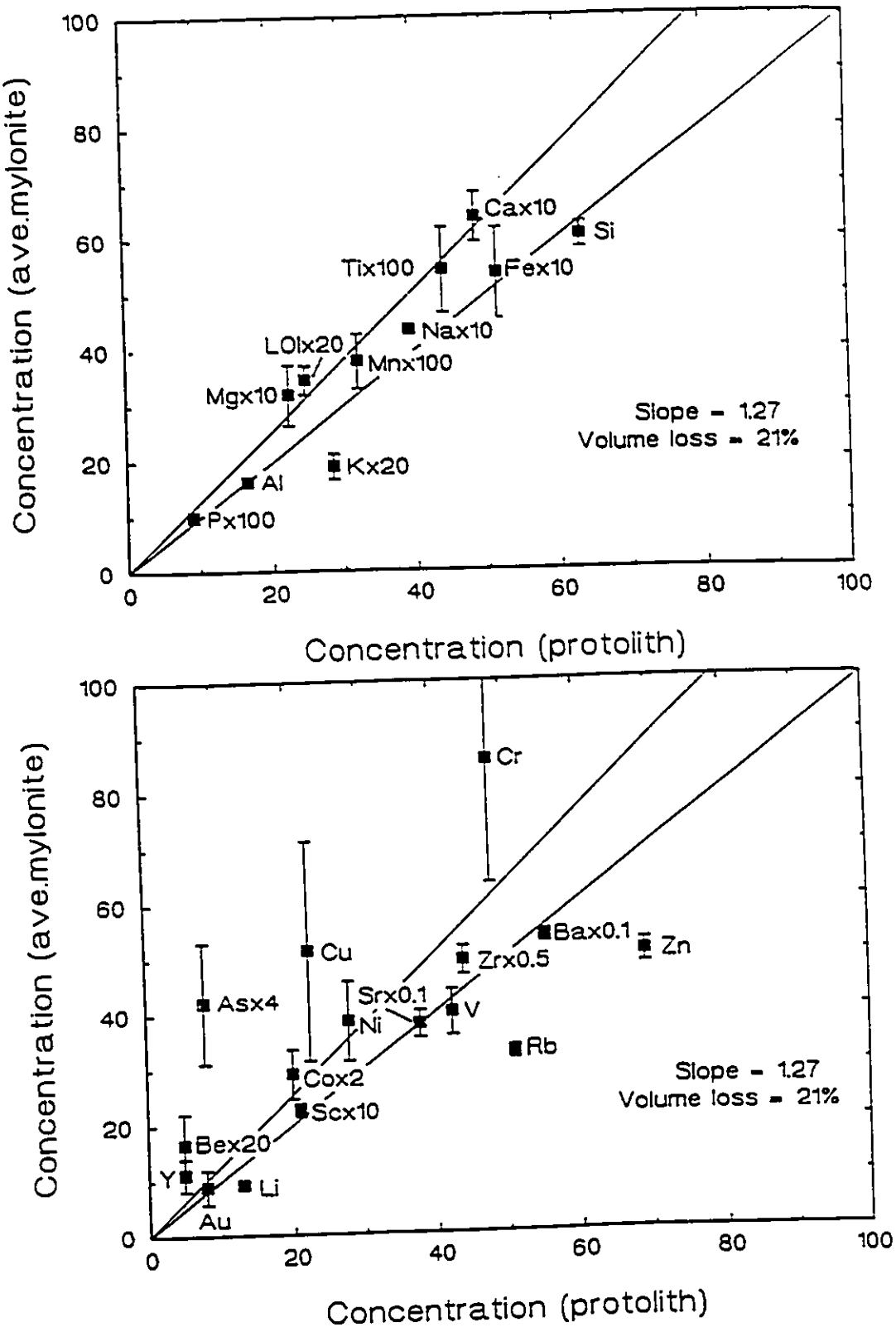

Fig.47. Plot of average concentrations of major and trace elements in Parkhill East mylonite versus concentrations in the protolith. Error bars represent one standard deviation. An isocon line of slope 1.27 through elements assumed to be immobile represents an average volume loss of 21% in the mylonites.

Parkhill West

Five samples were taken across the Parkhill shear zone at the west pit. The presence of an adjacent lamprophyre dike prohibited a full cross-sectional traverse. Hydrothermal alteration possibly related to the emplacement of this dike is reflected in the chemistry of samples PHW-90-3 through PHW-90-5. Figure 48 is a plot of the chemical variations in SiO_2, Al_2O_3, K_2O, Na_2O, CaO, TiO_2, P_2O_5, Zr, Sc, and Nb from the rocks. Enrichment in CaO, Na_2O, and TiO_2 and depletions in SiO_2, and K_2O characterize the hydrothermal alteration.

Figure 49 illustrates the chemical variations in the components $Fe_2O_3^*$, MgO, V, Cr, Co, Sr, Rb, Ba, Li and Be across the shear zone. Enrichments in $Fe_2O_3^*$, Cr, MgO, V, Co, Sr, and Be are accompanied by depletions in Rb and Li in the rocks in zone H.

Figure 50 shows the variations in the concentrations of Zn, Cu, As, Y and Au across the Parkhill West shear zone. Enrichments in these components are related to the hydrothermal alteration within zone H.

Figure 51 is a Grant-type diagram plotting the concentrations of the major element oxides and trace elements in the unaltered mylonite versus the protolith. The mylonite is relatively enriched in Ti, Fe, Ca, LOI, K, Mn, Mg, Rb, Ba, Y and Li compared to the protolith, and is relatively depleted in Si, Na, Zr, Sr, Sc, Cr, Co, Nb, V, Cu, Au and As.

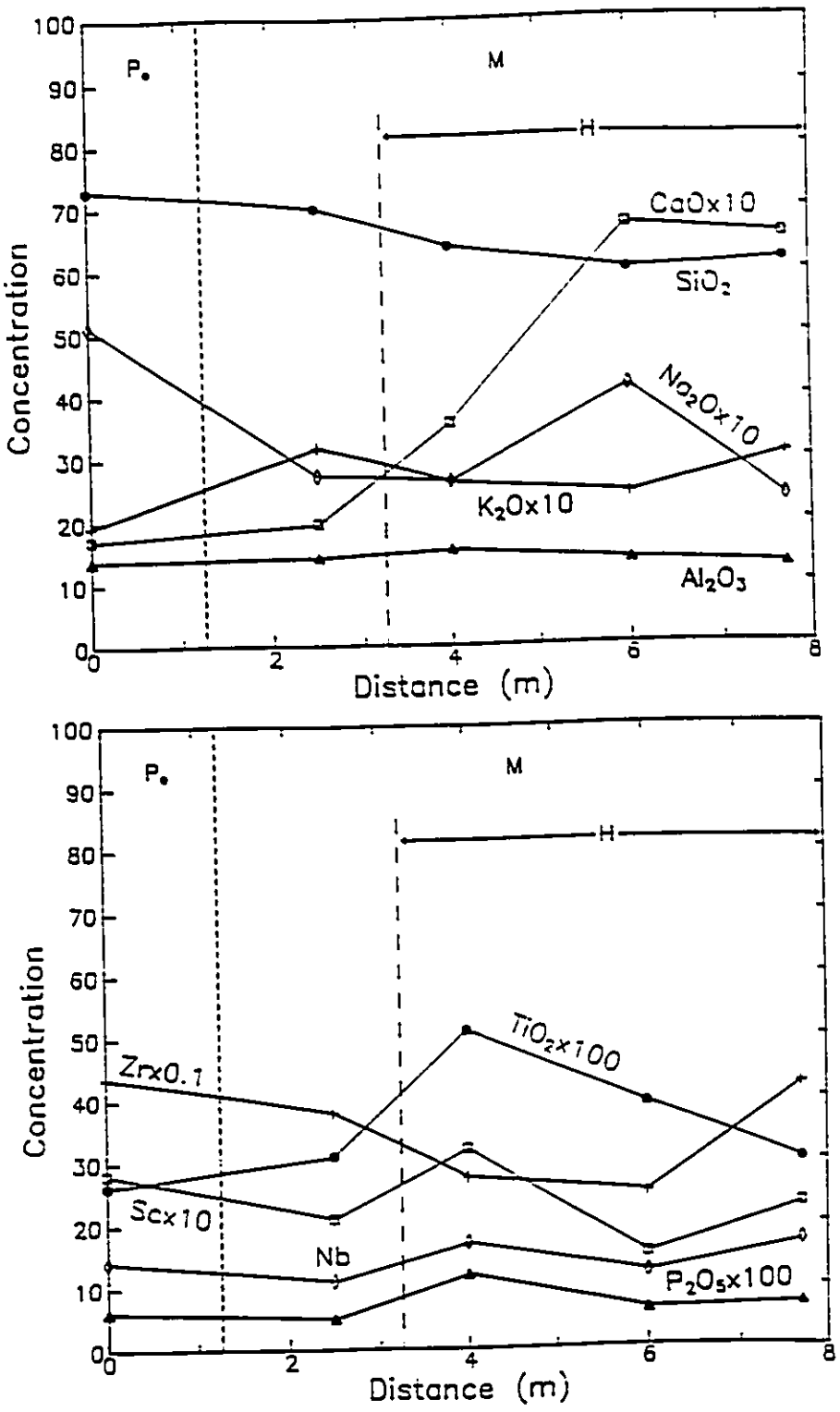

Fig.48. Plot of scaled concentrations of selected major and trace elements versus distance across the Parkhill West shear zone. Divisions between rock types are based on feldspar grain sizes (P_o = protomylonite; M = mylonite; H = zone of hydrothermal alteration).

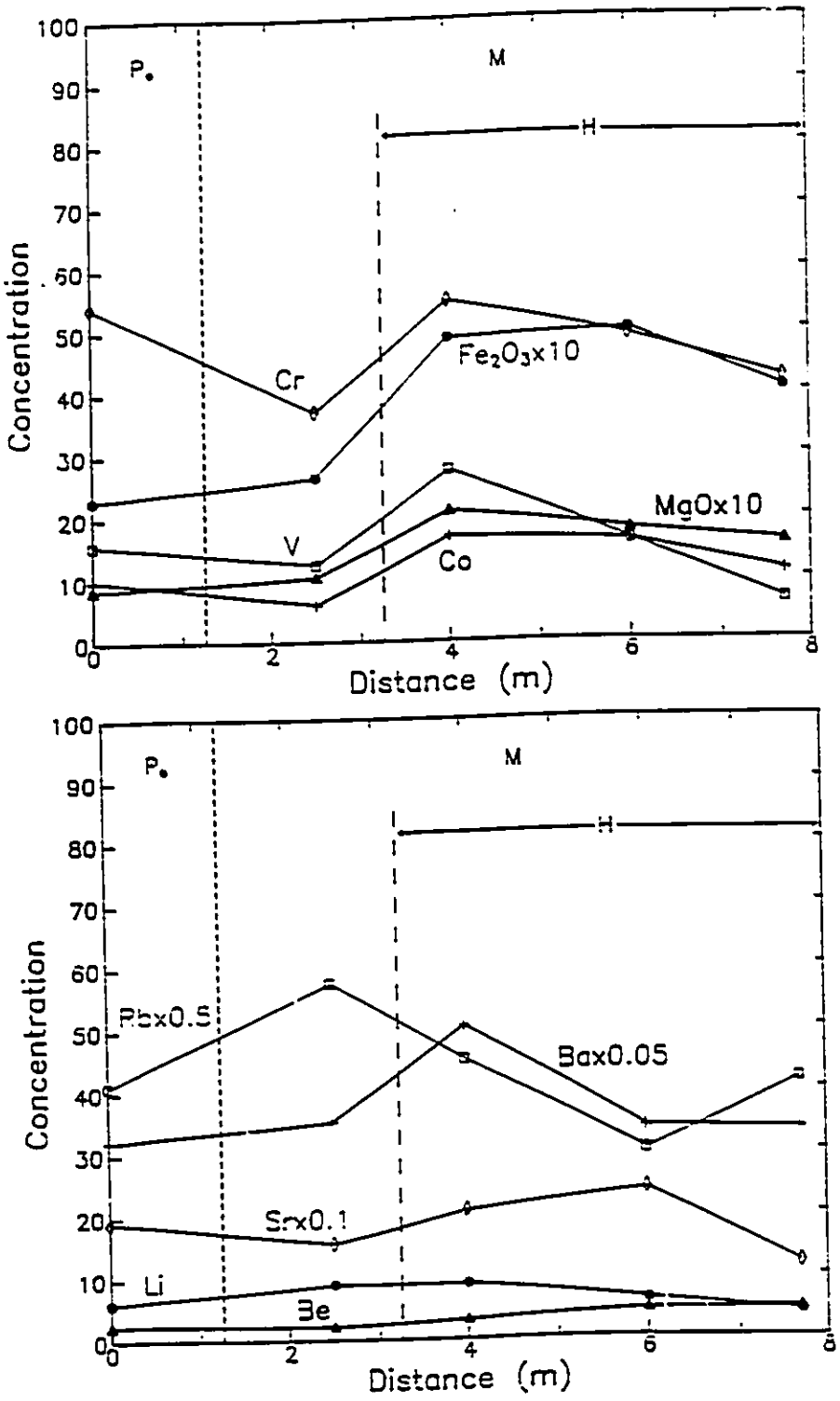

Fig.49. Plot of scaled concentrations of selected major and trace elements versus distance across the Parkhill West shear zone. Divisions and labels as in Fig.48.

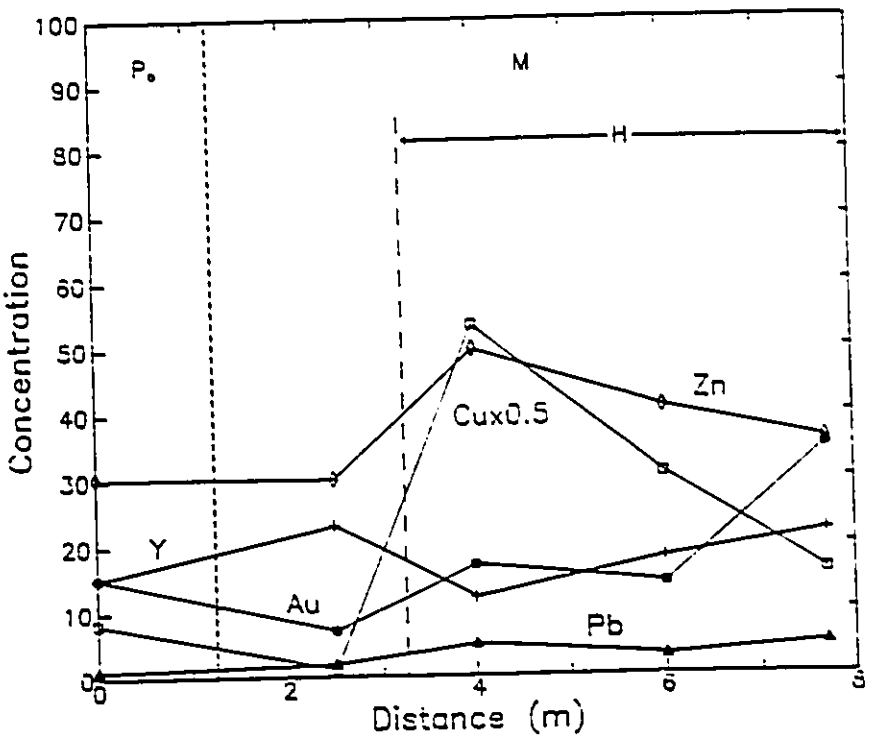

Fig.50. Plot of scaled concentrations of selected trace elements versus distance across the Parkhill West shear zone. Divisions and labels as in Fig.48.

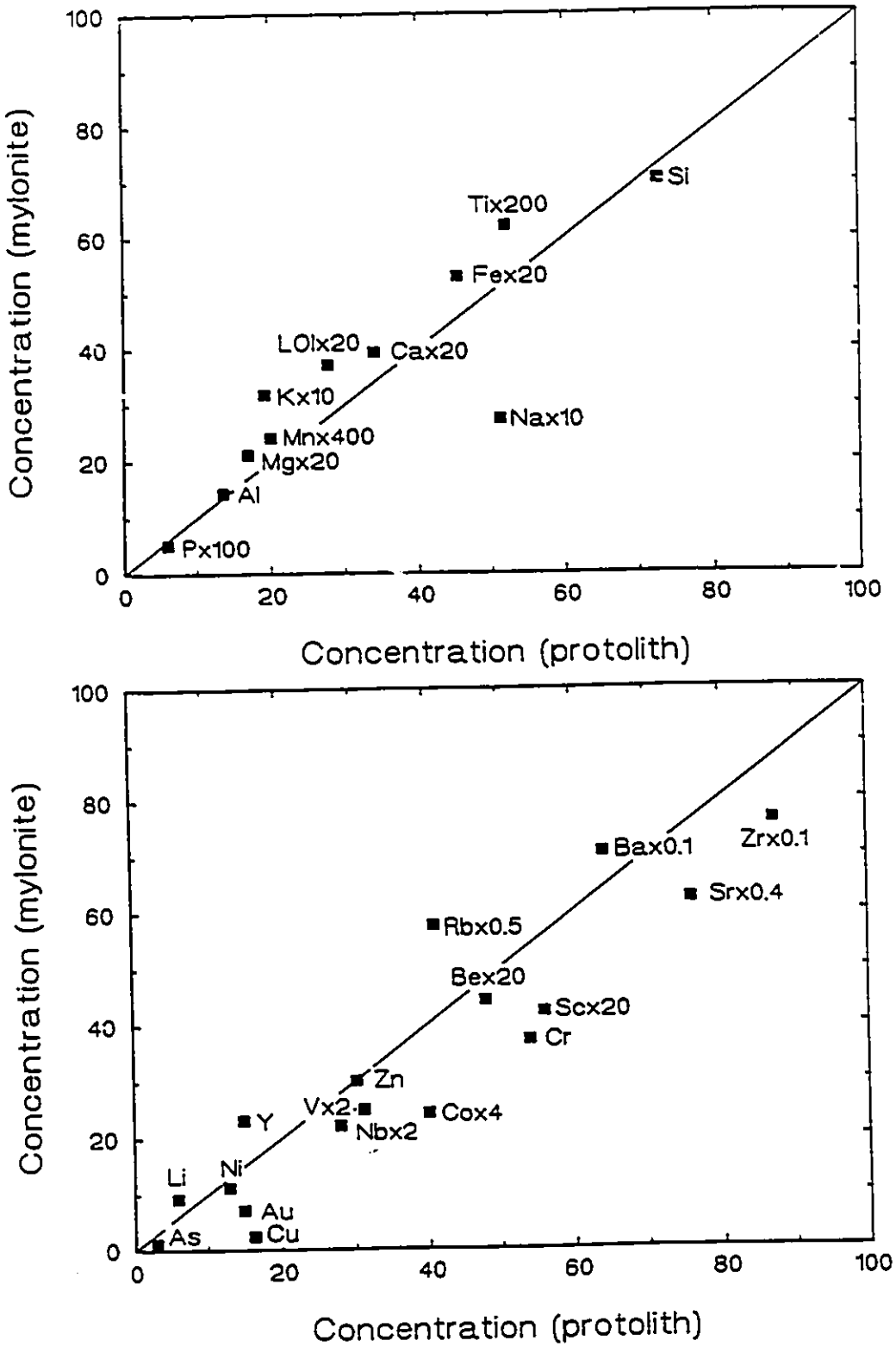

Fig.51. Plot of concentrations of major and trace elements in Parkhill West mylonite versus concentrations in the protolith.

CHAPTER 6

DISCUSSION AND CONCLUSIONS

In this study, the effects of deformation and hydrothermal alteration in several small shear zones at Wawa have been examined. The strained and altered rocks have been characterized on the basis of their feldspar grain-sizes. Chemical changes accompanying grain-size reduction point to an overall loss of volume accompanying removal of soluble components, particularly those that compose feldspar, and relative increases in the least mobile components.

Grain-size reduction is implicit in the formation of mylonites and related rocks. The mechanisms of grain-size reduction necessitates the availability of hydrothermal fluids, particularly aqueous fluids. Many altered rocks have LOI values which lie close to the volume-loss isocon along with the immobile elements. This probably represents the amount of water added to the system accompanying the breakdown of feldspar and its replacement by either muscovite or epidote. In some of the shear zones studied, an overall volume gain may be the result of subsequent hydrothermal alteration and feldspar grain growth. Minto A, Minto C and Grace Darwin show evidence of the presence of CO_2-rich fluids. They have Ca and LOI values that, if plotted for the hydrothermally altered rocks, would lie well within the field of enrichment.

Grain-size data implies some differences in the behaviour of different types of feldspars. Alkali feldspar grains appear to be more susceptible to alteration and break down more readily than plagioclase feldspars. In some cases (Fred C, Jubilee, Parkhill West) alkali feldspar is totally removed from the sheared rocks. Plagioclase feldspar appears to be more resistant, breaks down less readily and generally forms rounded augen in the mylonites. In many of the deformed rocks, adjacent plagioclase and alkali feldspar clasts appear differently. The alkali feldspar grains are rounded and highly altered to muscovite such that

most of the original feldspar material has been altered. The adjacent plagioclase grains are commonly more angular and show little or no evidence of internal replacement by alteration.

Wall-rock alteration and mineralization is identified within the shear zones by anomalous chemical patterns. Often this involves additions of Si, K, Cu, ±As, ±Au, ±Rb, ±Ba, ±Fe. Fred C, Grace Darwin, and Minto A are characterized by alterations of this type which are constrained within relatively narrow bands of high-strain rocks. Because mineralization is concentrated in the most deformed rocks, it may be implied that deformation occurred prior to this hydrothermal event and fluids were concentrated along the deformation zones of enhanced permeability.

Data from the Jubilee shear zone indicate alteration involving addition of K, Rb, Cu and Au over a relatively wide area of the shear zone, not constrained to the most deformed rocks. These patterns, along with petrographic evidence, indicates that the last deformation event occurred after mineralization. Sampling control in Minto E is limited to one side of the shear zone, but chemical patterns indicate alteration involving additions of Si, K, Rb, Ba, Cu, As and Au prior to the last deformation event.

Chemical profiles from the Minto C shear zone indicate a complex history of deformation and alteration. An early mineralization event characterized by anomalous Si, K, Ba, Cu, As and Au is evident in a relatively broad area within the shear zone. Mineralization may have been controlled by a pre-existing deformation zone which acted as a conduit for fluid infiltration. Adjacent to these mylonites is an ultramylonite which has sharp increases in Ti, Si, Fe, Cr, Mg, Co, Rb, Be, and Zn. This may represent a later period of mineralization accompanying or subsequent to the last deformation event.

The Parkhill shear zone also shows evidence of multiple episodes of alteration and deformation. An early mineralization event characterized by anomalous Si and Cu may have followed an early deformation event which resulted in volume loss and enrichments of

refractory components including Ti, Zr, P and the First Transition Series elements. This is overprinted by later deformation and a second mineralization event characterized by the additions of Rb, K, As and Au.

Shear zone attitudes in the study area are generally either NW or NE striking. The NW striking shear zones appear to display similar histories of alteration and deformation. Fred C, Grace Darwin, and Minto A all show evidence of pre-mineralization deformation and have narrow, tightly constrained mineralized zones. Both the Jubilee shear and Minto E shear zone are NE striking and show evidence of post-mineralization deformation. Minto C and Parkhill are also NE striking and show evidence of multiple deformation and mineralization episodes. Structurally, Jubilee shear is cross-cut and offset by the later NW striking Parkhill fault. It may be implied that the NE shear zones are all earlier and related to each other in time and that the NW zones were later and subject to a shorter, less complex history.

A temporal model of deformation and mineralization events is proposed on the basis of the available chemical, structural and petrographic data. An early deformation event, D_1, produced northeasterly-trending shear zones with enhanced permeability. These acted as conduits for the earliest period of mineralization, M_1, by aqueous fluids carrying Si, K, Rb, Ba, Au, As, and Cu. The Jubilee, Minto E, Minto C and Parkhill shear zones all show M_1. The early mineralization is deformed by a northeasterly reactivation, D_2, which is observed at Minto C and Parkhill. A second period of mineralization along D_2 shears enriched K, Rb, Sr, and Si at Minto C and K, Rb, Au and As at Parkhill.

The last deformational event, D_3, in the area produced northwesterly-trending shear zones which offset earlier structural features. These zones, Minto A, Fred C and Grace Darwin, served as conduits for the last mineralization, M_3, which is typified by additions of Si, K, Cu, Au and As with some variations in other elements. Fluids accompanying the last mineralization seem to have been CO_2-rich as opposed to an earlier deformation by CO_2-

poor fluids. It may be, however, that evidence of earlier carbonate-deposition has been removed by subsequent fluids accompanying deformation.

This model must of course be confirmed by detailed structural analysis and petrographic studies of the mineralization.

Appendix A

Staining techniques

METHOD FOR STAINING UNCOVERED THIN SECTIONS after Hutchinson, 1974.

1. Etch the rock surface by leaving it face down for 10 seconds over concentrated HF at room temperature.

2. Immerse the slide in saturated sodium cobaltinitrite solution for 15 seconds. The K-feldspar stains light yellow.

3. Rinse briefly in tap water to remove excess reagent.

4. Dip the slide quickly in and out of the barium chloride solution.

5. Rinse briefly, first with tap water, then with distilled water.

6. Cover the rock surface with the rhodizonate reagent from a dropping bottle. When the plagioclase becomes pink, rinse in tap water.

7.Allow the slide to dry before covering.

Reagents Used in above procedure:

Hydrofluoric acid, concentrated 48%.

Five percent barium chloride solution in water.

Saturated sodium colbaltinitrite solution in water.

Preparation: add 20 g sodium coblatinitrite to 60 ml of distilled water such that there remains a residue of undissolved reagent.

Rhodizonate reagent.

Preparation: dissolve 0.05 g rhodizonic acid potassium salt in 20 ml distilled water. Reagent is unstable so must be prepared fresh.

Appendix B

Tables 1-16

Modal analyses and statistics of grain-size measurements

TABLE 1. Modal analysis, Fred C shear zone.

	FC-90-1 P_o	FC-90-2 P	FC-90-3 --	FC-90-4 M
Quartz	57.9	32.3	47.7	28.4
Plagioclase	11.9	26.7	19.2	19.2
Alkali Feldspar	8.0	3.3	2.9	2.6
Muscovite	17.8	23.3	5.6	17.3
Biotite	3.7	6.6	2.4	2.3
Chlorite	0.0	0.0	21.1	18.5
Epidote	0.0	0.0	0.0	0.0
Calcite	0.0	7.0	0.0	0.8
Zircon	0.2	0.0	0.0	0.0
Opaques	0.5	0.8	1.1	10.9
TOTAL	100.0	100.0	100.0	100.0

	FC-90-5 U	FC-90-6 U	FC-90-7 U	FC-90-8 U
Quartz	20.5	20.3	28.4	32.9
Plagioclase	20.2	38.3	23.9	23.5
Alkali Feldspar	1.5	0.0	1.3	0.0
Muscovite	10.0	29.8	18.8	17.9
Biotite	0.8	0.1	0.0	0.4
Chlorite	41.4	0.0	10.0	10.4
Epidote	1.3	0.2	0.0	0.0
Calcite	1.7	3.2	8.8	10.9
Zircon	0.1	0.3	0.0	0.0
Opaques	2.5	7.8	8.8	4.0
TOTAL	100.0	100.0	100.0	100.0

	FC-90-9 M	FC-90-10 M
Quartz	33.2	37.9
Plagioclase	24.8	23.2
Alkali Feldspar	0.6	0.0
Muscovite	29.8	24.1
Biotite	0.0	0.0
Chlorite	0.0	0.6
Epidote	0.0	0.0
Calcite	8.6	9.3
Zircon	0.0	0.0
Opaques	3.0	4.9
TOTAL	100.0	100.0

TABLE 2a. Statistics of plagioclase feldspar grain-size data for the Fred C shear zone.

	FC-90-1	FC-90-2	FC-90-3	FC-90-4	FC-90-5
n	61	71	15	48	53
$\bar{x}$	1.126	1.059	4.24	2.343	2.846
M	1.179	0.767	4.236	2.175	2.966
σ	0.866	1.362	1.162	0.986	0.834
mode*	1.25	-0.25/0.75	4.25	1.75	3.00
skewness	0.134	0.600	0.175	0.384	0.171
kurtosis	0.107	-0.434	-0.723	-0.537	0.708
K-S	0.059	0.126	0.109	0.087	0.070

	FC-90-6	FC-90-7	FC-90-8	FC-90-9	FC-90-10
n	70	64	99	69	65
$\bar{x}$	3.551	2.891	2.603	3.459	3.131
M	3.585	3.003	2.441	3.487	3.043
σ	0.983	1.076	0.961	0.879	1.086
mode*	3.75	2.25/3.75	2.00	2.75/3.75	3.75
skewness	0.154	0.106	0.563	0.054	0.384
kurtosis	0.258	-0.926	-0.156	-0.465	-0.434
K-S	0.064	0.104	0.083	0.049	0.058

Table 2b. Statistics of alkali feldspar grain size data for the Fred C shear zone.

	FC-90-1	FC-90-2	FC-90-3	FC-90-4
n	27	17	4	7
$\bar{x}$	1.602	3.190	4.473	4.184
M	1.603	3.550	4.502	4.108
σ	0.809	1.335	0.225	0.657
mode*	1.75	3.75	4.50	3.25/4.25
skewness	0.221	-1.918	-0.226	0.353
kurtosis	1.119	3.222	-4.706	-1.301
K-S	0.086	0.197	0.222	0.145

	FC-90-5	FC-90-6	FC-90-7	FC-90-9
n	4	7	8	5
$\bar{x}$	4.814	6.167	4.039	4.775
M	4.850	6.422	3.907	4.769
σ	0.311	0.752	0.663	0.840
mode*	4.750	5.75/6.75	4.750	4.750
skewness	-0.520	-0.295	0.265	-1.006
kurtosis	-1.159	-1.294	-1.763	1.558
K-S	0.152	0.175	0.149	0.142

n=number of grains; $\bar{x}$=average grain size (phi units); M=median; σ=population standard deviation; K-S=Kolmogorov-Smirnov critical values; * where sample is bimodal, both modes are given.

TABLE 3. Modal analysis, Grace Darwin shear zone.

	GD-90-1 P_0	GD-90-2 $_pO$	GD-90-3 P_0	GD-90-4 P
Quartz	29.2	9.0	3.4	8.0
Plagioclase	4.3	27.0	30.4	22.1
Muscovite	0.0	0.0	0.0	0.0
Biotite	30.1	41.7	28.2	38.6
Chlorite	19.2	7.9	14.8	13.2
Epidote	12.3	13.9	14.9	13.7
Calcite	1.0	0.0	0.2	1.6
Opaques	3.9	0.5	8.1	2.8
TOTAL	100.0	100.0	100.0	100.0

	GD-90-5 P	GD-90-6 M	GD-90-7 P	GD-90-8 P
Quartz	3.6	21.1	31.5	27.2
Plagioclase	29.4	44.4	13.8	1.2
Muscovite	0.0	4.5	33.3	51.0
Biotite	34.1	25.9	5.3	7.9
Chlorite	11.4	0.0	4.5	0.0
Epidote	21.4	0.0	0.0	0.0
Calcite	0.0	0.0	0.3	0.0
Opaques	0.1	4.1	11.3	12.7
TOTAL	100.0	100.0	100.0	100.0

	GD-90-9 P	GD-90-10 U	GD-90-11 M
Quartz	34.5	19.1	7.0
Plagioclase	11.9	34.1	37.3
Muscovite	38.6	0.4	0.0
Biotite	10.3	16.1	2.4
Chlorite	0.0	18.1	36.6
Epidote	0.0	2.9	3.7
Calcite	0.0	1.9	0.0
Opaques	4.7	7.4	13.0
TOTAL	100.0	100.0	100.0

TABLE 4. Statistics of plagioclase grain-size data for the Grace Darwin shear zone.

	GD-90-1	GD-90-2	GD-90-3	GD-90-4	GD-90-5	GD-90-6
n	68	36	46	68	81	48
$\bar{x}$	2.482	2.401	2.550	2.842	3.132	4.143
M	2.520	2.209	2.394	2.769	3.150	4.181
σ	0.743	0.882	0.744	0.611	0.919	0.759
mode*	1.75/2.75	1.75/2.75	1.75	2.75	3.25	4.25
skewness	0.856	0.527	0.412	0.348	0.047	0.363
kurtosis	1.494	-0.449	-0.984	-0.391	-0.672	0.056
K-S	0.083	0.103	0.141	0.061	0.051	0.084

	GD-90-7	GD-90-8	GD-90-9	GD-90-10	GD-90-11
n	63	9	68	31	33
$\bar{x}$	3.475	3.625	2.482	5.354	4.096
M	3.318	3.157	2.520	5.352	4.203
σ	0.807	1.122	0.743	0.685	0.971
mode*	3.25	3.25	1.75/2.75	5.00	4.25
skewness	0.305	0.659	0.856	0.712	-0.220
kurtosis	-0.459	-0.277	1.494	0.686	0.825
K-S	0.122	0.217	0.083	0.136	0.104

n=number of grains; $\bar{x}$=average grain size (phi units); M=median; σ=population standard deviation; K-S=Kolmogorov-Smirnov critical values; * where sample is bimodal, both modes are given.

TABLE 5. Modal analysis, Jubilee shear zone.

	JS-90-1 P_0	JS-90-2 P_0	JS-90-3 P	JS-90-4 M
Quartz	21.1	20.5	26.4	26.9
Plagioclase	47.0	59.5	28.0	22.1
Alkali Feldspar	1.3	0.0	0.0	0.0
Muscovite	0.0	0.0	6.9	21.7
Biotite	7.0	4.7	13.5	4.7
Chlorite	5.2	3.4	13.2	6.5
Epidote	13.3	6.3	0.0	0.0
Calcite	2.0	3.0	9.6	0.0
Zircon	0.1	0.0	0.0	0.0
Opaques	3.0	2.6	2.4	18.1
Tourmaline	0.0	0.0	0.0	0.0
TOTAL	100.0	100.0	100.0	100.0

	JS-90-5 M	JS-90-6 M	JS-90-7 U	JS-90-8 M
Quartz	39.9	25.2	9.4	24.1
Plagioclase	0.3	4.0	13.9	27.1
Alkali Feldspar	0.0	0.0	0.0	0.0
Muscovite	37.2	40.1	59.6	7.7
Biotite	5.6	1.2	6.3	12.7
Chlorite	5.0	2.2	5.8	14.9
Epidote	0.0	0.0	0.0	3.7
Calcite	8.6	21.2	0.0	4.5
Zircon	0.2	0.0	0.0	0.0
Opaques	3.2	4.8	5.0	5.3
Tourmaline	0.0	1.3	0.0	0.0
TOTAL	100.0	100.0	100.0	100.0

TABLE 6a. Statistics of plagioclase feldspar grain-size data for the Jubilee shear zone.

	JS-90-1	JS-90-2	JS-90-3	JS-90-4
n	39	21	29	36
$\bar{x}$	1.559	1.126	1.839	3.469
M	1.523	1.191	1.95	3.442
σ	1.025	0.802	0.947	1.008
mode*	1.750	1.000	2.000	3.25/4.25
skewness	0.250	-0.045	-0.264	-0.159
kurtosis	-0.419	-0.082	-0.766	0.567
K-S	0.116	0.630	0.069	0.110
	JS-90-5	JS-90-6	JS-90-7	JS-90-8
n	7	21	29	37
$\bar{x}$	4.277	3.958	5.108	4.096
M	4.231	3.909	5.064	4.093
σ	1.164	0.900	0.834	1.220
mode*	4.000	3.750	4.750	3.75/4.75
skewness	0.447	-0.282	-0.350	-0.134
kurtosis	0.166	0.400	0.372	-0.637
K-S	0.167	0.088	0.069	0.083

Table 6b. Statistics of alkali feldspar grain-size data for the Jubilee shear zone.

	JS-90-1	JS-90-3
n	4	5
$\bar{x}$	2.193	2.377
M	2.136	2.681
σ	0.870	1.345
mode*	1.5/3.0	1.0/3.25
skewness	0.294	-0.422
kurtosis	-1.650	-2.234
K-S	0.190	0.179

n=number of grains; $\bar{x}$=average grain size (phi units); M=median; σ=population standard deviation; K-S=Kolmogorov-Smirnov critical values; * where sample is bimodal, both modes are given.

TABLE 7. Modal analysis, Minto A shear zone.

	MA-90-1 P_o	MA-90-2 $_pO$	MA-90-3 P	MA-90-4 U
Quartz	29.9	24.2	18.3	29.9
Plagioclase	19.7	31.0	40.2	6.2
Alkali Feldspar	4.5	9.6	0.8	0.0
Muscovite	6.7	9.2	13.7	38.6
Biotite	4.6	1.3	0.7	0.0
Chlorite	27.1	21.3	19.5	13.2
Calcite	3.5	0.0	0.4	8.5
Epidote	1.7	0.0	0.2	2.3
Zircon	0.0	0.0	0.3	0.0
Opaques	2.3	3.4	5.9	1.3
TOTAL	100.0	100.0	100.0	100.0

TABLE 8a. Statistics of plagioclase feldspar grain-size data for the Minto A shear zone.

	MA-90-1	MA-90-2	MA-90-3	MA-90-4
n	27	27	32	21
$\bar{x}$	1.400	1.383	1.416	4.576
M	1.090	1.175	1.563	4.642
σ	1.157	1.242	0.994	1.013
mode*	0.5/1.75	1.25	1.75	4.75
skewness	0.588	0.805	-0.176	-0.877
kurtosis	-0.573	0.491	-0.45	0.825
K-S	0.125	0.102	0.097	0.103

TABLE 8b. Statistics of alkali feldspar grain size-data for the Minto A shear zone.

	MA-90-1	MA-90-2	MA-90-3	MA-90-4
n	15	5	8	7
$\bar{x}$	2.302	2.018	1.952	5.264
M	1.959	1.472	2.330	5.029
σ	1.475	1.324	1.095	0.774
mode*	1.75/3.5	1.25	2.75	4.75
skewness	-0.319	1.799	-0.747	0.908
kurtosis	-0.864	3.347	-0.854	-0.210
K-S	0.125	0.293	0.157	0.218

n=number of grains; $\bar{x}$=average grain size (phi units); M=median; σ=population standard deviation; K-S=Kolmogorov-Smirnov critical values; * where sample is bimodal, both modes are given.

TABLE 9. Modal analysis, Minto C shear zone.

	MC-90-1 P_0	MC-90-2 M	MC-90-3 U	MC-90-4 M
Quartz	23.5	27.9	16.2	45.3
Plagioclase	21.4	31.9	5.7	7.8
Muscovite	0.0	0.5	26.4	41.2
Biotite	20.3	2.7	0.0	0.0
Chlorite	6.4	30.9	25.7	0.0
Epidote	28.2	0.0	15.3	0.0
Calcite	0.0	0.0	7.0	0.0
Zircon	0.0	0.0	0.1	0.0
Opaques	0.2	6.1	3.6	5.7
TOTAL	100.0	100.0	100.0	100.0

	MC-90-7 P	MC-90-8 P_0
Quartz	26.5	38.4
Plagioclase	50.6	35.8
Muscovite	5.2	10.6
Biotite	5.4	2.6
Chlorite	7.4	4.3
Epidote	4.2	6.8
Calcite	0.0	0.5
Zircon	0.1	0.1
Opaques	0.6	0.9
TOTAL	100.0	100.0

TABLE 10. Statistics of plagioclase feldspar grain-size data for the Minto C shear zone.

	MC-90-1	MC-90-2	MC-90-3	MC-90-4
n	33	38	20	24
$\bar{x}$	1.648	3.514	4.623	2.902
M	1.391	3.910	4.555	3.098
σ	1.326	1.464	0.477	1.262
mode*	1.25	2.25/4.5	4.75	1.75
skewness	0.339	-0.566	0.320	0.296
kurtosis	-0.098	-0.241	2.522	-0.575
K-S	0.121	0.099	0.152	0.139

	MC-90-7	MC-90-8
n	31	39
$\bar{x}$	2.106	1.169
M	1.988	1.127
σ	1.585	0.911
mode*	1.25	0.75
skewness	0.510	0.686
kurtosis	-0.022	0.951
K-S	0.114	0.103

n=number of grains; $\bar{x}$=average grain size (phi units); M=median; σ=population standard deviation; K-S=Kolmogorov-Smirnov critical values; * where sample is bimodal, both modes are given.

TABLE 11. Modal analysis, Minto E shear zone.

	ME-90-1 P	ME-90-2 P	ME-90-3 P
Quartz	28.7	24.4	21.3
Plagioclase	20.5	24.0	29.1
Alkali Feldspar	0.0	0.0	0.0
Muscovite	0.0	2.9	2.2
Biotite	7.5	7.1	8.8
Chlorite	18.7	26.1	25.3
Epidote	22.9	8.5	2.3
Calcite	1.5	4.2	8.3
Zircon	0.0	0.0	0.0
Opaques	0.2	2.8	2.7
TOTAL	100.0	100.0	100.0

	ME-90-4 M	ME-90-5 P
Quartz	6.7	24.0
Plagioclase	45.9	33.3
Alkali Feldspar	0.0	0.0
Muscovite	5.2	29.2
Biotite	1.1	3.0
Chlorite	39.7	3.9
Epidote	0.0	0.0
Calcite	0.2	1.2
Zircon	0.0	0.1
Opaques	1.2	5.3
TOTAL	100.0	100.0

TABLE 12. Statistics of plagioclase feldspar grain-size data for the Minto E shear zone.

	ME-90-1	ME-90-2	ME-90-3	ME-90-4	ME-90-5
n	33	33	27	30	34
$\bar{x}$	2.040	2.216	2.086	4.074	2.186
M	2.081	1.908	2.073	3.968	2.095
σ	1.006	1.275	0.797	0.741	1.050
mode*	2.25	1.75	2.25	3.75	1.25/2.5
skewness	-0.262	0.761	0.227	0.937	0.149
kurtosis	-0.209	0.247	0.464	1.620	-0.262
K-S	0.065	0.116	0.062	0.111	0.075

n=number of grains; $\bar{x}$=average grain size (phi units); M=median; σ=population standard deviation; K-S=Kolmogorov-Smirnov critical values; * where sample is bimodal, both modes are given.

TABLE 13. Modal analysis, Parkhill East shear zone.

	PHE-90-1 P_0	PHE-90-2 P	PHE-90-3 P	PHE-90-4 M
Quartz	27.3	44.4	19.9	80.1
Plagioclase	17.5	15.6	10.8	3.3
Alkali Feldspar	0.0	0.0	0.0	0.0
Muscovite	0.0	0.6	0.0	0.0
Biotite	11.0	16.2	28.7	7.5
Chlorite	15.4	2.9	9.7	1.9
Epidote	27.9	20.1	27.0	2.3
Calcite	0.0	0.0	3.6	4.7
Titanite	0.0	0.0	0.2	0.0
Zircon	0.0	0.0	0.0	0.0
Amphibole	0.0	0.0	0.0	0.0
Opaques	0.9	0.2	0.1	0.2
TOTAL	100.0	100.0	100.0	100.0

	PHE-90-5 M	PHE-90-7 M	PHE-90-8 M
Quartz	18.6	35.6	27.8
Plagioclase	22.2	11.6	14.2
Alkali Feldspar	0.0	0.0	0.0
Muscovite	0.0	0.0	0.0
Biotite	14.8	12.3	13.4
Chlorite	10.7	5.9	0.0
Epidote	17.6	24.2	19.0
Calcite	14.3	7.5	0.2
Titanite	0.0	0.2	0.0
Zircon	0.1	0.1	0.0
Amphibole	0.0	0.1	25.4
Opaques	1.7	2.5	0.0
TOTAL	100.0	100.0	100.0

TABLE 14. Statistics of plagioclase feldspar grain-size data for the Parkhill East shear zone.

	PHE-90-1	PHE-90-2	PHE-90-3	PHE-90-4
n	119	95	68	54
$\bar{x}$	2.61	3.058	3.022	4.194
M	2.502	3.135	3.025	4.103
σ	0.993	0.884	0.883	1.057
mode*	2.25	3.25	2.75/3.75	3.25/4.75
skewness	0.262	-0.001	-0.046	0.194
kurtosis	-0.663	-0.508	-0.439	-0.621
K-S	0.092	0.089	0.049	0.110

	PHE-90-5	PHE-90-7	PHE-90-8
n	70	58	77
$\bar{x}$	4.376	3.977	3.759
M	4.393	4.060	3.703
σ	0.676	0.860	0.913
mode*	4.25	4.25	3.75
skewness	0.116	-0.315	-0.304
kurtosis	-0.646	0.846	0.368
K-S	0.049	0.061	0.056

n=number of grains; $\bar{x}$=average grain size (phi units); M=median; σ=population standard deviation; K-S=Kolmogorov-Smirnov critical values; * where sample is bimodal, both modes are given.

TABLE 15. Modal analysis, Parkhill West shear zone.

	PHW-90-1 P_o	PHW-90-2 M	PHW-90-3 M
Quartz	41.6	39.2	41.2
Plagioclase	23.3	15.6	6.2
Alkali Feldspar	3.1	2.2	1.2
Muscovite	16.0	28.2	34.9
Biotite	3.6	8.5	2.4
Chlorite	6.0	3.6	8.7
Calcite	2.5	1.3	0.5
Zircon	0.1	0.0	0.0
Opaques	3.8	1.4	4.9
Amphibole	0.0	0.0	0.0
TOTAL	100.0	100.0	100.0

	PHW-90-4 M	PHW-90-5 M
Quartz	31.1	44.9
Plagioclase	13.5	4.8
Alkali Feldspar	0.0	0.0
Muscovite	38.1	30.4
Biotite	5.5	2.2
Chlorite	1.3	4.6
Calcite	2.1	7.5
Zircon	0.0	0.0
Opaques	1.1	5.6
Amphibole	7.3	0.0
TOTAL	100.0	100.0

TABLE 16a. Statistics of plagioclase feldspar grain-size data for the Parkhill West shear zone.

	PHW-90-1	PHW-90-2	PHW-90-3	PHW-90-4	PHW-90-5
n	40	29	44	39	29
$\bar{x}$	5.017	4.469	4.144	3.993	4.671
M	4.999	4.655	4.305	4.339	4.810
σ	1.032	1.246	1.081	1.417	0.758
mode*	5.25	4.75	3.25/4.75	4.75	4.75
skewness	-0.029	-0.395	-0.199	-0.304	-0.192
kurtosis	-0.340	-0.170	-0.737	-0.524	-0.408
K-S	0.093	0.146	0.091	0.100	0.109

TABLE 16b. Statistics of alkali feldspar grain-size data for the Parkhill West shear zone.

	PHW-90-1	PHW-90-2	PHW-90-3
n	13	9	7
$\bar{x}$	5.448	4.715	5.505
M	5.381	5.109	5.725
σ	0.631	1.409	1.021
mode*	4.75	5.75	4.25/6.25
skewness	0.095	-0.826	-0.590
kurtosis	-1.560	-0.970	-1.454
K-S	0.176	0.181	0.191

n=number of grains; $\bar{x}$=average grain size (phi units); M=median; σ=population standard deviation; K-S=Kolmogorov-Smirnov critical values; * where sample is bimodal, both modes are given.

Appendix C

Petrographic classification of deformed rocks

TABLE 17. Petrographic classification of deformed rocks.

Fred C shear zone

Sample	Median Grain Size (ϕ) Alkali feldspar	Plagioclase	Classification
FC-90-1	1.60	1.18	protolith
FC-90-2	3.55	0.77	protomylonite
FC-90-3	4.50	4.24	(mylonite)
FC-90-4	4.11	2.18	mylonite
FC-90-5	4.85	2.97	ultramylonite
FC-90-6	6.42	3.59	ultramylonite
FC-90-7	3.91	3.00	ultramylonite
FC-90-8	--	2.44	ultramylonite
FC-90-9	4.77	3.49	mylonite
FC-90-10	--	3.04	mylonite

Grace Darwin shear zone

Sample	Median Grain Size (ϕ) Alkali feldspar	Plagioclase	Classification
GD-90-1	--	2.52	protolith
GD-90-2	--	2.21	protolith
GD-90-3	--	2.39	protolith
GD-90-4	--	2.77	protomylonite
GD-90-5	--	3.15	protomylonite
GD-90-6	--	4.18	mylonite
GD-90-7	--	3.32	protomylonite
GD-90-8	--	3.16	protomylonite
GD-90-9	--	2.52	protomylonite
GD-90-10	--	5.35	ultramylonite
GD-90-11	--	4.20	mylonite

Jubilee shear zone

Sample	Median Grain Size (ϕ) Alkali feldspar	Plagioclase	Classification
JS-90-1	2.14	1.52	protolith
JS-90-2	--	1.19	protolith
JS-90-3	2.68	1.95	protomylonite
JS-90-4	--	3.44	mylonite
JS-90-5	--	4.23	mylonite
JS-90-6	--	3.91	mylonite
JS-90-7	--	5.06	ultramylonite
JS-90-8	--	4.09	mylonite

TABLE 17. continued.

Minto A shear zone

Sample	Median Grain Size (ϕ) Alkali feldspar	Plagioclase	Classification
MA-90-1	1.96	1.09	protolith
MA-90-2	1.47	1.18	protolith
MA-90-3	2.33	1.56	protomylonite
MA-90-4	5.03	4.64	ultramylonite

Minto C shear zone

Sample	Median Grain Size (ϕ) Alkali feldspar	Plagioclase	Classification
MC-90-1	--	1.39	protolith
MC-90-2	--	3.91	mylonite
MC-90-3	--	4.56	ultramylonite
MC-90-4	--	3.10	mylonite
MC-90-7	--	1.99	protomylonite
MC-90-8	--	1.13	protolith

Minto E shear zone

Sample	Median Grain Size (ϕ) Alkali feldspar	Plagioclase	Classification
ME-90-1	--	2.08	protomylonite
ME-90-2	--	1.91	protomylonite
ME-90-3	--	2.07	protomylonite
ME-90-4	--	3.97	mylonite
ME-90-5	--	2.10	protomylonite

TABLE 17. continued.

Parkhill East shear zone

Sample	Median Grain Size (ϕ) Alkali feldspar	Plagioclase	Classification
PHE-90-1	--	2.50	protolith
PHE-90-2	--	3.14	protomylonite
PHE-90-3	--	3.03	protomylonite
PHE-90-4	--	4.10	mylonite
PHE-90-5	--	4.39	mylonite
PHE-90-6	--	--	mylonite
PHE-90-7	--	4.06	mylonite
PHE-90-8	--	3.70	mylonite

Parkhill West shear zone

Sample	Median Grain Size (ϕ) Alkali feldspar	Plagioclase	Classification
PHW-90-1	5.38	5.00	protolith
PHW-90-2	5.11	4.66	mylonite
PHW-90-3	5.73	4.31	mylonite
PHW-90-4	--	4.34	mylonite
PHW-90-5	--	4.81	mylonite

Appendix D

Analytical methods, precision and accuracy

Chemical analyses were made by X-ray Assay Laboratories of Don Mills, Ontario (XRAL) using a variety of techniques. Major and minor elements were determined using x-ray fluorescence spectrometry (XRF) on fused glass discs employing a method based on that of Norrish and Hutton (1969). Loss on ignition (LOI) represents weight loss following heating to 1000°C of a preweighed sample. The elements Ba, Rb, Sr, CR, Zr, Y, and Nb were determined by XRF on pressed powder specimens using Compton scattering to correct for mass absorption and background (Feather and Willis, 1976). Determinations of Li, Be, V, Co, Ni, Cu, Zn, and Sc were made by Induction Coil Plasma Spectrometry (ICP) and As and Au by instrumental neutron activation (INA).

Analytic precisions along with detection limits for each element are given in Table 18. Precisions are estimated from analytic results from duplicate determinations on samples and repeated determinations on control standards. Duplicate pairs are run at a frequency of 8 - 15 % of total samples in a run, depending on the stability of the instrumentation. The actual analytic precision for each element is estimated for each sample according to the concentration of the element in terms of multiples of the detection limit. As in most analytic techniques, the precision improves as the concentration increases. The precision values quoted in Table 18 are weighted averages for all the samples analyzed. Analytic precisions for individual samples or concentration ranges are available from the author on request.

Table 18. Analytic techniques, detection limits and precision.

Element	Method	Units	Detection limit	Precision*
SiO_2	XRF	Wt.%	0.01	0.9%
TiO_2	XRF	Wt.%	0.001	1.5%
Al_2O_3	XRF	Wt.%	0.01	0.8%
Fe_2O_3*	XRF	Wt.%	0.01	2.7%
MnO	XRF	Wt.%	0.01	0.8%
MgO	XRF	Wt.%	0.01	2.2%
CaO	XRF	Wt.%	0.01	1.3%
Na_2O	XRF	Wt.%	0.01	4.9%
K_2O	XRF	Wt.%	0.01	1.7%
P_2O_5	XRF	Wt.%	0.01	0.8%
Rb	XRF	ppm	10	13%
Sr	XRF	ppm	10	6.3%
Ba	XRF	ppm	10	6.6%
Cr	XRF	ppm	10	3.7%
Y	XRF	ppm	10	20%
Zr	XRF	ppm	10	7.1%
Nb	XRF	ppm	10	22%
Li	ICP	ppm	1	23%
Be	ICP	ppm	0.5	16%
V	ICP	ppm	2	6.3%
Co	ICP	ppm	1	8.6%
Ni	ICP	ppm	1	8.7%
Cu	ICP	ppm	0.5	5.8%
Zn	ICP	ppm	0.5	5.3%
Sc	ICP	ppm	0.5	8.2%
Pb	ICP	ppm	2	25%
As	INA	ppm	2	14%
Au	INA	ppb	5	33%
LOI	weight	Wt.%	0.01	4.9%

*Precision reported as Coefficient of Variation.
*Fe_2O_3 as total iron

Appendix E

Tables 19-26

Chemical analyses

TABLE 19: Major element oxide and trace element abundances, Fred C shear zone.

	FC-90-1 P_0	FC-90-2 P	FC-90-3 --	FC-90-4 M	FC-90-5 U
SiO_2	75.30	72.30	73.50	67.20	64.20
TiO_2	0.19	0.26	0.29	0.35	0.47
Al_2O_3	12.70	13.30	13.90	13.90	15.20
Fe_2O_3*	1.61	2.53	2.37	3.63	4.77
MnO	0.03	0.04	0.03	0.07	0.07
MgO	0.44	0.63	0.65	0.90	2.37
CaO	0.90	1.65	0.17	3.22	2.34
Na_2O	4.56	4.84	5.25	3.49	4.59
K_2O	1.99	2.08	1.80	2.44	1.46
P_2O_5	0.03	0.05	0.06	0.07	0.09
LOI	1.70	1.93	1.31	2.85	3.62
TOTAL	99.45	99.61	99.33	98.12	99.18
Li	2	5	3	3	12
Rb	59	59	58	77	62
Be	1.6	1.4	1.2	1.6	1.1
Sr	104	121	72	152	201
Ba	724	813	688	750	573
V	5.0	5.5	<0.5	1.6	18.9
Cr	58	47	42	39	80
Co	5	7	8	13	12
Ni	6	3	2	17	34
Cu	5.1	15.1	31.9	17.4	21.7
Zn	12.0	15.4	19.9	47.5	71.9
Sc	0.5	2.1	0.6	0.8	2.2
Y	21	<10	28	29	11
Zr	108	164	183	164	144
Nb	<10	<10	11	<10	18
As	6	110	5	12	5
Pb	6	<2	4	16	<2
Au	5	42	5	26	7

Major elements given in weight percent (Fe_2O_3*, total Fe as Fe_2O_3); trace elements given in parts per million (gold in parts per billion).

TABLE 19: continued

	FC-90-6 U	FC-90-7 U	FC-90-8 U	FC-90-9 M	FC-90-10 M
SiO_2	70.60	63.30	66.80	70.80	71.80
TiO_2	0.31	0.47	0.49	0.27	0.28
Al_2O_3	13.60	13.50	14.30	13.60	14.20
Fe_2O_3*	3.08	5.38	4.93	2.59	2.10
MnO	0.09	0.13	0.10	0.06	0.04
MgO	0.38	2.35	1.51	0.64	0.43
CaO	2.13	3.08	1.96	1.43	1.14
Na_2O	3.90	3.93	4.22	4.49	4.47
K_2O	2.20	1.36	1.58	2.34	2.31
P_2O_5	0.06	0.09	0.09	0.06	0.06
LOI	3.08	5.54	3.16	3.08	2.62
TOTAL	99.43	99.13	99.14	99.36	99.45
Li	3	13	8	2	1
Rb	55	36	39	52	61
Be	1.4	2.2	1.7	1.2	0.7
Sr	199	162	179	93	99
Ba	617	494	608	609	662
V	4.8	20.5	15.3	7.2	1.5
Cr	50	69	66	59	43
Co	10	19	15	7	6
Ni	15	20	21	5	4
Cu	45.8	18.3	18.5	4.0	2.8
Zn	30.2	128.0	91.5	23.5	23.7
Sc	1.0	2.5	1.9	1.5	1.1
Y	<10	<10	22	<10	23
Zr	170	164	187	179	180
Nb	12	<10	11	16	18
As	110	13	13	15	4
Pb	6	4	<2	5	4
Au	26	10	8	12	8

Major elements given in weight percent (Fe_2O_3*, total Fe as Fe_2O_3); trace elements given in parts per million (gold in parts per billion).

TABLE 20: Major element oxides and trace element abundances, Grace Darwin shear zone.

	GD-90-1 P_o	GD-90-2 P_o	GD-90-3 P_o	GD-90-4 P	GD-90-5 P
SiO_2	61.10	61.70	62.40	61.80	60.30
TiO_2	0.52	0.91	0.90	0.89	1.02
Al_2O_3	15.80	15.10	15.00	14.90	16.50
Fe_2O_3*	7.65	7.03	6.94	7.24	7.42
MnO	0.08	0.09	0.09	0.09	0.11
MgO	2.96	2.16	2.05	2.15	2.38
CaO	4.89	4.65	4.95	4.73	4.08
Na_2O	3.92	3.93	4.10	3.93	5.05
K_2O	1.11	2.02	1.62	1.84	0.75
P_2O_5	0.09	0.26	0.26	0.26	0.28
LOI	0.93	0.93	0.77	1.47	1.39
TOTAL	99.05	98.78	99.08	99.30	99.28
Li	14	12	14	20	9
Rb	43	65	54	46	22
Be	0.7	1.2	1.7	3.7	3.0
Sr	316	345	353	366	247
Ba	478	609	551	429	257
V	69.8	99.3	78.8	103.0	105.0
Cr	99	45	46	57	51
Co	27	20	20	17	13
Ni	46	32	30	30	24
Cu	245.0	14.9	272.0	4.8	20.9
Zn	39.2	52.5	51.0	57.3	52.0
Sc	4.7	6.1	4.8	5.4	7.1
Y	10	17	32	10	25
Zr	103	214	211	214	230
Nb	<10	30	16	25	19
As	3	4	5	6	29
Pb	<2	2	2	<2	3
Au	12	<5	21	12	7

Major elements given in weight percent (Fe_2O_3*, total Fe as Fe_2O_3); trace elements given in parts per million (gold in parts per billion).

TABLE 20: continued.

	GD-90-6 M	GD-90-7 P	GD-90-8 P	GD-90-9 P
SiO_2	63.40	66.80	59.00	65.80
TiO_2	0.93	0.92	0.98	0.90
Al_2O_3	15.50	15.10	16.00	15.00
Fe_2O_3*	6.10	4.94	7.83	5.31
MnO	0.05	0.02	0.02	0.06
MgO	1.43	0.92	0.98	1.63
CaO	2.43	0.72	0.77	2.08
Na_2O	1.66	0.67	0.86	1.02
K_2O	4.13	5.02	4.93	4.24
P_2O_5	0.26	0.26	0.26	0.25
LOI	2.70	2.85	6.47	2.70
TOTAL	98.59	98.22	98.10	98.99
Li	11	5	6	12
Rb	76	91	71	87
Be	3.8	2.3	2.6	4.3
Sr	64	35	30	48
Ba	1890	2720	2640	2100
V	57.8	17.3	19.5	52.5
Cr	40	39	43	46
Co	12	9	28	4
Ni	32	24	29	30
Cu	196.0	250.0	471.0	124.0
Zn	32.3	17.0	20.7	37.8
Sc	4.1	1.4	1.2	3.1
Y	39	27	<10	21
Zr	222	196	234	190
Nb	12	21	27	19
As	1700	1400	21000	75
Pb	6	5	6	2
Au	10000	500	3000	210

Major elements given in weight percent (Fe_2O_3*, total Fe as Fe_2O_3); trace elements given in parts per million (gold in parts per billion).

TABLE 20: continued.

	GD-90-10 U	GD-90-11 M
SiO2	59.40	62.00
TiO2	0.98	0.97
Al2O3	16.00	15.70
Fe2O3*	7.06	5.79
MnO	0.10	0.09
MgO	2.38	3.13
CaO	4.31	4.65
Na2O	4.15	4.93
K2O	2.11	0.53
P2O5	0.27	0.27
LOI	1.70	1.23
TOTAL	98.46	99.29
Li	22	5
Rb	66	14
Be	3.0	3.2
Sr	132	312
Ba	636	207
V	151.0	80.2
Cr	42	44
Co	20	12
Ni	35	19
Cu	33.4	26.3
Zn	67.4	27.1
Sc	11.1	4.5
Y	13	36
Zr	224	217
Nb	33	25
As	14	6
Pb	<2	6
Au	15	6

Major elements given in weight percent (Fe_2O_3*, total Fe as Fe_2O_3); trace elements given in parts per million (gold in parts per billion).

TABLE 21: Major element oxides and trace element abundances, Jubilee shear zone.

	JS-90-1 P_0	JS-90-2 P_0	JS-90-3 P	JS-90-4 M
SiO_2	63.90	63.30	61.50	63.20
TiO_2	0.84	0.82	0.81	0.62
Al_2O_3	15.00	15.80	14.50	14.80
Fe_2O_3*	6.72	6.09	6.16	4.77
MnO	0.08	0.07	0.09	0.05
MgO	1.54	1.23	1.79	1.22
CaO	4.51	3.82	4.07	2.36
Na_2O	4.46	5.74	4.64	3.55
K_2O	1.48	1.15	1.91	4.46
P_2O_5	0.17	0.20	0.17	0.14
LOI	1.54	1.47	3.23	4.08
TOTAL	100.24	99.69	98.87	99.25
Li	26	14	22	11
Rb	53	36	64	95
Be	3.3	3.8	3.2	3.3
Sr	321	557	289	175
Ba	474	490	621	1460
V	52.1	40.3	58.0	20.8
Cr	40	51	46	43
Co	11	11	13	7
Ni	16	17	23	20
Cu	10.7	4.7	4.8	28.4
Zn	126.0	39.3	121.0	28.5
Sc	4.3	6.5	6.7	6.2
Y	27	20	26	19
Zr	257	287	174	278
Nb	24	29	10	51
As	<2	3	<2	<2
Pb	4	2	5	3
Au	9	<5	<5	5

Major elements given in weight percent (Fe_2O_3*, total Fe as Fe_2O_3); trace elements given in parts per million (gold in parts per billion).

TABLE 21: continued.

	JS-90-5 M	JS-90-6 M	JS-90-7 U	JS-90-8 M
SiO_2	61.80	56.50	63.30	62.90
TiO_2	0.70	0.67	0.55	0.57
Al_2O_3	13.60	12.30	16.00	15.80
Fe_2O_3*	5.71	4.75	5.42	6.07
MnO	0.10	0.12	0.07	0.60
MgO	2.54	3.00	2.25	2.18
CaO	2.85	6.07	1.79	2.65
Na_2O	0.91	0.92	4.01	4.77
K_2O	4.78	4.71	3.37	2.05
P_2O_5	0.15	0.09	0.10	0.10
LOI	4.93	9.23	2.62	2.16
TOTAL	98.07	98.36	99.48	99.85
Li	12	3	16	15
Rb	109	123	111	61
Be	4.6	4.2	1.7	1.0
Sr	85	173	237	242
Ba	754	835	790	697
V	22.3	4.5	41.0	57.5
Cr	35	219	70	59
Co	7	20	8	13
Ni	22	35	30	34
Cu	68.7	3.4	3.4	12.9
Zn	25.2	14.3	45.0	50.2
Sc	2.4	3.3	4.9	7.8
Y	14	14	19	21
Zr	186	150	162	159
Nb	<10	28	21	15
As	2	4	<2	2
Pb	2	<2	<2	<2
Au	26	<5	<5	8

Major elements given in weight percent (Fe_2O_3*, total Fe as Fe_2O_3); trace elements given in parts per million (gold in parts per billion).

TABLE 22: Major element oxides and trace element abundances, Minto A shear zone.

	MA-90-1 P_o	MA-90-2 P_o	MA-90-3 P	MA-90-4 U
SiO_2	63.20	61.40	62.20	60.20
TiO_2	0.60	0.89	0.92	0.62
Al_2O_3	15.80	16.20	16.40	16.90
Fe_2O_3*	5.84	7.28	7.30	5.38
MnO	0.06	0.11	0.08	0.07
MgO	2.47	1.45	1.36	2.25
CaO	2.87	2.34	2.30	2.57
Na_2O	4.90	5.82	5.07	3.35
K_2O	0.78	0.85	1.33	3.24
P_2O_5	0.11	0.22	0.23	0.10
LOI	2.47	2.93	2.16	4.62
TOTAL	99.10	99.49	99.35	99.30
Li	14	7	7	7
Rb	26	35	49	97
Be	1.1	1.2	1.5	0.7
Sr	333	234	343	175
Ba	413	401	660	1040
V	70.1	14.4	7.5	22.3
Cr	59	38	34	54
Co	15	6	10	10
Ni	31	7	7	23
Cu	2.9	3.7	4.3	5.4
Zn	62.8	66.1	60.7	52.4
Sc	5.4	6.3	3.3	2.2
Y	11	<10	29	<10
Zr	158	287	339	178
Nb	10	<10	14	<10
As	4	<2	2	2
Pb	<2	<2	<2	<2
Au	7	7	20	5

Major elements given in weight percent (Fe_2O_3*, total Fe as Fe_2O_3); trace elements given in parts per million (gold in parts per billion).

TABLE 23: Major element oxides and trace element abundances, Minto C shear zone.

	MC-90-1 P_0	MC-90-2 M	MC-90-3 U	MC-90-4 M	MC-90-7 P	MC-90-8 P_0
SiO_2	64.10	64.20	49.40	74.20	70.80	68.40
TiO_2	0.53	0.61	0.92	0.43	0.36	0.43
Al_2O_3	15.50	16.40	14.80	11.30	14.30	15.40
Fe_2O_3*	6.06	5.57	8.51	3.83	3.82	4.47
MnO	0.09	0.08	0.16	0.01	0.06	0.07
MgO	2.60	2.83	3.68	0.51	1.06	0.94
CaO	4.75	2.08	4.76	0.17	1.77	2.81
Na_2O	3.92	4.32	4.48	0.87	5.60	5.10
K_2O	1.22	1.12	2.77	3.37	0.92	1.22
P_2O_5	0.10	0.10	0.09	0.03	0.07	0.10
LOI	1.54	2.47	9.62	2.93	1.23	1.47
TOTAL	100.41	99.78	99.19	97.65	99.99	100.41
Li	14	10	8	3	7	7
Rb	63	52	69	61	42	46
Be	<0.5	1.0	3.9	1.2	1.3	2.6
Sr	343	256	91	41	297	415
Ba	437	407	562	782	450	607
V	39.0	48.8	75.3	1.4	19.3	9.9
Cr	96	104	149	63	62	47
Co	13	13	26	2	5	9
Ni	50	41	89	14	13	10
Cu	5.1	9.4	24.3	74.9	2.2	24.7
Zn	59.0	77.2	156.0	7.4	51.3	51.3
Sc	1.1	4.2	10.7	0.5	1.6	1.9
Y	25	28	<10	<10	<10	21
Zr	158	192	121	187	178	252
Nb	19	<10	13	18	14	<10
As	11	270	56	9400	14	11
Pb	<2	<2	<2	<2	<2	3
Au	5	20	270	5800	7	<5

Major elements given in weight percent (Fe_2O_3*, total Fe as Fe_2O_3); trace elements given in parts per million (gold in parts per billion).

TABLE 24: Major element oxides and trace element abundances, Minto E shear zone.

	ME-90-1 P	ME-90-2 P	ME-90-3 P	ME-90-4 M	ME-90-5 P
SiO_2	60.30	58.30	57.50	59.40	67.20
TiO_2	0.58	0.73	0.69	0.69	0.65
Al_2O_3	16.10	15.20	14.90	16.80	14.40
Fe_2O_3*	6.92	7.71	6.85	6.60	5.30
MnO	0.12	0.13	0.13	0.12	0.04
MgO	2.98	3.15	2.91	3.32	0.97
CaO	6.60	5.37	5.93	2.71	1.15
Na_2O	3.17	3.56	4.08	5.75	5.03
K_2O	0.72	1.33	1.53	0.93	2.20
P_2O_5	0.08	0.10	0.10	0.08	0.13
LOI	2.62	3.54	5.39	3.23	2.54
TOTAL	100.19	99.12	100.01	99.63	99.61
Li	18	21	14	15	5
Rb	31	54	53	36	48
Be	1.4	3	4.1	2.8	2.7
Sr	309	266	199	189	203
Ba	262	444	578	386	948
V	66.1	69.3	77.1	56.3	19.3
Cr	57	58	55	129	38
Co	20	21	19	11	12
Ni	44	37	34	47	12
Cu	9.6	23.6	27.7	1.1	32.4
Zn	81.4	77.5	71.8	64.7	28.1
Sc	2.2	4	6.7	5.5	2.5
Y	<10	14	18	<10	24
Zr	95	131	135	79	296
Nb	20	14	<10	<10	25
As	3	<2	<2	<2	30
Pb	2	<2	<2	<2	4
Au	6	16	8	5	630

Major elements given in weight percent (Fe_2O_3*, total Fe as Fe_2O_3); trace elements given in parts per million (gold in parts per billion).

TABLE 25: Major element oxides and trace element abundances, Parkhill East shear zone.

	PHE-90-1 P_0	PHE-90-2 P	PHE-90-3 P	PHE-90-4 M
SiO_2	63.20	65.50	55.50	68.20
TiO_2	0.44	0.37	0.77	0.45
Al_2O_3	16.40	16.40	16.40	11.60
Fe_2O_3*	5.16	3.93	7.42	5.48
MnO	0.08	0.06	0.13	0.09
MgO	2.22	1.75	4.78	2.87
CaO	4.87	5.00	5.96	4.50
Na_2O	3.92	4.35	3.04	2.22
K_2O	1.42	1.02	1.28	1.68
P_2O_5	0.09	0.09	0.13	0.08
LOI	1.23	0.85	3.31	2.23
TOTAL	99.03	99.32	98.72	99.40
Li	13	7	16	14
Rb	51	50	54	62
Be	<0.5	<0.5	1.2	<0.5
Sr	378	422	335	205
Ba	554	485	483	1280
V	42.3	31.5	90.4	60.1
Cr	48	37	173	93
Co	10	10	22	14
Ni	28	22	73	55
Cu	22.5	47.7	4.4	8.7
Zn	69.2	47.5	95.6	65.6
Sc	2.1	1.7	3.5	2.5
Y	<10	<10	<10	17
Zr	88	96	103	55
Nb	<10	<10	17	<10
As	2	4	15	16
Pb	<2	2	<2	<2
Au	8	8	<5	380

Major elements given in weight percent (Fe_2O_3*, total Fe as Fe_2O_3); trace elements given in parts per million (gold in parts per billion).

TABLE 25: continued.

	PHE-90-5 M	PHE-90-6 M	PHE-90-7 M	PHE-90-8 M
SiO_2	55.40	61.30	65.30	55.90
TiO_2	0.55	0.44	0.39	0.70
Al_2O_3	14.90	16.60	16.10	16.40
Fe_2O_3*	6.56	6.18	3.74	7.03
MnO	0.11	0.08	0.07	0.12
MgO	3.39	2.48	2.10	4.30
CaO	7.45	5.71	5.50	7.31
Na_2O	3.42	3.79	4.23	4.50
K_2O	1.98	1.35	0.72	1.19
P_2O_5	0.08	0.08	0.08	0.12
LOI	6.00	2.47	2.00	1.47
TOTAL	99.84	100.48	100.23	99.04
Li	21	13	8	10
Rb	73	46	30	35
Be	1.8	<0.5	<0.5	1.4
Sr	277	429	428	328
Ba	738	608	510	558
V	68.7	34.5	31.5	48.2
Cr	93	47	41	130
Co	19	10	10	19
Ni	57	24	24	53
Cu	18.9	45.3	91.4	11.3
Zn	85.7	72.6	45.9	54.7
Sc	5.1	2	2.5	2
Y	<10	13	<10	17
Zr	109	98	88	109
Nb	33	<10	<10	<10
As	15	<2	5	16
Pb	<2	<2	<2	<2
Au	370	8	15	<5

Major elements given in weight percent (Fe_2O_3*, total Fe as Fe_2O_3); trace elements given in parts per million (gold in parts per billion).

TABLE 26: Major element oxides and trace element abundances, Parkhill West shear zone.

	PHW-90-1 P_o	PHW-90-2 M	PHW-90-3 M	PHW-90-4 M	PHW-90-5 M
SiO_2	72.80	70.10	63.80	60.00	61.50
TiO_2	0.26	0.31	0.51	0.39	0.30
Al_2O_3	13.60	14.20	15.40	13.50	12.70
Fe_2O_3*	2.27	2.64	4.90	5.00	4.04
MnO	0.05	0.06	0.08	0.11	0.13
MgO	0.85	1.05	2.11	1.78	1.58
CaO	1.70	1.96	3.57	6.72	6.55
Na_2O	5.12	2.72	2.63	4.14	2.35
K_2O	1.92	3.18	2.62	2.42	3.07
P_2O_5	0.06	0.05	0.12	0.06	0.07
LOI	1.39	1.85	3.39	6.00	6.85
TOTAL	100.02	98.12	99.13	100.12	99.14
Li	6	9	9	6	4
Rb	82	115	90	60	83
Be	2.4	2.2	3.2	4.5	4.7
Sr	190	155	208	238	118
Ba	642	704	1010	674	667
V	15.6	12.4	27.6	16	6.3
Cr	54	37	55	49	42
Co	10	6	17	16	11
Ni	13	11	28	26	19
Cu	16.3	2.2	107	61.3	31.7
Zn	30.3	30.0	49.8	40.7	35.8
Sc	2.8	2.1	3.2	1.5	2.3
Y	15	23	12	18	22
Zr	218	190	137	124	211
Nb	14	11	17	12	17
As	3	<2	<2	<2	2
Pb	<2	2	5	3	5
Au	15	7	17	14	35

Major elements given in weight percent (Fe_2O_3*, total Fe as Fe_2O_3); trace elements given in parts per million (gold in parts per billion).

BIBLIOGRAPHY

Bancroft, G.M. and Jean, G., 1982. Gold deposition at low temperatures on sulphide minerals. Nature, 298; 730-731.

Bas, B., 1992. Hydrothermal alteration and fluid inclusion geochemistry of auriferous deformation zones and vein systems, S.W. Michipicoten Greenstone Belt, Ontario. University of Windsor. Unpublished MSc. Thesis.

Beane, R.E., 1981. Porphyry copper deposits: Part II: Hydrothermal alteration and mineralization. *In* Economic Geology 75thAnniversary Volume; 214-269.

Bell, T.H., 1981. Foliation development - the contribution, geometry and significance of progressive, bulk, inhomogeneous shortening. Tectonophysics, 75; 273-296.

Bell, T.H. and Etheridge, M.A., 1973. Microstructures of mylonites and their descriptive terminology. Lithos, 6; 337-348.

Bell, T.H. and Hammond, R.L., 1984. On the internal geometry of mylonite zones. Journal of Geology, 92; 667-686.

Berthé, D., Choukroune, P. and Jegouzo, P., 1979. Orthogneiss, mylonite and non-coaxial deformation of granites: the example of the South Armorican Shear Zone. Journal of Structural Geology, 1; 31-42.

Bryant, B., 1966. Formation of phyllonites in the Grandfather mountain area, northwestern North Carolina. United States Geological Survey Professional Paper, 550-D; 144-150.

Cann, J.R., 1970. Rb, Sr, Y, Zr, and Nb in some ocean floor basaltic rocks. Earth and Planetary Science Letters, 10; 7-11.

Card, K.D. and Ciesielski, A., 1986. Subdivisions of the Superior Province of the Canadian Shield (DNAG v.1). Geoscience Canada, 13; p.5-13.

Choukroune, P. and Gapais, D., 1983. Strain pattern in the Aar Granite (Central Alps): orthogneiss developed by bulk inhomogeneous flattening. Journal of Structural Geology, 5; 411-418.

Cobbold, P.R., 1977. Description and origin of banded deformation structures. I. Regional strain, local perturbations, and deformation bands. Canadian Journal of Earth Sciences, 14; 1721-1731.

Correns, C.W., 1978. Titanium: behavior in metamorphic reactions. *In* Handbook of Geochemistry, 2 (II). K.H. Wedepohl (ed.). 67 p.

Colvine, A.C., 1989. An empirical model for the formation of Archean gold deposits: Products of final cratonization of the Superior Province, Canada. *In* The Geology of gold deposits: The perspective in 1988. R.R. Keays, W.R.H. Ramsay and D.I. Groves (eds.), Economic Geology, monograph 6; 37-53.

Colvine, A.C., Fyon, J.A., Heather, K.B., Marmont, S., Smith, P.M. and Troop, D.G., 1988. Archean lode gold deposits in Ontario: Part I. A depositional model; Part II. A genetic model. Ontario Geological Survey Miscellaneous Paper 139, 136 p.

Coward, M.P., 1976. Strain within ductile shear zones. Tectonophysics, 34; 181-197.

Dicken, A.P., 1988. Evidence for limited REE leaching from the Roffna Gneiss, Switzerland - a dicussion of the paper by Vocke et al. (1987) (CMP95:145-154). Contributions to Mineralogy and Petrology, 99; 273-275.

Dixon, J. and Williams, G., 1983. Reaction softening in mylonites from the Arnaboll thrust, Sutherland. Scottish Journal of Geology, 19; 157-168.

Feather, C.E. and Willis, J.P., 1976. A simple method for background and matrix correction of spectral peaks in trace element determination by X-ray fluorescence spectrometry. X-ray Spectrometry, 5; 41-48.

Glasner, A.F. and Bartley, J.M., 1991. Volume loss, fluid flow and state of strain in extensional mylonites from the cental Mojave Desert, California. Journal of Structural Geology, 13; 587-594.

Goodwin, A.M., 1972. The Superior Province. *In* Variations in Tectonic Style in Canada. R.A. Price and R.J.W. Douglas, (eds.) Geological Association of Canada Special Paper 11, 528-623.

Grant, J.A., 1986. The isocon diagram - a simple solution to Gresens' equation for metasomatic alteration. Economic Geology, 81; 1976-1982.

Gresens, R.L., 1967. Composition-volume relationships of metasomatism. Chemical Geology, 2; 47-65.

Griggs, D.T. and Blacic, J.D., 1965. Anomalous weakness of synthetic crystals. Science, 147; 292-295.

Guibert, J.M. and Park, C.F., 1986. The Geology of Ore Deposits. W.H. Freeman and Company, New York, 985 p.

Hanmer, S., 1986. Asymmetrical pull-aparts and foliation fish as kinematic indicators. Journal of Structural Geology, 8; 111-122.

Hanmer, S., 1987. Textural map units in quartzo-feldspathic mylonitic rocks. Canadian Journal of Earth Sciences, 24: 2065-2073.

Helmstaedt, H., 1988. Structural observations in the Surluga and Jubilee Mines, Wawa.

Herrmann, A.G., 1978. Yttrium: abundance in natural waters. *In* Handbook of Geochemistry 2(IV), H.K. Wedepohl (ed.). Springer, Berlin, p.57.

Holland, H.D. and Malinin, S.D., 1979. The solubility of non-ore minerals. *In* Handbook of Geochemistry of Hydrothermal Ore Deposits, H.L.Barnes (ed.), 2nd Edition. Wiley, New York, N.Y., 798 pp.

Hortenbach, R., 1977. Pressure solution processes in carbonates and their importance. Zeitschrift fur Geologie Wissenschaften, 5; 617-621.

Hutchinson, C.S., 1974. Laboratory Hanbook of Petrographic Techniques. John Wiley and Sons, Inc., New York.

Kerrich, R., Fyfe, W.S., Gorman, B.E. and Allison, I., 1977. Local modification of rock chemistry by deformation. Contributions to Mineralogy and Petrology, 65; 183-190.

Landergren, S., 1978. Vanadium: Solubilities of compounds which control concentrations of Vanadium in natural waters; adsorption processes, valence states in natural environments. *In* Handbook of Geochemistry, 2 (II), K.H. Wedepohl (ed.). Springer, Berlin, p.23.

Lapworth, C., 1885. The Highland contoversy in British history: its causes, course and consequences. Nature, 32; 558-559.

Lister, G.S. and Snoke, A.W., 1984. S-C Mylonites. Journal of Structural Geology, 6; 617-638.

Lumbers, S.B., 1978. Geology of the Grenville Front Tectonic Zone in Ontario. GAC/MAC 1978 Toronto, Field Trip Guidebook, pp. 347-361. A.L. Currie and W.O. Mackasey, eds.

Norrish, K. and Hutton, J.T., 1969. An accurate X-ray spectrographic method for the analysis od a wide range of geological samples. Geochemica et Cosmochemica Acta, 33; 431.

O'Hara, K., 1988. Fluid flow and volume loss during mylonitization: an origin for phyllonite in an overthrust setting, North Carolina, U.S.A. Tectonophysics, 156; 21-36.

O'Hara, K., 1990. State of strain in mylonites from the Western Blue Ridge Province, Southern Appalachians: The role of volume loss. Journal of Structural Geology, 12; 419-430.

O'Hara, K. and Blackburn, W.H., 1987. Fluid flow and volume loss during mylonitization: evidence from the western Blue Ridge, North Carolina. Geological Society of America Abstracts with Programs, 156; 792.

O'Hara, K. and Blackburn, W.H., 1989. Volume-loss model for trace-element enrichments in mylonites. Geology, 17; 524-527.

Ojakangas, R.W., 1983. Clastic sedimentary rocks of the Michipicoten volcanic-sedimentary belt, Wawa, Ontario. *In* Workshop on a cross section of Archean crust, L.D. Ashwal and K.D. Card (eds.). Lunar and Planetary Institute Technical Report 83-03; 66-70.

Olsen, S.N. and Grant, J.A., 1991. Isocon analysis of migmatization in the Front Range, Colorado, USA. Journal of Metamorphic Geology, 9; 151-164.

Passchier, C.W. and Simpson, C., 1983. Porphyroclast systems as kinematic indicators. Journal of Structural Geology, 8; 831-844.

Perring, C.S., Groves, D.I. and Ho, S.E., 1987. Constraints on the source of auriferous fluids for Archean gold deposits. *In* Recent advances in understanding Precambrian gold deposits, Ho, S.E. and Groves, D.I.(eds.). Nedlands, University of Western Australia Geology Department University Ext. Pub. 11; 287-306.

Ralser, S., Hobbs, B.E. and Ord, A, 1991. Experimental deformation of a quartz mylonite. Journal of Structural Geology, 13; 837-850.

Ramsay, J.G., 1980. Shear zone geometry: a review. Journal of Structural Geology, 2; 83-99.

Ramsay, J.G. and Huber, M.I., 1987. The Techniques of Modern Structural Geology, Volume 2: Folds and Fractures. Acedemic Press, London. pp. 309-700.

Ramsay, J.G. and Wood, D.S., 1973. The geometric effects of volume change during deformation processes. Tectonophysics, 16; 263-277.

Robert, F. and Brown, A.C., 1986. Archean gold-bearing quartz veins at the Sigma mine, Abitibi greenstone belt, Quebec. Economic Geology, 79; 393-399.

Rohlf, F.J. and Sokal, R.R., 1969. Statistical Tables. W.H. Freeman and Company, San Francisco, 253 p.

Rupert, R.J., 1975. Ontario Division of Mines, Open File Report and Map P. 828.

Rupert, R.J., 1979. Geology of McMurray Township and parts of surrounding townships, District of Algoma; Ontario Geological Survey. OFR 5283; 170 p.

Sage, R.P., 1979. Wawa area, District of Algoma, pp. 48-53. *In* Summary of Field Work, 1979 by the Ontario Geological Survey. V.G. Milne, O.L. White, R.B. Barlow and C.R. Kustria (eds.), Ontario Geological Survey Miscellaneous Paper 90; 245 p.

Sage, R.P., 1980. Stratigraphic correlation in the Wawa area. *In* Volcanology and Mineral Deposits, Ontario Ministry of Resources, p.62-68.

Sage, R.P., 1981. Preliminary interpretation of the relationship between economic mineralization and volcanic stratigraphy in the Wawa area, p.41-44. *In* Summary of Field Work, 1981 by the Ontario Geological Survey. J. Wood, O.L. White, R.B. Barlow, and A.C. Colvine (eds.), Ontario Geological Survey, Miscellaneous Paper 100; 255p.

Sage, R.P., 1991. Synoptic studies in the Michipicoten greenstone belt. *In* Summary of Field Work and Other Activities 1990, Ontario Geological Survey, Miscellaneous Paper 151; p. 48-52.

Samson, I.M. and Holm, P.E., 1990. Geological relationships in mineralized deformation zones, McMurray Township, Wawa, Ontario. Unpublished Report, Department of Geology, University of Windsor.

Sibson, R.H., 1977. Fault rocks and fault mechanisms. Geological Society of London, 133; 191-213.

Sibson, R.H., Robert, F. and Poulsen, K.H., 1988. High-angle reverse faults, fluid pressure cycling and mesothermal gold-quartz deposits. Geology, 16; 551-555.

Simpson, C., 1986. Fabric development in brittle-to-ductile shear zones. Pure and Applied Geophysics, 124; 269-288.

Simpson, C. and Schmid, S. M., 1983. An evaluation of criteria to deduce the sense of movement in sheared rocks. Geological Society of America Bulletin, 94; 1281-1288.

Sinha, A.K., Hewitt, D.A., and Rimstidt, J.D., 1986. Fluid interaction and element mobility in the development of ultramylonites. Geology, 14; 883-886.

Sokal, R.R.and Rohlf, F.J., 1969. Biometry. The principles and practice of statistics in biological research. W.H. Freeman and Company, San Francisco, 776 p.

Spooner, E.T.C., Burrows, D.R., Callan, N.J., De Ronde. C.E.J. and Wood, P.C., 1987. High hydrothermal fluid pressures, hydraulic fracturing, and fluid pressure dilation of shear zones in Archean Au-quartz vein systems [abs.]. Geological Association of Canada, Summer Field Meeting, Yellowknife, Program with Abstracts.

Sylvester, P.J., Attoh, K. and Schluz, K.J., 1989. Tectonic setting of the late Archean bimodal volcanism in the Michipicoten (Wawa) greenstone belt, Ontario. Canadian Journal of Earth Sciences, 24, 1120-1134.

Thurston, P.C., 1986. Volcanic cyclicity in mineral exploration: The caldera cycle and zoned magma chambers. *In* Volcanology and Mineral Deposits, Ontario Geological Survey Miscellaneous Paper 129; 104-123.

Tortosa, D.J.J., Frey, E.D., Stewart, R.C., Wilson, A.C., Wing, W., Ashick, L., Melisek, J.D., 1988. Wawa resident geologist's district - 1988. OGS Report

Tortosa, D.J.J., Frey, E.D., Delisle, P.C., Lowe, C., Wilson, A.C., Beach, P. and Walmsley, J.R., 1989. Wawa resident geologist's district -1989; Report on Activities 1989, Resident Geologists, Ontario Geological Survey. Miscellaneous Paper 147; 183-204.

Tullis, J., Snoke, A. and Todd, V., 1982. Significance and petrogenesis of mylonitic rocks. Geology, 2; 175-188.

Turek, A., Sage, R.P., and Van Schmus, W.R., 1990. Advances in geochronology of the Michipicoten greenstone belt. *In* Proceedings, 36th Annual Meeting, Institute on Lake Superior Geology, p. 110-111.

Vocke, R.D., Hanson, G.N., and Grunenfelder, M., 1987. Rare earth element mobility in the Roffna Gneiss, Switzerland. Contributions to Mineralogy and Petrology, 95; 145-154.

Wayne, D.M., and Sinha, A.K., 1988. Physical and chemical response of zircons to deformation. Contributions to Mineralogy and Petrology, 98; 109-121.

White, S.H., Barrows, S.E., Carreras, J., Shaw, N.D., and Humphreys, F.J., 1980. On mylonites in ductile shear zones. Journal of Structural Geology, 2; 175-188.

White, S.H. and White, S.E., 1983. Semi-brittle deformation within the Alpine fault zone, New Zealand. Journal of Structural Geology, 5; 579-589.

Winchester, J.A., and Max, M.D., 1984. Element mobility associated with syn-metamorphic shear zones near Scatchport, NW Mayo, Ireland. Journal of Metamorphic Geology, 2; 1-11.

Wise, D.U., Dunn, D. E., Engelder, J.T., Geiser, P.A., Hatsher, R.D., Kish, S.A., Odom, A.L., and Schamel, S., 1984. Fault-related rocks: Suggestions for terminology. Geology, 12; 391-394.

Zeck, H.P., 1974. Cataclastites, hemiclastites, holoclastites, blasto-ditto, and myloclastites - cataclastic rocks. American Journal of Science, 274; 1064-1073.

VITA AUCTORIS

NAME: Deborah Lynn MacDonald

PLACE OF BIRTH: Antigonish, Nova Scotia

DATE OF BIRTH: May 31, 1967.

EDUCATION: Whycocomagh Consolidated School,
Whycocomagh, Nova Scotia.
1979-1985

Saint Francis Xavier University,
Antigonish, Nova Scotia.
1985-1989 B.Sc.

University of Windsor,
Windsor, Ontario.
1990-1991 M.Sc.